NOVEL OPTICAL WAVEGUIDES: FROM DIELECTRIC TO PLASMONIC

SI GUANGYUAN

A THESIS SUBMITTED FOR THE DEGREE OF DOCTOR OF PHILOSOPHY

DEPARTMENT OF ELECTRICAL AND COMPUTER ENGINEERING

NATIONAL UNIVERSITY OF SINGAPORE

2011

Acknowledgements

I would like to thank my advisors, Dr. Aaron Danner and Dr. Teng Jinghua, for offering me the opportunity to work on exciting and interdisciplinary projects and providing me the wonderful chance to finish my PhD degree. Their unwavering support, invaluable guidance and suggestions are greatly appreciated.

I gratefully acknowledge my friends in Institute of Materials Research and Engineering (IMRE): Chew Ah Bian, Norman Ang, Teo Siew Lang, Hui Hui Kim, Liu Hong, Eunice Leong, Liu Yanjun, and Steve Wu.

I especially thank Dr. Zhang Mingsheng from Data Storage Institute (DSI), for helping me with the ion milling process which was critical to my work and Zhao Yanhui from Pennsylvania State University (PSU) for simulations and fruitful discussions.

Finally, I would like to thank my wife and my parents for their constant encouragement and support during this course.

Table of Contents

Acknowledgements....I

Table of Contents....II

Abstract....V

List of Acronyms....VI

List of Figures....VII

List of Tables....XI

List of Publications....XII

Chapter-1: Introduction

1.1 Background and literature reviews....1

1.2 Research motivation....4

1.3 Thesis outline....5

Chapter-2: Suspended Slab and Photonic Crystal Waveguides in LN

2.1 Waveguides in LN and traditional etching methods....8

2.2 How to fabricate suspended waveguides in LN....10

2.3 Results and discussion....13

2.4 Chapter summary....19

Chapter-3: Ultrahigh Aspect Ratio Waveguides in LN

3.1 PCs in LN and FIB technique....20

3.2 Nanoholes with standard profiles....21

3.3 Nanorings with ultrahigh aspect ratio....23

3.4 Nanorod arrays by FIB milling..27

3.5 Chapter summary..30

Chapter-4: Fabrication of Coaxial Metamaterials and Nanorod Arrays

4.1 Fabrication tools for plasmonic structures.........................31

4.2 Plasmonic coaxial waveguides...33

4.3 Plasmonic nanorod arrays..35

4.4 Chapter summary..39

Chapter-5: Annular Aperture Array Based Color Filter

5.1 EOT through AAA…..41

5.2 Tunable resonance via geometric control..........................44

5.3 Fabrication and characterization of AAA color filter........48

5.4 Chapter summary..51

Chapter-6: Plasmonic Crystal Color Filter Based on Silver Nanorods with Ultrasmall Spacings

6.1 Coupling regimes in plasmonic nanorods.........................52

6.2 Nanorod color filter based on strong coupling effect.........54

6.3 Chapter summary..65

Chapter-7: Plasmon-Induced Transparency in Plasmonic Crystals with Ultrasmall Gaps

7.1 EIT in classic optics...66

7.2 Plasmon-induced transparency in ultrasmall gaps.............67

7.3 Chapter summary..71

Chapter-8: Summary and Future Work

8.1 Summary of this thesis..72

8.2 Improving device performance…….....................................73

8.3 Tunable plasmonic devices using LCs...............................77

8.4 3-D metamaterials and novel plasmonic clusters..............79

References...80

Abstract

Lithium niobate is an important material for fabricating optoelectronic devices due to its novel optical properties especially the high electro-optical coefficient. However, it is quite difficult to etch this material due to its poor reactivity with common etchants and selectivity issues. In this work, an elegant way of fabricating suspended waveguides in lithium niobate is developed. Using combined techniques, monolithic fabrication of strip waveguides and photonic crystals is available in bulk lithium niobate now. A symmetric cladding structure (air-lithium niobate-air) can be formed once the buried sacrificial layer introduced by ion implantation is removed by chemicals, resulting in significantly enhanced light confinement in the waveguide as well as dramatically reduced propagation losses. The influence of waveguide sidewall on device performance is also investigated in detail. Ultra-high aspect ratio (50:1) photonic crystals are fabricated. Subsequently, all the novel structures realized in lithium niobate are introduced to noble metals, leading to fascinating plasmonic waveguides. Such devices have found important applications in developing nanophotonics and integrated optics. As typical examples, color filters under transmission and reflection testing modes are demonstrated using nanorings and rods, respectively. In particular, the nanorod color filter could be applied in digital light processing techniques since each mirror or pixel can be made very small to achieve a high resolution. More interestingly, a pronounced plasmon induced resonance peak is observed in symmetric plasmonic patterns with ultra-small gaps which can find important applications in plasmon-assisted sensing and imaging.

List of Acronyms (In Alphabetical Order)

1. AAA, annular aperture array.
2. CSP, cylindrical surface plasmon.
3. EBL, electron beam lithography.
4. EIR, electromagnetically induced reflectance.
5. EIT, electromagnetically induced transparency.
6. EOT, extraordinary optical transmission.
7. ETES, edge-to-edge separation.
8. FBMS, fixed beam moving stage.
9. FDTD, finite-difference time-domain.
10. FIB, focused ion beam.
11. FWHM, full width at half maximum.
12. ICP, inductively coupled plasma.
13. LCs, liquid crystals.
14. LN, lithium niobate, $LiNbO_3$.
15. LSPR, localized surface plasmon resonance.
16. PCs, photonic crystals.
17. PE, proton exchange.
18. PSP, planar surface plasmon.
19. RIE, reactive ion etching.
20. SEM, scanning electron microscope.
21. SOI, silicon on insulator.
22. SP, surface plasmon.
23. SRIM, stopping and range of ions in matter.
24. 3-D, three dimensional.
25. 2-D, two dimensional.

List of Figures

Fig. 1-1. SEM images showing lifted-off pieces of pillar tops in an x-cut LN..............3

Fig. 1-2. Pictorial overview of this thesis..6

Fig. 2-1. Illustration of the process steps to create suspended structures in LN using ion implantation, FIB milling and selective wet etching...11

Fig. 2-2. (a) SRIM simulation of 1 MeV He^+ in LN. (b) SRIM simulations of 0.8, 1, and 1.15 MeV He^+ in LN...12

Fig. 2-3. SEM image of a rectangular hole patterned on the edge of implanted area...14

Fig. 2-4. (a) FIB image of a post after milling and before wet etching. (b) SEM image of a post after wet etching. (c) SEM image showing the cross-sectional view...........15

Fig. 2-5. Cross-sectional images showing the undercut after 10 min (a) and 20 min (b) of wet etching. The inset of (a) shows a further magnified view of the right part of the undercut structure...17

Fig. 2-6. Fabricated PCs in a suspended LN slab. All the holes have been milled through the slab...18

Fig. 3-1. (a) SEM image showing the tapered cross-sections of nanoholes. (b) Cross section of PCs in a suspended LN film fabricated by implantation, FIB milling and wet etching. Note that these two hole arrays have different periodicities...................22

Fig. 3-2. SEM image showing nearly vertical sidewalls of holes with labeled angles in comparison with seriously tapered bottoms...24

Fig. 3-3. Top view SEM images of ring structures with fixed inner radius (80 nm) and varying outer radii (a) 140 nm, (b) 180 nm, (c) 220 nm, and (d) 260 nm...................25

Fig. 3-4. (a) Top view of the nanoring arrays with 200 nm inner radius and 240 nm outer radius. (b) Cross sectional view showing the straightly etched ring apertures...26

Fig. 3-5. (a) Glancing view of nanorod arrays with hexagon-shaped lattices. (b) Cross sectional view showing the bottoms of nanorods by a gradient milling at 15-degree...28

Fig. 3-6. (a) Low and (b) high magnification cross-sectional images showing

vertically etched dense nanorods with less than 30 nm gaps and more than 2.5 μm etching depth....29

Fig. 4-1. SEM images of coaxial waveguides with different gap aperture widths in a 450-nm-thick gold film on a quartz substrate. (a) - (d), outer radii R_o equal to 220 nm, 260 nm, 300 nm and 340 nm with fixed inner radius R_i at 200 nm and pitch Λ= 1200 nm. (e) Similar nanoring structures fabricated in a 450-nm-thick silver film for comparison. (f) Cross sectional view of 15-nm gap width coaxial apertures. Note the difference of periodicity between (e) and (a)-(d)....34

Fig. 4-2. Top view SEM images of metallic (110 nm thick gold) annular structures fabricated by EBL and ion milling with (a) 100 nm inner radius and 200 nm outer radius and (b) 60 nm inner radius and 280 nm outer radius....35

Fig. 4-3. Schematic diagram of the FIB lithography method for nanorod fabrication based on nanoring patterning....36

Fig. 4-4. SEM images showing dense nanorod arrays with varying lattice shapes fabricated in a 450-nm-thick gold film on a quartz substrate by FIB milling. Nanorods formed with (a) large difference in size, (b) moderate difference in size, and (c) equally-sized lattices. (d) shows the bottoms of the fabricated nanorods and one can clearly observe the angle of slightly tapered profiles of the fabricated rods. Top views of plasmonic crystals with (e) square lattices and (f) square-circle lattices....36

Fig. 4-5. SEM top views of plasmonic crystals fabricated using EBL and ion milling methods in a 110-nm-thick gold film with different periodicities of (a) 900 nm, (b) 700 nm, (c) 500 nm, and (d) 300 nm....38

Fig. 4-6. (a) Transmittance and (b) reflectance spectra of the plasmonic crystals shown in Fig. 4-5....39

Fig. 5-1. Schematic drawing of the proposed color filter working under transmission measurement....45

Fig. 5-2. SEM images showing (a) overview of a fabricated 9 × 9 AAA and (b) magnified view of a single ring with 25 nm gap width. (c) Measured and (d) simulated transmission spectra of AAAs as a function of gap width. Simulated spectra are

normalized for clarity. The apertures have fixed inner radius at 200 nm and varying outer radii from 225 nm to 270 nm in steps of 15 nm. The arrow in (c) indicates decreasing gap width. Inset of (d), magnified peak tops with 700-800 nm wavelength range to show the shift more clearly..45

Fig. 5-3. Top panel: top view; and bottom panel: cross sectional view showing the electric intensity distribution of a single ring with 55 nm gap width illuminated at 740 nm (λ_{max}) and 600 nm (λ_{min}). 48

Fig. 5-4. SEM images of the fabricated AAAs with (a) 40 nm, (b) 80 nm, (c) 120 nm, and (d) 160 nm gap width (outer radii equal to 240 nm, 280 nm, 320 nm, and 360 nm with 200 nm fixed inner radius). Scale bars are 200 nm. (e) Corresponding optical image presenting different colors. (f) Measured transmission spectra of the AAAs with different color outputs shown in (e)..49

Fig. 5-5. Optical images showing the words of (a) "NUS" and (b) "IMRE" with different colors..50

Fig. 6-1. Schematic of the proposed color filter working under reflection mode........55

Fig. 6-2. (a) SEM image showing the top view of the nanorod array with period p =550 nm. Scale bar, 200 nm. (b) Measured and (c) calculated reflection spectra of nanorod arrays with periodicities from 400 nm to 700 nm. The arrow indicates increasing periodicities. The height of the nanorods is 240 nm..................................57

Fig. 6-3. Dependence of the reflection resonant wavelength on the periodicity. As the periodicity is varied, the resonance (λ_{max}) sweeps with a typical constant increment (about 90 nm)..58

Fig. 6-4. Simulated reflection of nanorod arrays with constant periodicity p = 400 nm and varying d/p ratios..59

Fig. 6-5. SEM images of nanorods with ultrasmall gaps. (a) - (e) Oblique views of nanorod arrays with varying periodicities from 540 nm (a) to 320 nm (e) in steps of 55 nm. (f) Magnified top view of the p = 375 nm rod array (blue color). It is obvious that the rods have been milled through. The height of the nanorods is 240 nm..................60

Fig. 6-6. (a) Optical image showing different color outputs under reflection mode using plasmonic nanorod crystals. Measured corresponding reflection (b) and transmission (c) spectra of the arrays as a function of wavelength............................62
Fig. 6-7. Electric intensity distribution of nanorods with 50 nm (top panel) and 20 nm (bottom panel) spacings illuminated at 670 nm (λ_{max}) / 720 nm (λ_{min}) and 670 nm (λ_{max}) /740 nm (λ_{min}), respectively...63
Fig. 7-1. (a) Schematic diagram of the FIB lithography method for nanorod fabrication based on nanoring patterning. (b) and (c), two typical designs proposed in this study. SEM images of (b) diamond-circle and (c) square-circle lattices.............67
Fig. 7-2. SEM images showing decreasing ETES of diamond-circle (left column) and square-circle (right column) shaped lattices. All scale bars are 200 nm.....................68
Fig. 7-3. Measured reflectance and transmittance spectra of plasmonic nanoantenna systems consisting of diamond-circle ((a) and (b)) and square-circle ((c) and (d)) shaped lattices with different ETES..70
Fig. 8-1. SEM image showing the stitching error in a standard EBL process............74
Fig. 8-2. Microscope image of a strip waveguide with rough sidewalls and PCs.......74
Fig. 8-3. (a) Intensity distribution of a channel waveguide fabricated in an x-cut LN substrate using proton exchange technique. (b) Cross section of a trench after ICP etching a channel waveguide...75
Fig. 8-4. (a) Schematic diagram of fabricating channel waveguides in LN using He implantation. (b) Microscope image of a strip waveguide on LN with a thick metal film as implantation mask. (c) Top view SEM showing PCs in the waveguide..........76
Fig. 8-5. Schematic of the experimental setup for characterization of the hybrid system. The enlarged part shows the reversible N–I phase transition induced by the *trans-cis* photoisomerization of the photochromic LCs..78
Fig. 8-6. The trans-cis isomerization of BMAB under UV flood exposure. Inset, the structure of a BMAB molecule and its reversible trans-cis isomerization.................78
Fig. 8-7. (a) - (h) Examples of 3-D metamaterials and novel plasmonic clusters.......79

List of Tables

Table 6-1. Parameters of the arrays presenting different colors................................61

List of Publications (Resulting From Work in This Thesis)

Journal Papers

1. G. Y. Si, Y. H. Zhao, Y. J. Liu, N. Xiang, A. J. Danner, T. J. Huang, and J. H. Teng, "Plasmon-induced transparency in plasmonic crystals with ultrasmall gaps", to be submitted.
2. G. Y. Si, Y. H. Zhao, M. Q. Lu, Y. J. Liu, H. Liu, N. Xiang, A. J. Danner, T. J. Huang, and J. H. Teng, "Plasmonic crystal color filter with ultrasmall spacings", to be submitted.
3. Y. J. Liu, G. Y. Si, E. S. P. Leong, N. Xiang, A. J. Danner, and J. H. Teng, "Light-driven plasmonic color filters by overlaying photoresponsive liquid crystals on gold annular aperture arrays", accepted by *Adv. Mater.* (2012).
4. Y. J. Liu, G. Y. Si, E. S. P. Leong, B. Wang, A. J. Danner, X. C. Yuan and J. H. Teng, "Optically tunable plasmonic color filters," *Appl. Phys. A* **107**, 49 (2012).
5. B. Wang, A. B. Chew, J. H. Teng, G. Y. Si, and A. J. Danner, "Sub-wavelength lithography by waveguide mode interference", *Appl. Phys. Lett.* **99**, 151106 (2011).
6. H. Tanoto, J. H. Teng, Q. Y. Wu, M. Sun, Z. N. Chen, S. A. Maier, B. Wang, C. C. Chum, G. Y. Si, A. J. Danner, S. J. Chua, "Greatly enhanced continuous-wave terahertz emission by nano-electrodes in a photoconductive photomixer", *Nat. Photon.* **6**, 121 (2012).
7. J. Deng, W. Jia, G. Y. Si, S. Jaesung, Y. Hyunsoo, A. J. Danner, "Deep anisotropic $LiNbO_3$ etching with SF_6/Ar inductively coupled plasmas", *J. Vac. Sci. Techno. B* **30**, 011208 (2012).
8. G. Y. Si, Y. H. Zhao, H. Liu, S. Teo, M. S. Zhang, T. J. Huang, A. J. Danner, and J. H. Teng, "Annular aperture array based color filter", *Appl. Phys. Lett.* **99**, 033105 (2011).
9. G. Y. Si, A. J. Danner, S. L. Teo, E. J. Teo, J. H. Teng, and A. A. Bettiol, "Photonic crystal structures with ultrahigh aspect ratio in lithium niobate

fabricated by focused ion beam milling," *J. Vac. Sci. Techno. B* **29**, 021205 (2011).

10. G. Y. Si, A. J. Danner, J. H. Teng, S. S. Ang, A. B. Chew, E. Dogheche, "Nanoscale arrays in lithium niobate fabricated by interference lithography and dry etching," *International J. of Nanoscience* **9**, 311 (2010).
11. H. Liu, B. Wang, E. S. P. Leong, P. Yang, Y. Zong, G. Y. Si, J. H. Teng, and S. A. Maier, "Enhanced surface plasmon resonance on a smooth silver film with a seed growth layer," *ACS Nano* **4**, 3139 (2010).
12. G. Y. Si, E. J. Teo, A. A. Bettiol, J. Teng, and A. J. Danner, "Suspended slab and photonic crystal waveguides in lithium niobate," *J. Vac. Sci. Techno. B* **28**, 316 (2010).

Conference Presentations

13. H. Tanoto, Q. Y. Wu, M. Sun, Z. N. Chen, B. Wang, S. L. Teo, C. C. Chum, S. A. Maier, G. Y. Si, L. Y. Deng, A. J. Danner, S. J. Chua, and J. H. Teng, "Nano-antenna for greatly enhanced THz emission in a photomixer," *SPIE Photonics Europe*, 2012.
14. Y. J. Liu, G. Y. Si, E. S. P. Leong, N. Xiang, A. J. Danner, and J. H. Teng, "Optically tunable plasmonic color filters based on photoresponsive liquied crystals and gold annular aperture arrays," *ICNP*, Beijing, China, 2012.
15. B. Wang, Y. J. Liu, G. Y. Si, E. S. P. Leong, N. Xiang, A. J. Danner, and J. H. Teng, "Plasmonic Brillouin Scattering and Filtering," *IPS12*, Institute of Physics Singapore, Faculty of Science, National University of Singapore, Singapore, 2012.
16. H. Liu, B. Wang, E. S. P. Leong, L. Ke, J. Deng, C. C. Chum, M. Zhang, L. Shen, G. Y. Si, Y. Liu, A. J. Danner, S. A. Maier, J. Teng, "Surface roughness of Ag film on the optical properties of metal-dielectric-metal film and super-resolution imaging," *ICMAT 2011* (invited oral presentation) *and A-Star metamaterial workshop*, Suntec Convention Centre, Singapore, June 26 - July 1, 2011.

17. H. Liu, L. Ke, J. Deng, C. C. Chum, M. Zhang, L. Shen, G. Y. Si, A. J. Danner, S. MAIER, J. Teng, "A High Contrast Silver/Nickel Superlens Characterized by Photon Scanning Tunneling Microscopy," *ICMAT 2011* (oral presentation), ICMAT11-A-1641 (S3-5), Suntec Convention Centre, Singapore, June 26 - July 1, 2011.
18. Y. Liu, G. Y. Si, E. S. P. Leong, B. Wang, A. J. Danner, X. Yuan, J. Teng, "Optically Tunable Plasmonic Color Filters," *ICMAT 2011* (oral presentation), ICMAT11-A-3487 (S9-6), Suntec Convention Centre, Singapore, June 26 - July 1, 2011.
19. G. Y. Si, E. L. S. Ping, A. J. Danner, and J. Teng, "Plasmonic coaxial Fabry-Pérot nanocavity color filter," [7757-127] PS1, *SPIE Optics + Photonics 2010*, San Diego, California USA (San Diego Convention Center), August 1 - 5, 2010.
20. J. Deng, G. Y. Si, and A. J. Danner, "Dry etching of $LiNbO_3$ using inductively coupled plasma," *Photonics Global 2010*, (Suntec Convention Center), Singapore, December 14 - 16, 2010.
21. G. Y. Si, E. J. Teo, D. Jun, A. A. Bettiol, J. Teng, and A. J. Danner, "Improved profiles of photonic crystals in lithium niobate by truncating tapered bottoms," *Photonics Global 2010*, (Suntec Convention Center), Singapore, December 14 - 16, 2010.
22. G. Y. Si, M. Zhang, S. L. Teo, J. Deng, J. Teng, and A. J. Danner, "Fabrication of single-layer metamaterials with sub-50-nm ultrasmall gaps," *Photonics Global 2010*, (Suntec Convention Center), Singapore, December 14 - 16, 2010.
23. G. Y. Si, M. Zhang, S. L. Teo, J. Deng, A. J. Danner, and J. Teng, "Tuning of surface plasmons in visible and near infrared range using plasmonic crystals," *Photonics Global 2010*, (Suntec Convention Center), Singapore, December 14 - 16, 2010.
24. G. Y. Si, A. J. Danner, J. H. Teng, S. S. Ang, and A. B. Chew, "Nanoscale arrays of lithium niobate fabricated by interference lithography and dry

etching," *ICMAT 2009*, Singapore: Materials Research Society, June 28 - July 3, 2009.

25. G. Y. Si, J. H. Teng, A. J. Danner, E. Dogheche, R. Yin, S. S. Ang, M. Y. Lai, A. Gokarna, A. Stolz, D. Decoster, and S. Y. Tan, "Fabrication and characterization of proton-exchanged waveguide on x-cut $LiNbO_3$," *IEEE Photonics Global*, Singapore, Dec. 8 - 11, 2008.
26. G. Y. Si, H. Y. She, J. H. Teng, A. J. Danner, "Enhanced Interaction of Plasmonic Nanocylinders and Other Cylindrical Structures", *the 2008 International Symposium on Antenna and Propagation (ISAP'08)*, No. 1645112, Taipei, Taiwan 2008.
27. H. Y. She, G. Y. Si, L. W. Li, "Light Scattering by Silicon NanoWires—Explanations of the Ignition Phenomenon by Analyzing Near-Field Energy Distribution", *the 2008 International Symposium on Antenna and Propagation (ISAP'08)*, No. 1644876, Taipei, Taiwan 2008.

Chapter-1: Introduction

1.1 Background and literature reviews

In 1981, the first lithium niobate ($LiNbO_3$, LN) waveguide with ultra-low loss was experimentally demonstrated by researchers at AT&T Bell laboratories using titanium in-diffusion techniques. Since then, LN has drawn increasing attention for years because of its peculiar optical properties, such as electro-optic, acousto-optic, and piezoelectric effects. Conventionally, a waveguide in LN crystal is fabricated using metal diffusion, ion exchange, or proton exchange (PE). Compared with the common titanium in-diffusion method, the PE process has a much higher photorefractive damage threshold for guiding visible laser light.[1] Furthermore, many proton sources have been used in the PE process, including benzoic, adipic, stearic, octanoic, and glutaric acids and their mixtures.[2-4] In addition, the fabrication of LN photonic crystals (PCs)[5-7] could find applications in decreasing the size of some crucial components in many optical systems. A feasible way to fabricate suspended waveguides in LN is to combine implantation, wet chemical etching and focused ion beam (FIB) milling techniques. FIB is a versatile and powerful instrument which can define patterns down to the nanoscale without using masks. This maskless lithography technique has been widely applied to manufacture electronic and photonic components with highly controllable parameters, leading to a great variety of applications. The FIB system utilizes ions (gallium, usually) produced by a liquid-metal source to scan over a sample surface and sputter away bulk material. The collision between ions and atoms results in surface alteration of different levels which

are mainly impacted by ion beam variables, such as overlap, dwell time, dosage and so on. However, FIB can be expected to produce sharp features and achieve high resolutions by precisely controlling the beam variables and obtaining optimized conditions.

A buried sacrificial layer below the sample surface can be generated directly by ion implantation due to lattice damage which results in a large etch selectivity relative to the bulk LN. Using FIB etching, varying patterns can be fabricated in LN to make chemicals contact the sacrificial layer during wet etching. Fig. 1-1 shows the scanning electron microscope (SEM) image of micro-pillar tops obtained in an x-cut LN. Details of how to develop a new method of fabricating suspended waveguides in LN and further shaping the device profiles will be discussed in this work.

However, even with advanced fabrication methods, the development of normal dielectric waveguides is limited by basic physical laws such as the diffraction limit. New types of waveguides are needed. For example, plasmonic waveguides have found significant applications in recent years and even replaced normal dielectric waveguides in some optical devices thanks to their ability of manipulating light at sub-wavelength scales. They also have great potential for creating different optical components such as switches, modulators and sensors. The spectrum of a plasmonic nanostructure is decided by its collective electronic oscillations and the plasmon modes are determined by its composition, scale and shape. Particularly, plasmonic coaxial apertures and nanorods have drawn considerable attention because of their great potential as important candidates for ultracompact optical devices.

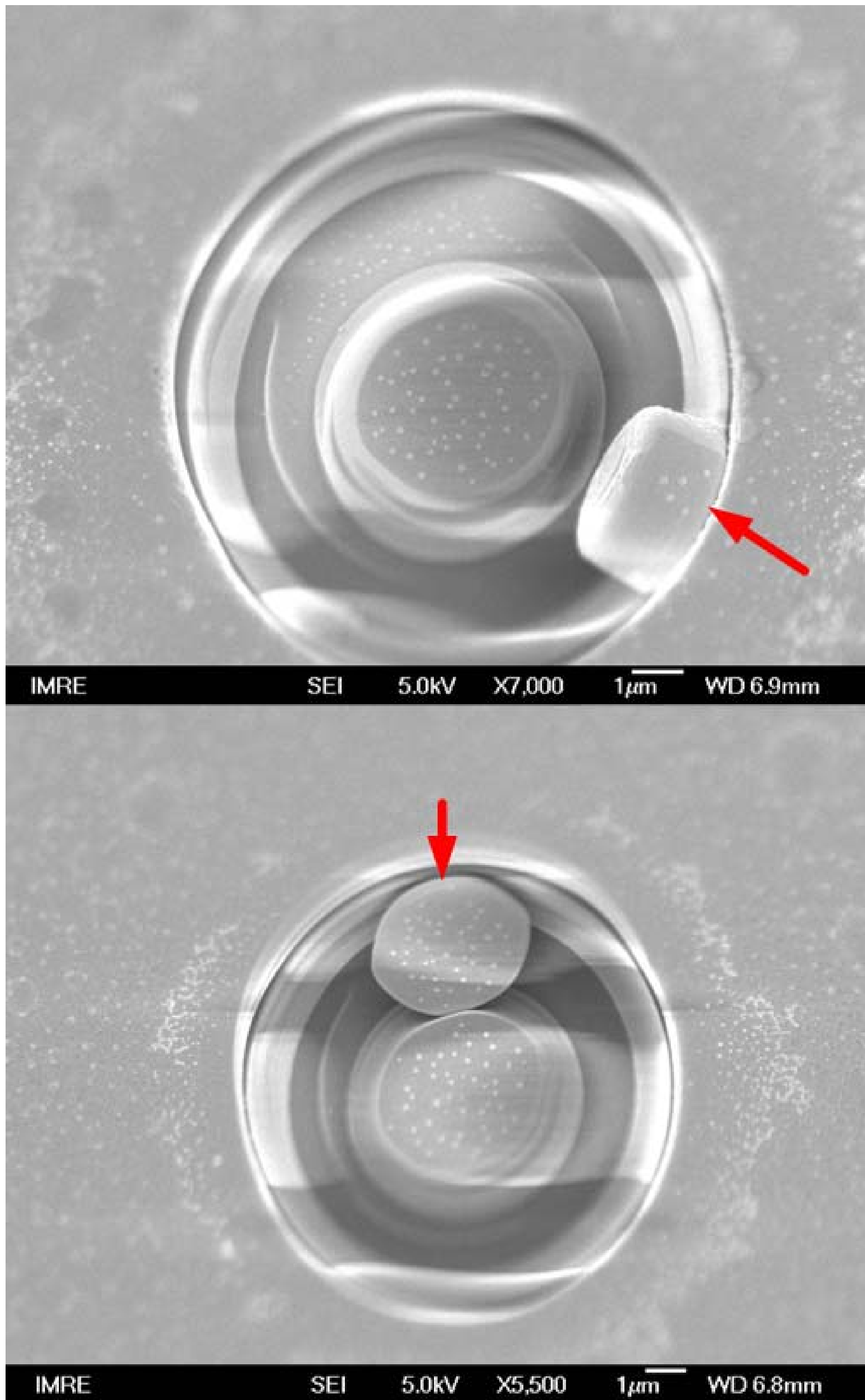

Fig. 1-1. SEM images showing lifted-off pieces of pillar tops in an x-cut LN.

Tuning of surface plasmons in the visible range is critical and essential to develop nanophotonic devices like color filters, modulators and sensors. Among all

these applications, color filters are of special importance because of their great potential for display and imaging. In digital imaging devices, typically three primary color components (red, green, and blue) are needed and balanced in each pixel to generate desired colors. Recently, plasmon assisted imaging devices have drawn increasing interest. In this thesis, color filters working under both transmission and reflection testing modes will be demonstrated and induced transparency observed from ultra-small plasmonic gaps will also be discussed.

1.2 Research motivation

Traditional methods of fabricating LN-based devices using slicing and wafer bonding are time-consuming and complicated. The structure is complex and the process is achieved at a high cost. For pulsed laser deposition techniques, the evaporated thin films are normally amorphous which means no crystal properties can be realized. Thus, how to fabricate usable devices in LN at a reasonable cost becomes a critical issue which confines the applications of this material. The new method developed in this work, techniques combining implantation and etching, paves the way for new generations of LN based devices since it does not involve slicing or bonding and is entirely monolithic.

Research on surface plasmons covers a broad scope with potential applications ranging from waveguiding to sensing. But plasmon assisted color filters are rarely reported especially the ones working under reflection testing mode. Using suitable fabrication methods, color filters working under both transmission and reflection

testing modes are demonstrated here. Thus far, manufacture of plasmonic nanostructures is mainly realized by using electron-beam lithography (EBL) and FIB. In this thesis, both techniques will be investigated. Advantages and limitations of each technique are also discussed. For example, FIB is capable of defining nanostructures on almost all kinds of materials with ultra-small gaps and ultra-high aspect ratios but limited mainly by re-deposition effects which result in non-vertical sidewalls. Different from FIB, EBL can define patterns only in electron resists. Therefore, it is normally combined with lift-off or dry etching to transfer patterns. In this work, FIB is used to define nanoring transmission-type color filters and EBL followed by ion milling is applied to transfer nanorod patterns to fabricate reflection-type color filters since it is impossible to produce dense and high-aspect-ratio structures by lift-off.

1.3 Thesis outline

Chapters 2 and 3 show how to fabricate suspended slab waveguides in LN and improve the device performance by shaping the device sidewalls. Monolithic fabrication of PCs in LN with high aspect ratio and uniform profiles is experimentally demonstrated. Different geometries with various lattices in bulk LN are also shown.

Chapter 4 demonstrates the fabrication and optical characterization of coaxial structures formed by both air and metal using FIB and standard EBL. Single layer metamaterials with high fabrication quality are shown. Dense nanorod arrays are also obtained using different techniques. Note that the FIB 200 system (FEI Company) was employed in this work.

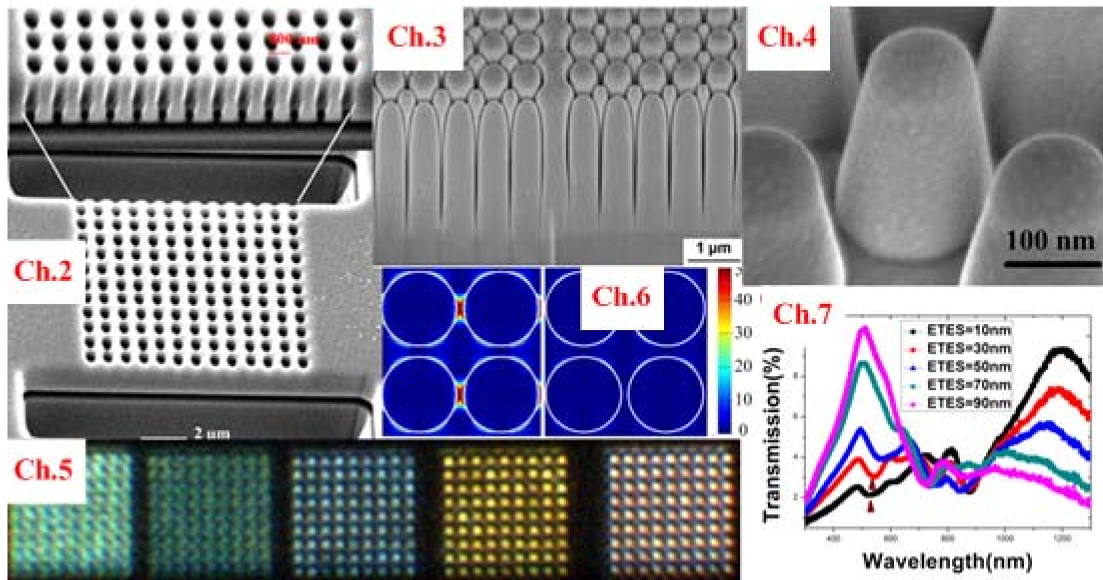

Fig. 1-2. Pictorial overview of this thesis.

Chapters 5 and 6 discuss color filters working under transmission and reflection modes using coaxial apertures and dense nanorods, respectively. Effective and fine tuning of resonance peaks through precise geometric control of the aperture dimensions is demonstrated. The dependence of reflected intensity on inter-rod spacing is determined and then utilized to develop a plasmonic crystal color filter using dense silver nanorods with ultrasmall spacings. Individual colors are finally filtered out using nanorod arrays with different periodicities.

Plasmon-induced transparency is discussed in Chapter 7. Plasmonic crystal designs consisting of different lattices which can exhibit induced transparency in the reflectance spectrum at visible frequencies are proposed and experimentally demonstrated.

Future work is proposed in Chapter 8, including further improving device performance and fabricating tunable plasmonic devices and three dimensional (3-D) metamaterials. Fixed beam moving stage (FBMS) lithography technique is proposed

to fabricate straight waveguides without stitching errors. Tunable plasmonic devices are also achievable via a pumping light (UV light source, normally) control using liquid crystals (LCs).

Chapter-2: Suspended Slab and Photonic Crystal Waveguides in LN

Suspended waveguides have been widely applied to silicon-on-insulator structures because they are easily fabricated with processing techniques similar to those of integrated circuit designs. However, it is difficult to fabricate such structures in LN which is also a very important material for optoelectronics. One main challenge is the difficulty of etching LN. In this chapter, a novel method will be shown to fabricate suspended slab waveguides in LN by combining ion implantation, FIB milling and selective wet etching techniques. The method does not involve wafer bonding or crystal ion slicing and is entirely monolithic. Lattice damage can be introduced to a buried thin layer of a certain depth beneath sample surface by ion implantation, resulting in a considerable wet etching selectivity to bulk material. The etching rate has been investigated to control the size of the suspended membrane. Fabrication of suspended PC waveguides has also been demonstrated. The results show an effective method of fabricating suspended devices in LN, which enables new applications such as waveguides, modulators and infrared detectors.

2.1 Waveguides in LN and traditional etching methods

Waveguides in LN are used for high-speed modulation or for nonlinear devices such as parametric oscillators and amplifiers. LN is also common in telecommunication systems due to its high electro-optic coefficient and low optical losses. Moreover, LN is an important ferroelectric material which is extensively used in optoelectronic and surface acoustic wave devices. However, it is quite difficult to etch LN due to its poor reactivity with common etchants and selectivity issues.

There are two normal ways of LN etching, wet etching and plasma etching. Wet etching is a frequently used processing step but is seldom applied to LN because of the material's strong etch resistance which results in low etch rates and sometimes inhomogeneous etching.[8-12] Introduction of structural defects can speed up the etching considerably, therefore the combinations of ion bombardment and subsequent wet etching have been demonstrated as a useful method for etching of LN. For plasma

etching, the main limitation is the redeposition effect which will lower the etching rate when fluorine gases are involved. To improve this, a proposed way is using the mixture of fluorine gases with argon or oxygen. Previously, a maximum etching rate without cooling of 5.7 μm/h was obtained with CHF_3/Ar.[10] Recently, an optimized SF_6/Ar mixture was applied to provide etching rates of up to 190 nm/min.[11]

In particular, PC slab structures in LN would offer the possibility of realizing high-density integrated optical systems and low-loss large-bandwidth connectivity between different components in integrated circuits on an active material. The optical properties could then be modified externally through an applied electric field, for example, offering fast tunability of PC devices. Because the Pockels effect in LN is much faster (and loss is lower) than carrier-induced index changes in silicon-on-insulator (SOI)[13-15] structures, for example, the method described in this chapter could allow applications requiring ultrahigh switching speeds in LN that would be impossible to achieve in other materials.

The buried oxide in SOI devices can be easily removed by a selective wet etch. By replacing the out-of-plane asymmetric structure (air-silicon-silicon dioxide) by a symmetric frame (air-silicon-air), the propagation loss can be reduced remarkably. Light is tightly confined in the waveguide during propagation. Besides, it can provide high density integration of optical components due to strong light confinement and tailorable dispersion. Similar methods can be applied to GaAs/AlAs systems by oxidizing the AlAs and undercutting with a wet etch. No such methods are normally available in bulk LN.

In this chapter, the fabrication of suspended membrane and PC structures in LN will be demonstrated. This method can effectively be applied to bulk LN wafers, which are typically of much higher quality than epitaxial LN. Effective wet etching of implanted LN after the formation of a buried sacrificial layer beneath the sample surface induced by ion damage will also be shown. This approach opens a new era of LN-based device design.

2.2 How to fabricate suspended waveguides in LN

In the past, ion implantation techniques have been applied to LN together with a wafer bonding method to transfer a thin film of LN to another substrate such as silicon or gallium arsenide to make a slab waveguide.[16,17] X-ray probing can be applied to map elastic strains caused by implantation.[18] The refractive indices and the electro-optical coefficient of the fabricated thin films have also been studied elsewhere.[19,20]

Recently, ultrathin membranes are available in x-cut LN[21] and the PCs in an ion-sliced LN film with a soft underlayer have been characterized.[22] Devices fabricated using such a method have advantages over normal waveguides fabricated by etching proton exchanged or metal diffused LN because they not only have low loss and tight optical confinement, but also enable the fabrication of PC structures. A new process will be developed: A buried sacrificial layer below the sample surface can be generated directly by ion implantation due to lattice damage which results in a large etch selectivity relative to the bulk LN.

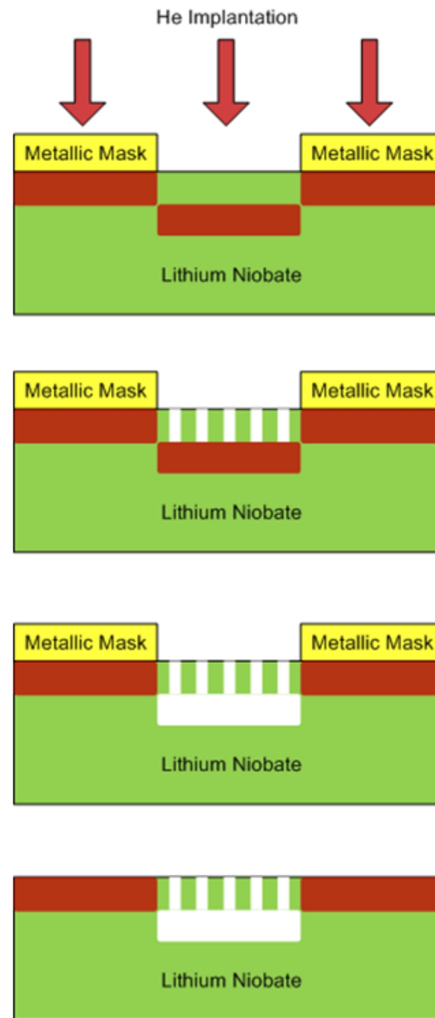

Fig. 2-1. Illustration of the process steps to create suspended structures in LN using ion implantation, FIB milling and selective wet etching.

The schematic drawing showing the process flow is illustrated in Fig. 2-1. First, He^{+} ions with 1 MeV beam energy were implanted normal to the surface of a z-cut LN sample. According to the Stopping and Range of Ions in Matter (SRIM, http://www.srim.org/) simulation shown in Fig. 2-2 (a), the damage is rather constant and low for the first 2 μm from the surface, and increases sharply by 20 times at the end of range of 2.4 μm. For a dose of 1×10^{16} ions/cm^{2} used in this experiment, this corresponds to a damage of 4×10^{20} vacancies/cm^{3} created near the surface and a maximum of 8×10^{21} vacancies/cm^{3} created at the end of range.

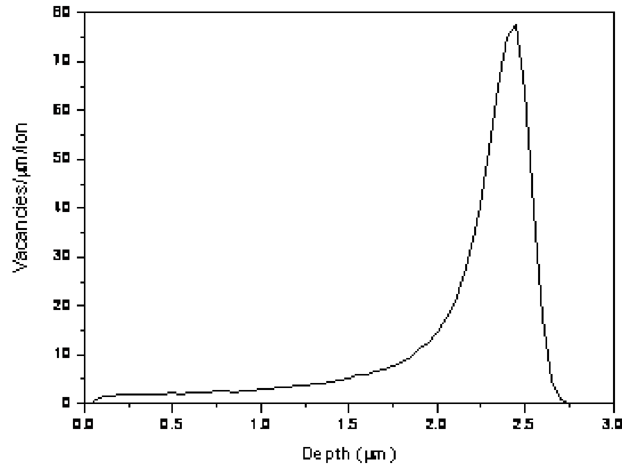

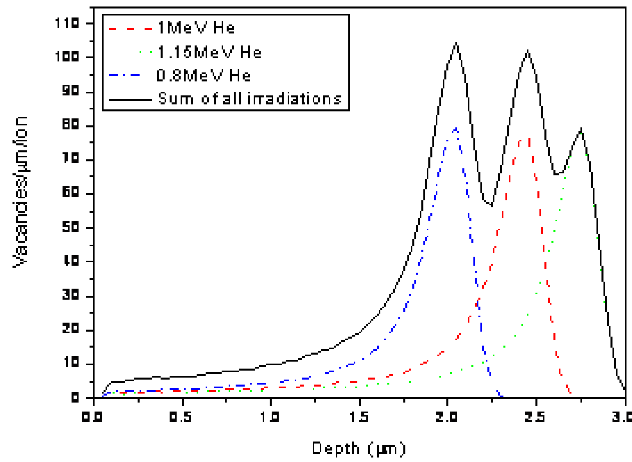

Fig. 2-2. (a) SRIM simulation of 1 MeV He^+ in LN. (b) SRIM simulations of 0.8, 1, and 1.15 MeV He^+ in LN.

The lattice defects introduced by implantation make it chemically active towards selective etching compared to a perfect crystal. Fig. 2-3 shows that selective etching occurs only near the end of range, producing a 2 μm thick LN slab that is suspended in air with a gap thickness of about 350 nm. Contrastively, the un-implanted area is barely etched. The sample was first FIB milled to pattern a rectangular hole and then immersed in mixed acids to etch away the sacrificial layer. To prevent light leakage into the substrate, a thicker air gap may be needed. This can

be obtained by using multi-energy irradiations to produce overlapping Bragg peaks to increase the etched layer thickness.

Fig. 2-2 (b) shows that the thickness of the etched layer can be increased to 1 μm by using irradiations with three different energies (0.8, 1, and 1.15 MeV). After implantation, rectangular patterns were milled by FIB etching in the implanted area which also exposed the sacrificial layer to chemicals during wet etching. During FIB milling, gallium ions with 30 kV acceleration voltage were emitted and focused on sample surface. The probe current was 350 pA and the spot size was about 55 nm. Finally, the sample was immersed in a mixture of 65% HNO_3 and 49% HF (2:1) for various times to etch away the damaged layer, leaving suspended structures consisting of a LN slab vertically surrounded by air. The process is simple and monolithic. Optical lithography or EBL combined with ICP etching can also be used to mill the pattern prior to wet etching the undercut region.

2.3 Results and discussion

The SEM image of a rectangular hole milled by FIB on the edge of the implanted area after wet etching is shown in Fig. 2-3. The picture was taken at a glancing incidence of 35 degrees to normal. One can observe the undercut structure clearly which is caused by selective wet etching. The layer of sacrificial LN replaced by air has a tapered shape, indicating a selectivity of the sacrificial to the bulk. Images of a post structure fabricated by ring FIB milling of 8 μm diameter before and after wet etching are demonstrated in Figs. 2-4 (a) and (b), respectively.

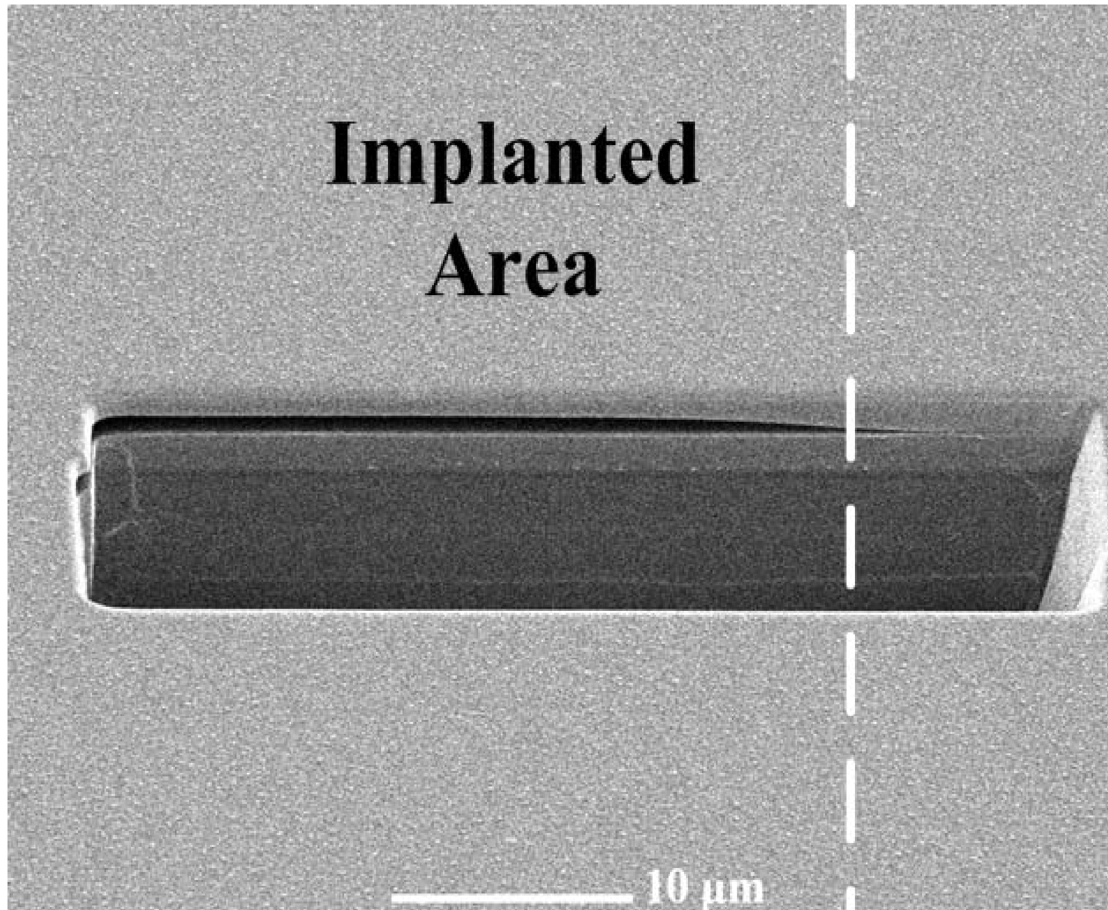

Fig. 2-3. SEM image of a rectangular hole patterned on the edge of implanted area.

However, in Fig. 2-4 (a), one can see the surroundings of the milled ring are damaged because of a large probe current during milling. In addition, it is evident that the profiles are not vertical, which is common in FIB milling. Improving the anisotropy of the milled structures is also a motivation of this work. One can make the etched profiles more anisotropic by truncating the bottom, more tapered portions of the milled structures when wet etching to achieve suspended structures. In order to investigate the etching rates and control the size of the suspended membrane, different wet etching times were applied and then cross sectional views were obtained by a second FIB milling.

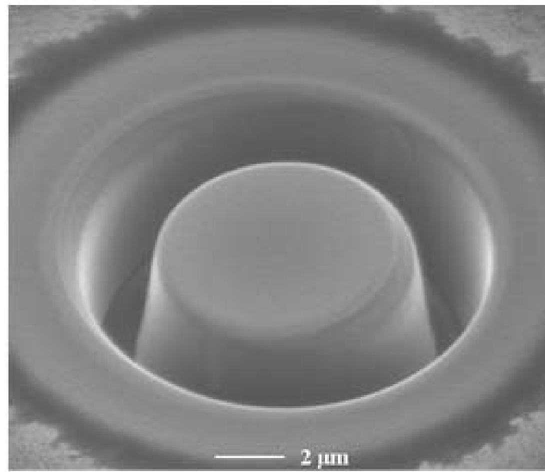

(a)

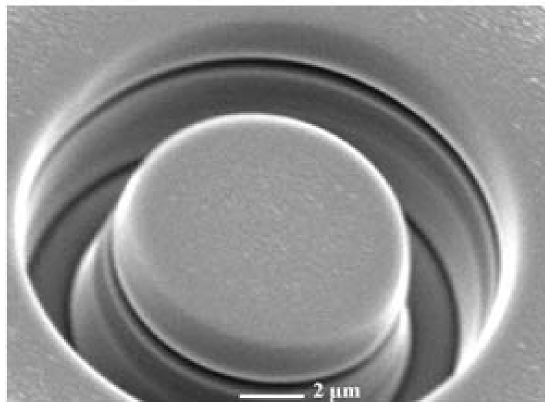

(b)

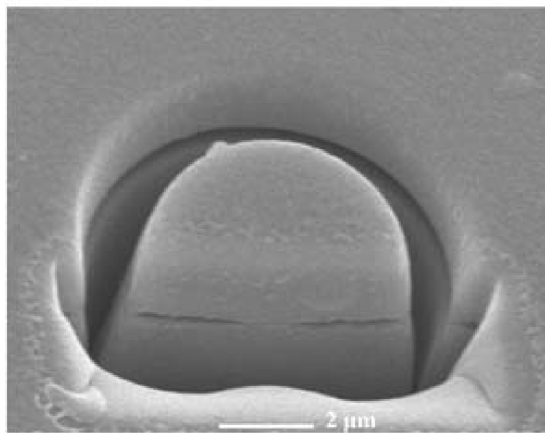

(c)

Fig. 2-4. (a) FIB image of a post after milling and before wet etching. (b) SEM image of a post after wet etching. (c) SEM image showing the cross-sectional view.

Fig. 2-5 (a) shows the cross sectional SEM image of a slab after 10 min of wet etching. The measured etching rate is ~100 nm/min, as shown in the inset with a larger magnification to demonstrate more details. There are tiny spots interspersed on

the sample surface caused by material redeposition during milling. For conventional waveguides in LN fabricated by PE, the propagation loss is high due to light leakage caused by poor refractive index contrast. Once the buried sacrificial layer is removed by the etchants, a symmetric cladding structure (air-LN-air) is formed, which can significantly enhance light confinement in the waveguide as well as reduce the propagation loss. To make a larger area of suspended slab, one can simply extend the wet etching time. The cross sectional profiles of a slab and a post after 20 min of wet etching are shown in Figs. 2-5 (b) and 2-4 (c), respectively. The suspended slab is almost separated from the substrate by the etch. Note that the etching profile has a slightly tapered shape. This is because the outer part has been exposed to etchants for a longer time than the inner part, but it is also evident that this is not a serious problem and that the selectivity is generally quite uniform, even with long undercuts (which are not needed in PC-based structures).

Suspended PCs in a LN slab are shown in Fig. 2-6. The 13×12 hole array with lattice constant a = 800 nm and hole radius r = 0.175a was milled by FIB for ~ 30 min using a small probe current. Taking into account both the spot size of milling holes with such small features and a reasonable total milling time, a 70 pA probe current (25 nm spot size) was selected. The holes have been milled through the suspended membrane. The structure is anisotropic because the bottoms of the milled cones have been truncated by the buried air layer. Since the thickness of the buried layer can be controlled by the ion implantation process, one can easily change the parameters of fabricated suspended structures to tailor device performance.

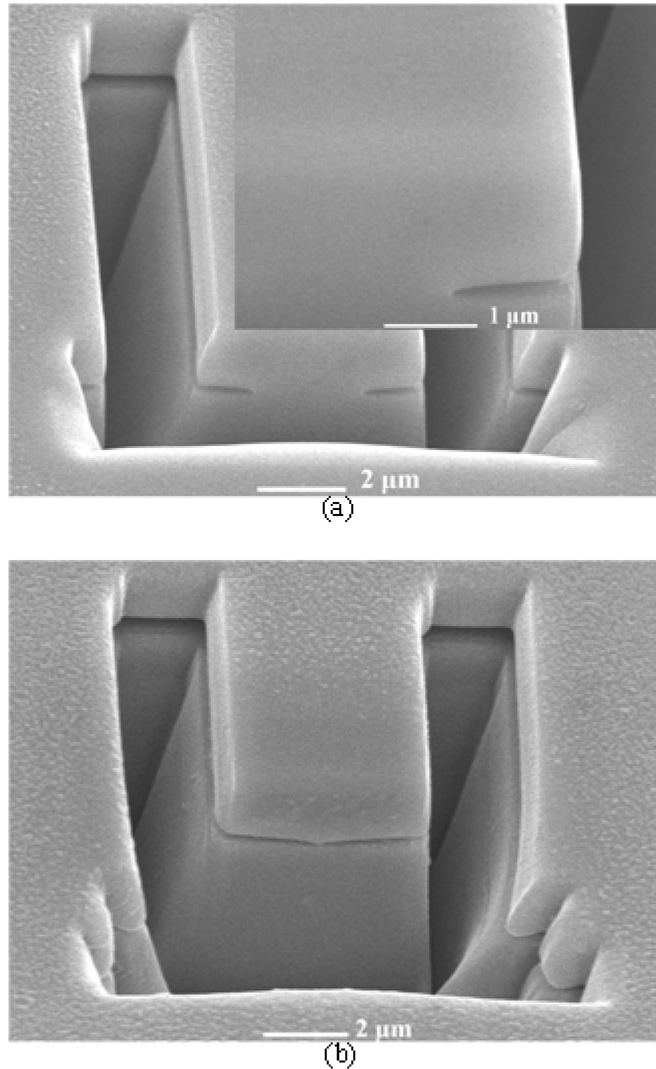

Fig. 2-5. Cross-sectional images showing the undercut after 10 min (a) and 20 min (b) of wet etching. The inset of (a) shows a further magnified view of the right part of the undercut structure.

The impact of a tapered shape on PC slab waveguides was theoretically investigated by Y. Tanaka *et al.*[23] and it was found that PC waveguides consisting of cone-shaped air holes exhibit a much larger propagation loss than in vertical air hole waveguides. The coupling between TE-like waveguide modes and TM-like slab modes is responsible for the large propagation loss generated by tapered PCs. Similar studies have also been performed by G. Burr *et al.*[24] recently. They experimentally verified that shallow tapered holes could be used as a broad-band attenuator.

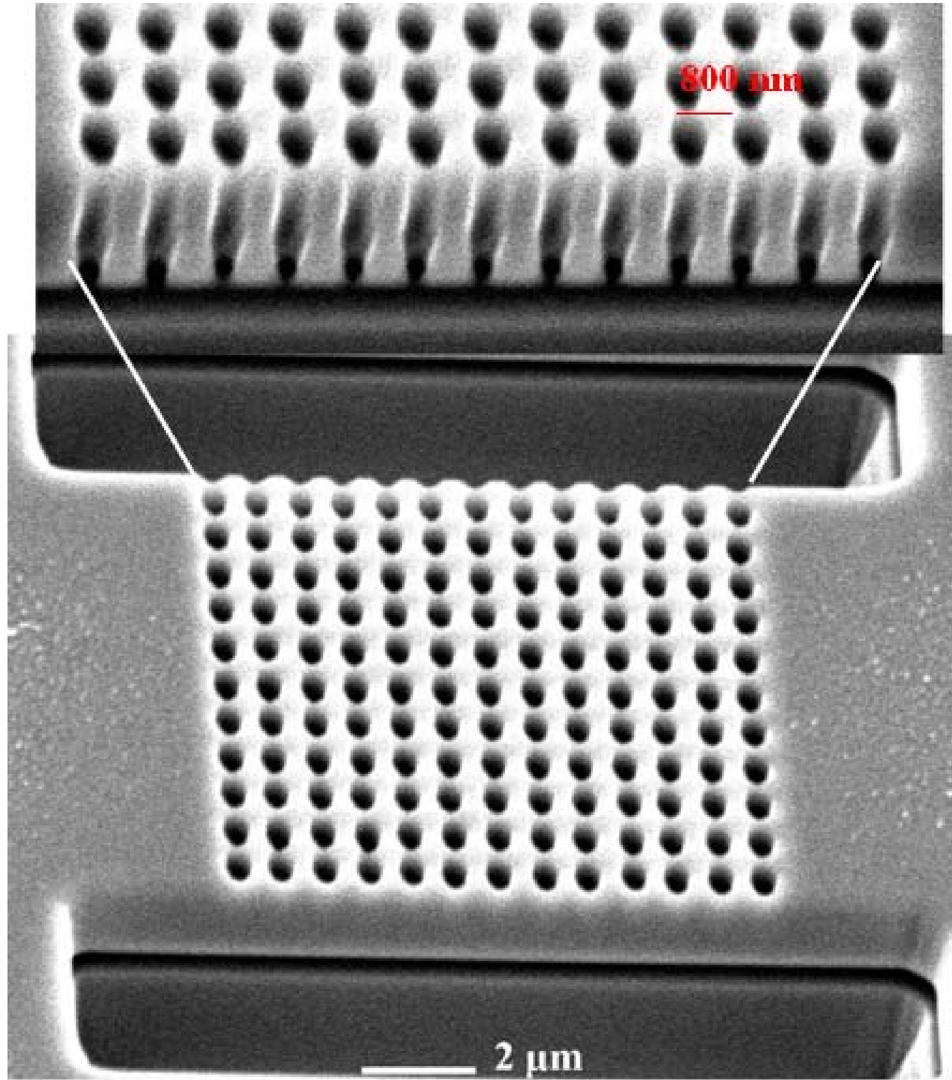

Fig. 2-6. Fabricated PCs in a suspended LN slab. All the holes have been milled through the slab.

Therefore, only holes with nearly vertical (less than 0.5° tilting angle) sidewalls could produce well-defined stop-bands in the transmission spectra. Thus, PC applications in LN require holes with vertical profiles to achieve an acceptable optical performance. Making the holes suspended can enable easy fabrication of vertical PCs because the bottoms of the tapered holes caused by redeposition during FIB milling would be truncated by an air gap. One can further minimize redeposition effects by coating a thin layer of metal before FIB milling and then wet etching to

remove the metal together with redeposited material after FIB milling. In addition, one can also fabricate large area PCs with high aspect ratio by applying ICP etching on suspended LN membrane. After truncating the bottoms of the cone-shaped holes, only the top parts with a uniform profile are left in the suspended membrane, which can further give rise to better performance. The ion implantation could also take place at multiple energies within the same sample, creating complicated layered structures of high index contrast when undercut.

2.4 Chapter summary

In summary, a novel method has been investigated to fabricate suspended structures in LN, including normal slab waveguides and PCs. After generating lattice damage with ion implantation, FIB milling was employed to make the buried sacrificial layer exposed to etchants during wet etching. Using this method, one can fabricate a suspended structure in LN without applying ion slicing and wafer bonding to transfer thin films, therefore avoiding thermal mismatch-induced stress during heating and cooling steps. Monolithic fabrication of large area PCs with high aspect ratio and uniform profiles is now realizable in LN.

One critical factor which can determine the performance of the fabricated waveguides is the profile of the PCs. Thus, it is important to control the device cross section and aspect ratio, which will be described in detail in the next chapter.

Chapter-3: Ultrahigh Aspect Ratio Waveguides in LN

In this chapter, fabrication of novel patterns based on LN using FIB milling will be shown. When an array of small holes is etched, a severe tapering problem is observed as is common, but by replacing the nanocylindrical hole array with a nanoring structure, PCs with an aspect ratio up to 50:1 (2 μm total etching depth and 40 nm gap aperture) can be obtained. Dense nanorod arrays with sub-30-nm ultrasmall gaps and more than 2.5 μm depth are also achieved with FIB milling.

3.1 PCs in LN and FIB technique

LN is notoriously difficult to etch and the fabrication of various waveguide structures like right-angle bends, T-junctions and PCs typically requires the use of high-index contrast structures. Such structures require robust LN etch processes. PCs, for example, offer the possibility of realizing high-density integrated optical systems but are among the most difficult to fabricate in LN. The fabrication of LN PCs would provide a way of significantly decreasing the size of crucial LN components in optical communication systems, which are generally quite large due to the use of diffused waveguides when fabricated in LN. Since LN exhibits a strong Pockels effect, tunability of PCs could be achieved simply by applying external electric fields.[7,25]

FIB lithography is a frequently used technique to fabricate PCs in LN.[26,27] Since PCs require vertical optical confinement, a potential approach for achieving this in LN would be to implant a bulk LN sample followed by thin film transfer (crystal ion slicing and wafer bonding).[17,28] Fabrication of suspended slab and PC waveguides by implantation and wet etching has been investigated previously.[29] Therefore, it is worth investigating dry etching methods in LN for creating lateral index steps which are useful for a wide range of devices.

The FIB instrument is a useful tool based on ion beam-solid interactions.[30] Equipped with a liquid ion source, it can define patterns directly without using masks. In addition, since FIB lithography can be applied to almost all kinds of materials, it has found extensive applications in manufacturing semiconductor devices.[31,32] Due to its versatile and reliable properties, fabrication of 3-D structures was also achieved elsewhere.[33,34]

In this chapter, improving the profiles of PC structures by developing different patterns using FIB lithography will be demonstrated. Nanorings with over 50:1 aspect ratio are realized. All patterns are fabricated with good uniformity and high homogeneity. Furthermore, nanorod arrays are fabricated by increasing the outer radii of ring structures and realigning the ring array patterns as will be described. Ultrasmall gaps with less than 30 nm width are also achieved. Gap apertures can be simply tuned by varying the overlapping area.

3.2 Nanoholes with standard profiles

A common problem of using FIB milling methods is tapered sidewalls, caused by redeposition during etching which is inevitable. Straight sidewalls are preferred. To demonstrate the redeposition effect, a typical 2-D planar PC structure was fabricated. 100 nm gold with 5 nm titanium as adhesion layer was first deposited on an x-cut LN sample surface by electron beam evaporation to avoid charging problems during FIB milling. Then all the hole patterns were milled in parallel to minimize the redeposition effect using a 70 pA probe current with a 30 kV acceleration voltage.

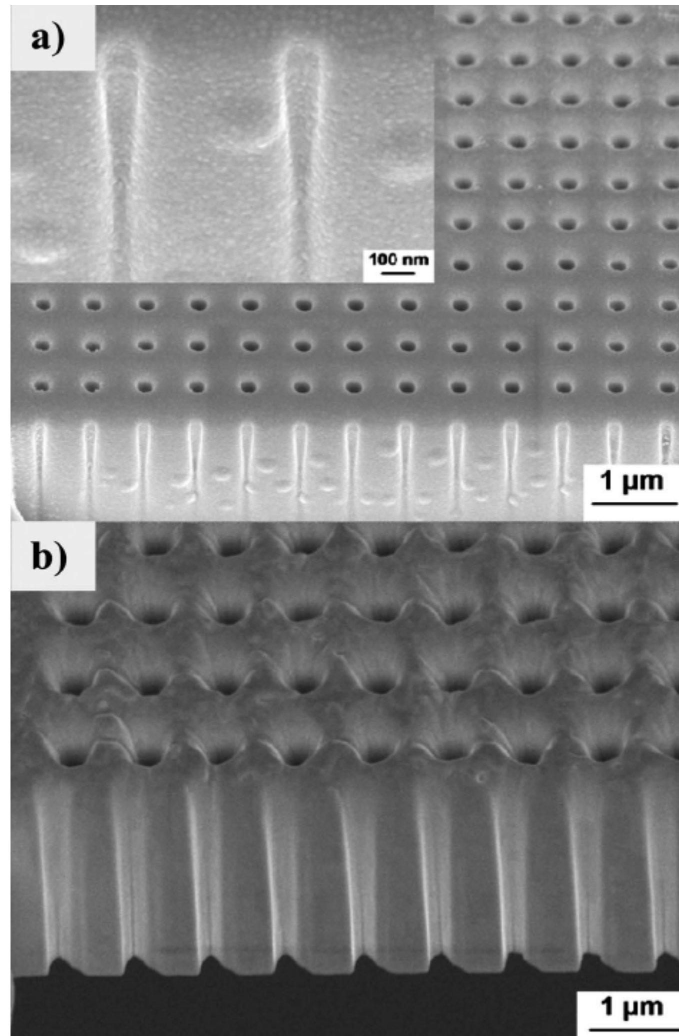

Fig. 3-1. (a) SEM image showing the tapered cross-sections of nanoholes. (b) Cross section of PCs in a suspended LN film fabricated by implantation, FIB milling and wet etching. Note that these two hole arrays have different periodicities.

The metals on sample surface also function as protective layer during scanning and milling to minimize ion damage to the LN surface. One should also note that it is easy to remove all redeposited materials after milling by simply removing the metals to obtain a clean LN face.

Fig. 3-1 (a) shows a typical cross sectional profile of nanoholes fabricated in a LN sample by FIB milling. From the inset of Fig. 3-1 (a), one can observe profiles with a serious tapering shape which is common in FIB milling due to material redeposition. One can also find bubbles interspersed among the sidewalls. Tapered

profiles could affect optical device performance dramatically, so this represents a serious problem as large optical losses may be caused.[23,24]

One potential solution is to truncate the tapered bottoms to minimize the impact generated by gradient shapes by making the holes suspended using combined techniques of implantation, FIB milling and wet etching as shown in a previous work.[29] Fig. 3-1 (b) demonstrates the cross section of PCs fabricated in a suspended LN film with severely tapered bottoms truncated using combined techniques mentioned above. To further show the improvement and accurately measure the angles, new experiments (after the first submission of this thesis) were carried out using a dual-beam FIB system (Nova NanoSEM 230, FEI Company). As shown in Fig. 3-2, almost vertical (89.7°) sidewalls are achieved and cone-shaped bottoms with 24.3° and 37.9° are also shown in the same image for comparison.

One can find significantly improved profiles of the cylindrical structures. Nonetheless, simply etching holes will always lead to a tapered profile, resulting in large propagation losses. As will be described, other shapes (rings, for instance) do not necessarily suffer from the same effect.

3.3 Nanorings with ultrahigh aspect ratio

To further investigate the feasibility of fabricating high aspect ratio PCs with homogeneous etching profiles, coaxial ring-like structures by direct FIB patterning were developed. As illustrated in Fig. 3-3, a series of two-lattice superimposed PCs with fixed inner radius (nominally 80 nm) and varying outer radii (140 nm to 260 nm in 40 nm increments) were fabricated.

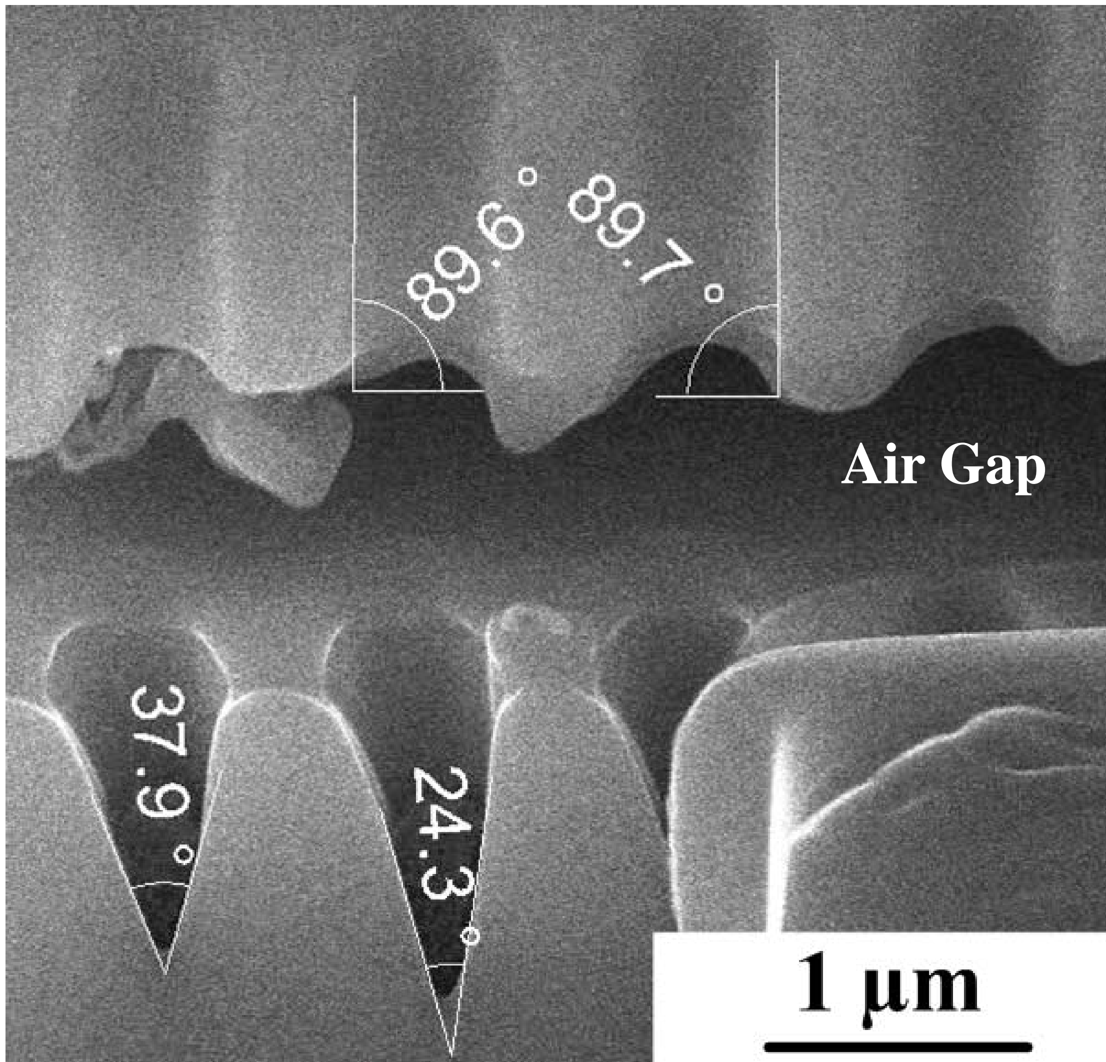

Fig. 3-2. SEM image showing nearly vertical sidewalls of holes with labeled angles in comparison with seriously tapered bottoms.

The spot size of an ion beam is determined by many factors, such as dwell time, beam overlap, focus, stigmatism and especially the probe current. Taking both the total etching time and desired features into account, an 11 pA probe current was selected to mill the ring patterns in this work. This corresponds to a 15 nm spot diameter. The total milling time for a 9 × 9 ring array was approximately 5 min. By replacing the nanoholes described in Section 3.2 with ring structures, the milled profiles can be improved remarkably and uniform cross-sections can be obtained with a high aspect ratio.

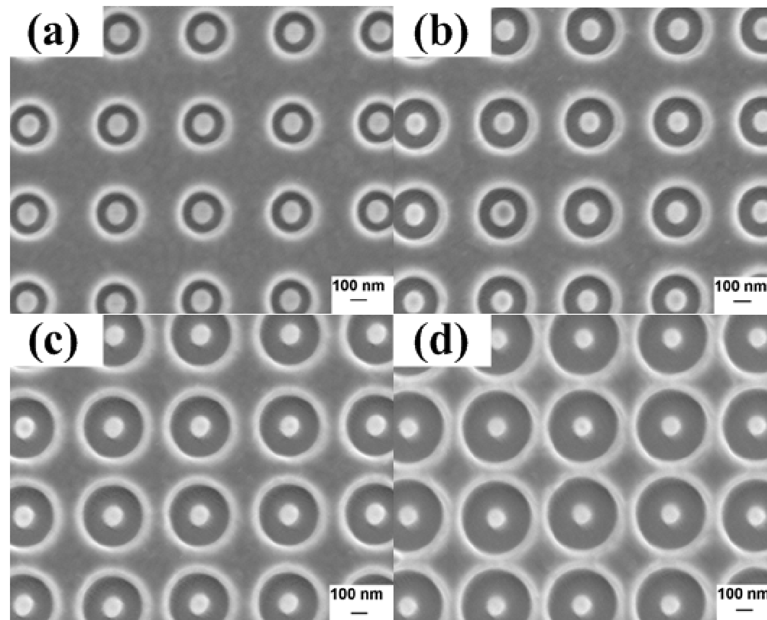

Fig. 3-3. Top view SEM images of ring structures with fixed inner radius (80 nm) and varying outer radii (a) 140 nm, (b) 180 nm, (c) 220 nm, and (d) 260 nm.

As demonstrated in Fig. 3-4, nanorings with a 40 nm gap aperture (200 nm inner radius and 240 nm outer radius, respectively) exhibit good uniformity with 50:1 aspect ratio (over 2 μm total etching depth). One can observe straight ring apertures as shown in the cross sectional view in Fig. 3-4 (b). Since post-etch FIB cross sectioning processes can cause etches to appear deeper than they actually are (phantom etches) during the cross sectioning process, these were also investigated in the next section to ensure the aspect ratio was not an FIB cross sectioning artifact and were truly a result of the initial FIB milling. In addition, one can control the aspect ratio by simply varying the geometry of the ring arrays to make PC structures with different effective indices for various applications.

It appears that ring shapes are much more resistant to the tapering effect than standard holes, and this is the primary motivation for this work, as this property may be important for fabrication of various nano-scale devices with FIB milling.

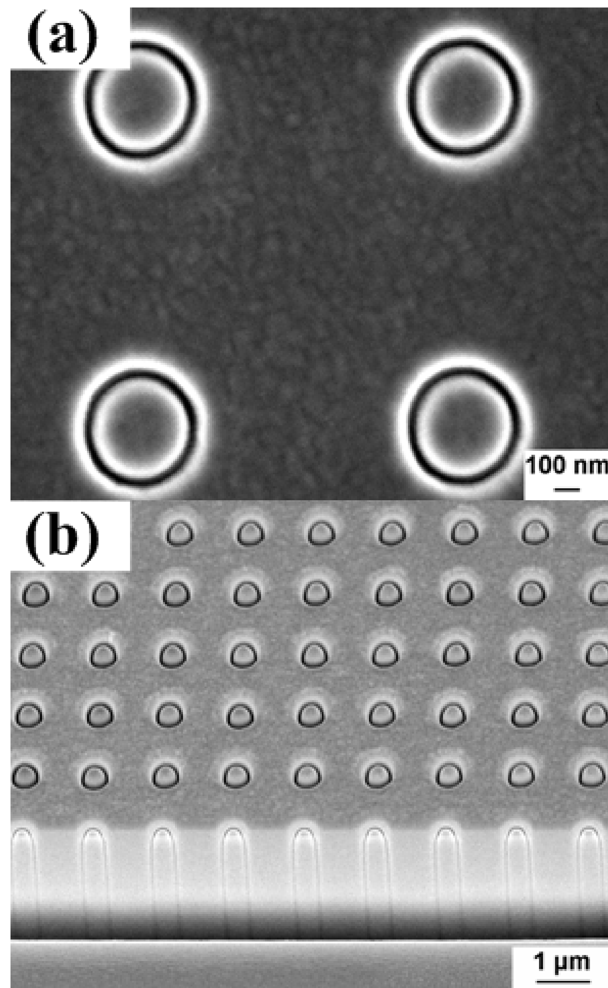

Fig. 3-4. (a) Top view of the nanoring arrays with 200 nm inner radius and 240 nm outer radius. (b) Cross sectional view showing the straightly etched ring apertures.

The tapered cross sectional profiles are mainly caused by redeposition problem which is inevitable during milling. Tapered holes will generate high optical losses and they could hardly produce well-defined stop-bands in the transmission spectra. One proposed solution is to truncate the tapered bottoms and reshape the cross sections using appropriate techniques. Another potential approach is to replace cylindrical holes with coaxial structures which have been studied for decades.[35,36] More beam energy can be concentrated in the ring area which results in reduced energy spread and total etching time during the FIB process, enabling small features and large etching depth simultaneously.

Coaxial geometries can be used to guide light around sharp bends since the radial confinement of the light is a consequence of omnidirectional reflection instead of total internal reflection.[37] Coaxial holes can also be used to create PC structures with similar characteristics to those of standard air hole PCs.[38] They have been used to create waveguides with polarization-independent guiding effect[39] and a complete photonic band gap[40,41] most recently. More designs and fabrication work have been investigated elsewhere.[42,43]

3.4 Nanorod arrays by FIB milling

By further increasing the outer radii and realigning the ring arrays, we can obtain nanorods with different shapes by FIB milling. Fig. 3-5 shows a glancing view of dense nanorod arrays with different lattices. Although one can observe coniform tops for the nanorods, gaps between individual crystals become uniform from 500 nm downwards. The coniform tops are caused by damage during long-time milling and scanning when adjusting system parameters to focus. Besides, the tapered profile is also attributed to the redeposition effect during milling.

The FIB technique is a maskless lithography method since ions can directly define patterns on a wide range of materials. It is feasible to manufacture a great variety of electrical and optical components by precisely controlling the beam variables, such as overlap, dwell time and so on. In addition, without producing forwardscattering and backscattering, a fine defined ion beam is capable of fabricating narrow line widths and structures at the nanoscale with high aspect ratio and accuracy, leading to fascinating photonic devices with various functions and applications.

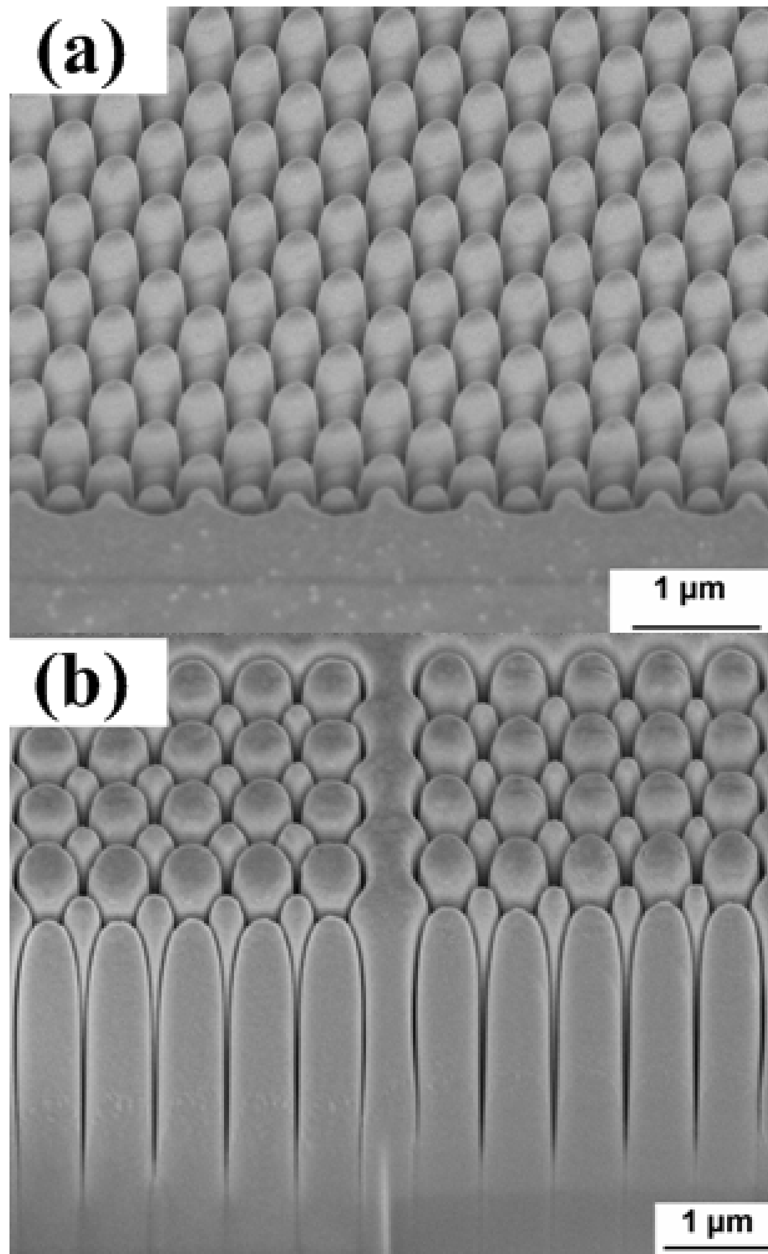

Fig. 3-5. (a) Glancing view of nanorod arrays with hexagon-shaped lattices. (b) Cross sectional view showing the bottoms of nanorods by a gradient milling at 15-degree.

Since a single beam FIB system (FIB 200, FEI Company) was employed in this work, we tried to reduce scanning time to minimize ion damage during navigation to a target region but some damage was unavoidable. There are no such problems for dual-beam (electron and ion sources) FIB systems because navigation can be performed using the electron beam instead.

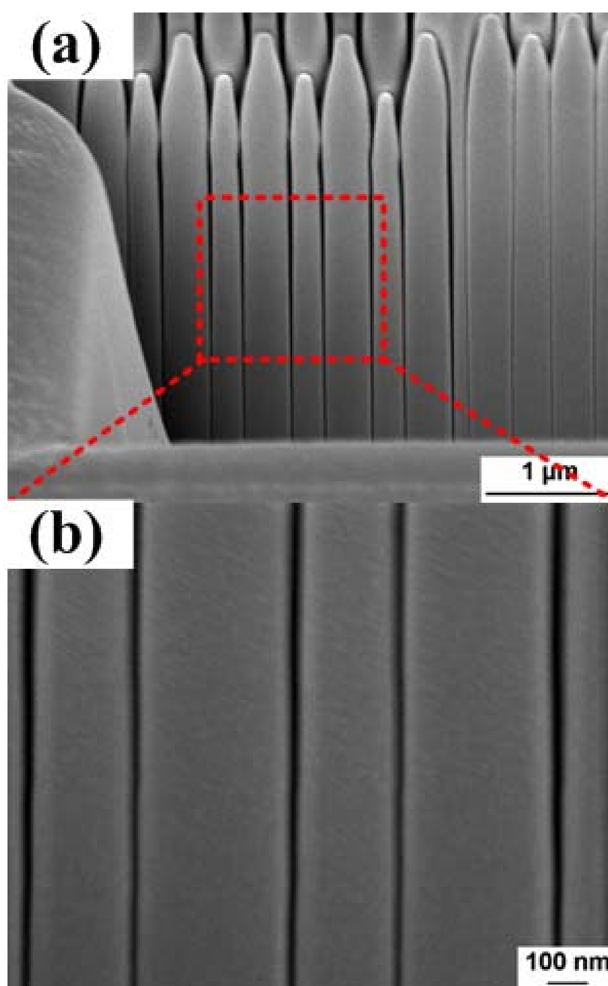

Fig. 3-6. (a) Low and (b) high magnification cross-sectional images showing vertically etched dense nanorods with less than 30 nm gaps and more than 2.5 μm etching depth.

To present the bottoms of the nanorods without showing any artifacts caused by FIB cross sectioning, a gradient milling at 15-degree tilting angle was applied to the rod bottom parts as illustrated in Fig. 3-5 (b). This shows the true etching depth achieved during initial milling by eliminating any potential additional vertical etching during the cross sectioning process. The aspect ratio reported above is repeated and thus verified. In this work, nanocavities obtained using such a method have ultrasmall gaps with quite a large etching depth. As shown in Fig. 3-6, dense pillar arrays have been fabricated with less than 30 nm gaps and ultra-high aspect ratios (more than 2.5

μm etching depth). Note that the damage for the patterns (especially the top parts) becomes severe as the milling time is extended (for deep etching).

3.5 Chapter summary

To conclude, tapered profiles of FIB milling method caused by redeposition have been investigated. By applying ring-pattern milling instead of simple hole milling, an ultra-high aspect ratio over 50:1 has been achieved. Once the ion energy is focused onto a smaller milling area on sample surface, dry etching can go much deeper with significantly reduced total milling time using a well-defined ion beam. Moreover, nanorod arrays with sub-30-nm cavity gaps have been fabricated using an improved and realigned ring-pattern milling function. Different geometries with various lattice shapes are available in bulk LN now. More importantly, one can tune the effective indices efficiently since both the inner nanorod diameter and the outer surrounding air filling factor are controllable. Fabrication of homogeneous PCs enables a new series of optical devices which can be easily applied to bulk LN.

All the device fabrication technique achievements in LN described above can be readily applied to metallic materials, leading to an emerging candidate for integrated optics and photonics: the plasmonic waveguide. The plasmonic waveguide can find important applications in negative refractive index cloaking, chemical-/bio-sensing, color filtering, and surface enhanced Raman scattering, as will be described in the following chapters.

Chapter-4: Fabrication of Coaxial Metamaterials and Nanorod Arrays

Plasmonic coaxial apertures are emerging candidates for single layer metamaterials at visible frequencies. Different mechanisms of extraordinary optical transmission can be observed from coaxial nanorings and they can support localized Fabry-Pérot plasmon modes. However, fabrication is a challenge due to difficulties of etching metals, especially for ultrasmall features with deep etching. This chapter demonstrates the fabrication and optical characterization of coaxial structures formed by both air and metal using FIB etching and EBL followed by argon ion milling. Single layer metamaterials with high fabrication quality are shown. Dense nanorod arrays are also obtained using different techniques to be described, which could find extensive applications in nanofocusing and imaging.

4.1 Fabrication tools for plasmonic structures

Surface plasmons (SPs) are electromagnetic waves propagating along metallic-dielectric interfaces and they have drawn considerable attention in the past ten years since extraordinary optical transmission (EOT) phenomenon was first reported in 1998.[44] They can take different forms, from propagating waves to localized electron oscillations. Owning to their unique optical properties and particular ability of manipulating light at sub-wavelength scales, a wide range of practical applications have been enabled. Since the near-field of electromagnetic waves can be enhanced significantly using plasmonic structures with different designs, SP based waveguides are of special importance for developing sensors with ultra-high sensitivity and figure of merit.

Most recently, coaxial structures have become an important candidate for single layer metamaterials in the visible range.[45-49]. Different from the mechanisms of EOT observed from subwavelength cylindrical nanoholes, such ring-like structures can support propagating plasmon modes due to strong Fabry-Pérot resonances. More

theoretical investigations of coaxial structures can be found elsewhere.[50-54]

To date, most plasmonic devices are mainly fabricated using EBL and FIB techniques. EBL is capable of defining diversified patterns down to nanoscale dimensions in polymer resists. Therefore, it is normally combined with stripping (lift-off) or etching (dry etching and wet etching) to transfer patterns. For the lift-off method, it is cumbersome to make the fabrication process effective when the features go down to the tens of nanometers scale, especially for dense arrays, because resists are difficult to strip away. With wet etching techniques, it is hard to control the processes since etching rates are quite sensitive to chemical etchant concentration and other parameters like temperature and pressure.

Another common problem of wet chemical etching is rough sidewalls due to nonuniform etching rates. In contrast, dry etching can give much smoother sidewalls, improving etching profiles considerably. However, thin resist thickness and selectivity issues limit the dry etching process as well and make it only applicable to non-deep etching.

In this chapter, fabrication of nanorings and nanorods with two different techniques will be demonstrated. Both air- and metal-filled ring apertures are achieved. Patterns with good uniformity and high accuracy are shown. By FIB lithography, highly homogeneous nanoring arrays are demonstrated with less than 30-nm apertures in optically thick gold films. To obtain similar complementary patterns, EBL and ion milling are applied. In addition, fabrication of nanorod arrays is also shown using both the FIB method and EBL followed by ion milling. More

interestingly, dense nanorods with different lattices are fabricated using an improved FIB lithography patterning process with accurate geometry control; the patterns achieved here could find applications in nanofocusing and imaging.[55-57]

4.2 Plasmonic coaxial waveguides

As illustrated in Fig. 4-1, coaxial waveguides with different gap aperture widths were FIB-milled in an optically thick (450 nm) gold film which was deposited on a quartz substrate with a 10 nm titanium adhesion layer by electron-beam evaporation for 40 min (~ 0.2 nm/s average deposition rate) total evaporation time. Note that sputtering is another alternative film deposition method for noble metals. To minimize redeposition and charging effects, all patterns were milled in parallel instead of serially. Note the similarity of these coaxial structures to the LN counterparts described in the previous chapter. A probe current of 70 pA was applied with 30 kV acceleration voltage. One can clearly observe an increasing gap width from Figs. 4-1 (a) to (d), corresponding to 20 nm, 60 nm, 100 nm, and 140 nm (fixed inner radius R_i=200 nm and outer radii R_o=220 nm, 260 nm, 300 nm and 340 nm) with period Λ= 1200 nm. By design, it is feasible to obtain a wide range of metamaterials with such geometries in the visible range. Fig. 4-1 (e) shows similar ring arrays fabricated in a silver film for comparison. Serious redepositions can be observed, resulting in a rough sample surface. Fig. 4-1 (f) shows the cross sectional view of 35-nm gap width coaxial apertures. Strong contrast at the periphery of the rings is caused by redeposition during the milling process. We can also find slight damage at the ring periphery and larger gaps at the top portions due to long time milling.

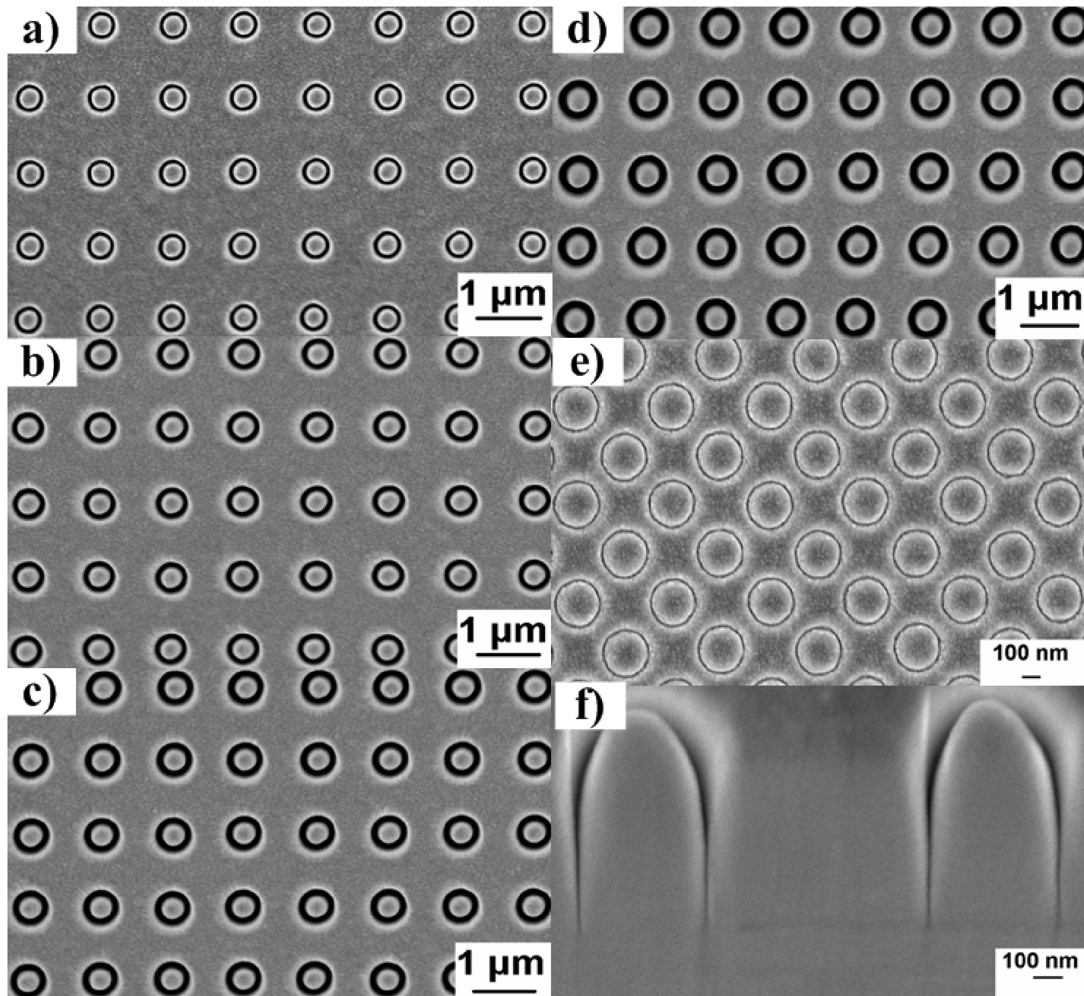

Fig. 4-1. SEM images of coaxial waveguides with different gap aperture widths in a 450-nm-thick gold film on a quartz substrate. (a) - (d), outer radii R_o equal to 220 nm, 260 nm, 300 nm and 340 nm with fixed inner radius R_i at 200 nm and pitch Λ= 1200 nm. (e) Similar nanoring structures fabricated in a 450-nm-thick silver film for comparison. (f) Cross sectional view of 15-nm gap width coaxial apertures. Note the difference of periodicity between (e) and (a)-(d).

Alternatively, complementary counterpart patterns of metallic coaxial apertures (instead of air gaps surrounded by metal) were fabricated by EBL followed by ion milling, as shown in Fig. 4-2. Negative electron resist NEB 22 was used for EBL pattern definition and an argon source was applied for ion milling (Microetch 1201 Ion Beam Etch System). The etch voltage and current were 300 V and 200 mA during ion milling, respectively. The measured etch rate was 23 nm for gold under a 30 sccm flowrate. The residual resists were stripped off by Microposit remover 1165.

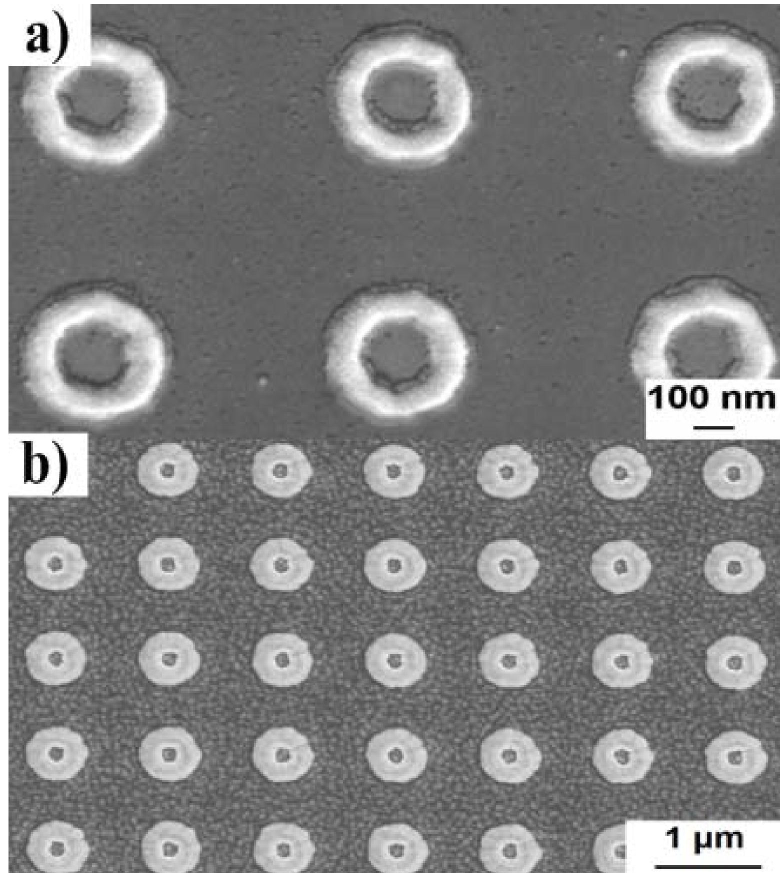

Fig. 4-2. Top view SEM images of metallic (110 nm thick gold) annular structures fabricated by EBL and ion milling with (a) 100 nm inner radius and 200 nm outer radius and (b) 60 nm inner radius and 280 nm outer radius.

Limited by etch rates and selectivity issues, 110 nm thick gold film with 5 nm titanium was employed here. In addition, to control the temperature in the chamber during milling, the milling process was run two rounds (3 min per run) with a 30 min intervening interval to cool down the system; otherwise the resist will be burned due to high resultant temperatures and cannot be removed by stripper thereafter.

4.3 Plasmonic nanorod arrays

Using an improved patterning method, it is feasible to fabricate dense nanorod arrays in a gold film. Fig. 4-3 is the schematic drawing of a pattern for nanorod fabrication using FIB lithography.

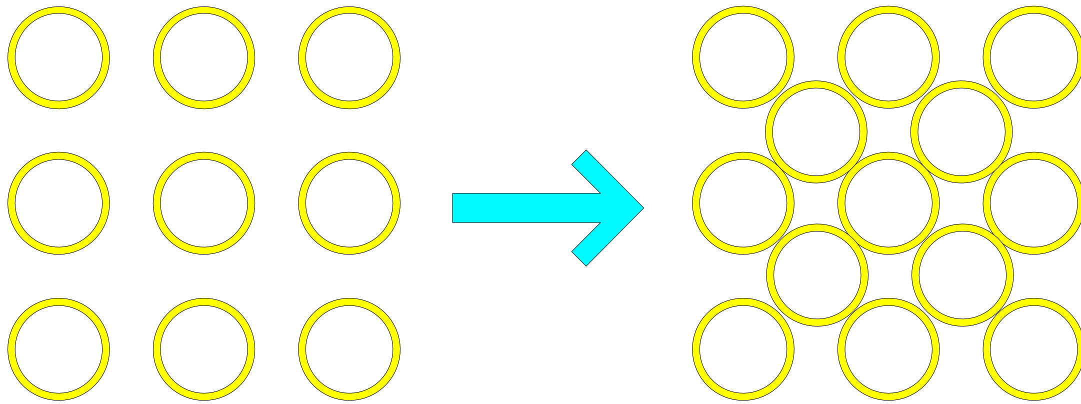

Fig. 4-3. Schematic diagram of the FIB lithography method for nanorod fabrication based on nanoring patterning.

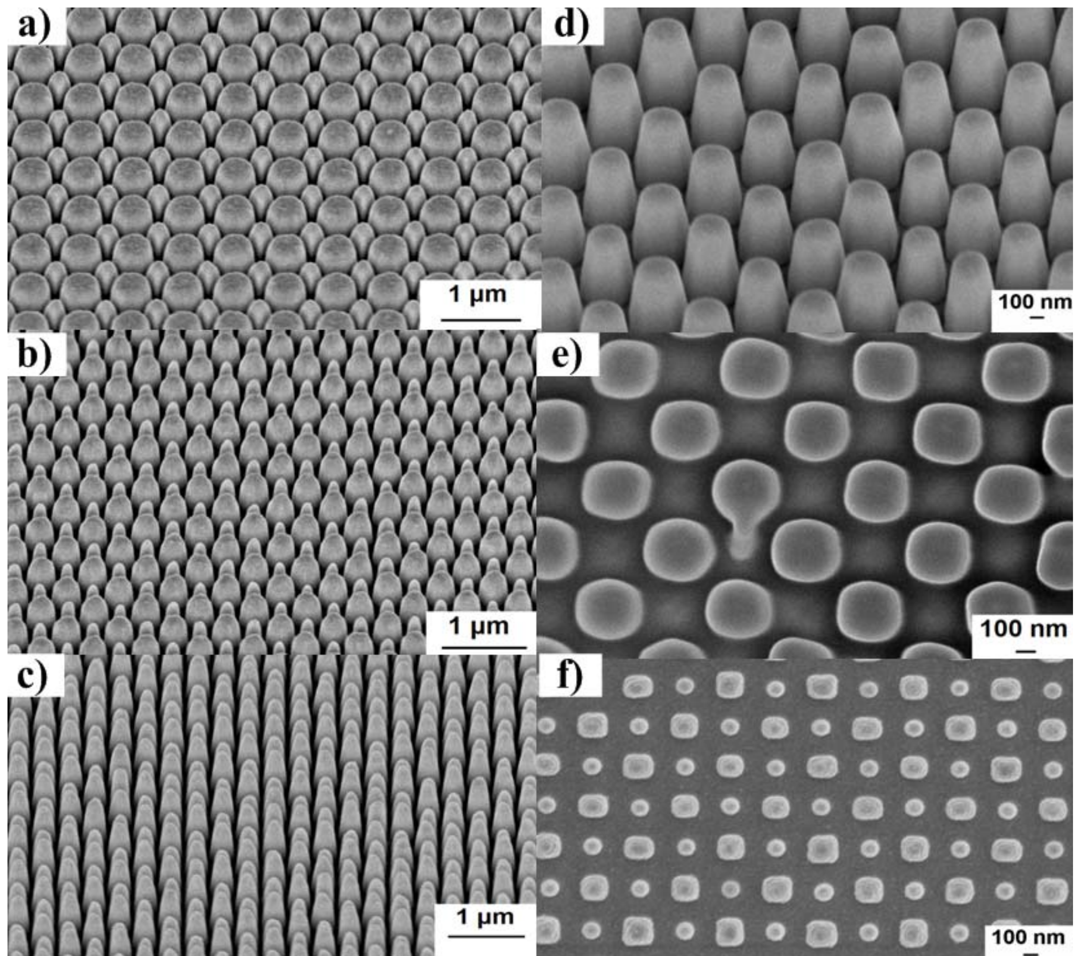

Fig. 4-4. SEM images showing dense nanorod arrays with varying lattice shapes fabricated in a 450-nm-thick gold film on a quartz substrate by FIB milling. Nanorods formed with (a) large difference in size, (b) moderate difference in size, and (c) equally-sized lattices. (d) shows the bottoms of the fabricated nanorods and one can clearly observe the angle of slightly tapered profiles of the fabricated rods. Top views of plasmonic crystals with (e) square lattices and (f) square-circle lattices.

By realigning coaxial ring-like structures, one can remove the parts between coaxial structures, leaving dense nanorod arrays with varying lattice shapes as illustrated in Fig. 4-4. Using such an improved FIB patterning method, one can simply fabricate metallic nanorods with larger aspect ratios than when using EBL techniques, since there is no limitation of selectivity issue. Moreover, one can easily control the geometry by varying inner and outer radii of individual rods and changing the distance between rods to precisely dominate overlapping areas. Therefore, the entire process is highly accurate and monolithic. Fig. 4-4 also demonstrates the programmable character of FIB lithography. From Fig. 4-4 (a), we can find lattices with different dimensions. By decreasing inner radii of the coaxial apertures, the discrepancy of the rods' sizes can be reduced as shown in Fig. 4-4 (b). To obtain isometric and homogeneous nanorod lattices, the inner radii are further decreased and Fig. 4-4 (c) illustrates nanorods with the same size and shape uniformity. Fig. 4-4 (d) clearly shows the bottoms of the fabricated nanorods and one can observe the angle of slightly tapered profiles of the fabricated rods. Figs. 4-4 (e) and (f) are top views of plasmonic crystals with differently shaped lattices. Since ions are significantly more massive than electrons and they can carry more momentum than electrons, they can strike a target with greater energy density at relatively short wavelengths to directly define patterns in hard materials. Therefore, the application of an electron-beam stays primarily in the realm of imaging while ions are expected to produce sharp and high resolution features under optimized conditions. One also needs to adjust many variables of the ion beam during a milling process to achieve a fine pattern.

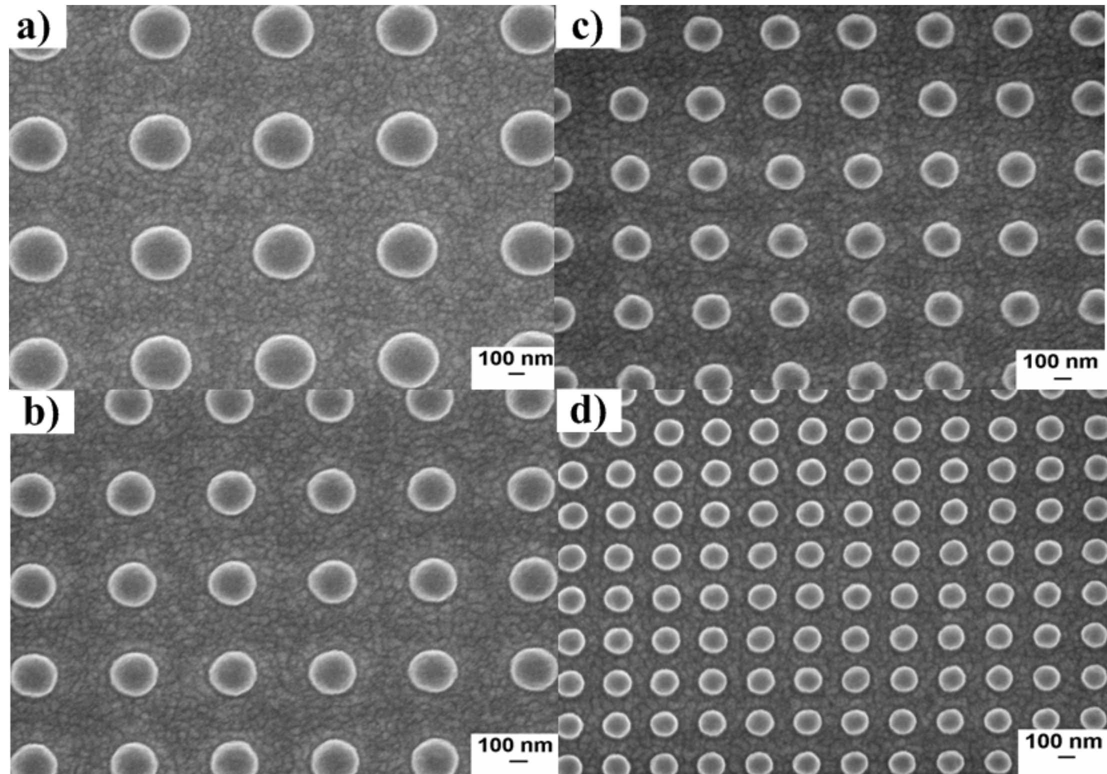

Fig. 4-5. SEM top views of plasmonic crystals fabricated using EBL and ion milling methods in a 110-nm-thick gold film with different periodicities of (a) 900 nm, (b) 700 nm, (c) 500 nm, and (d) 300 nm.

Using the same parameters as mentioned in Section 4.2, we also fabricated plasmonic nanorods using EBL and ion milling methods. As demonstrated in Fig. 4-5, nanorod arrays with different periodicities were fabricated. To measure the optical spectra of the fabricated nanorod arrays, a microspectrometer (CRAIC QDI 2010) was applied. Transmittance and reflectance measurements are normalized to the 75 W broadband xenon source and an aluminum mirror, respectively. As plotted in Fig. 4-6, one can see effective tuning of localized surface plasmon resonance (LSPR) using fabricated structures.

Resonances occur at different wavelengths when varying periodicities. The peaks in the transmittance and reflectance spectra gradually shift to longer wavelengths with increasing pitches, as shown in Fig. 4-6.

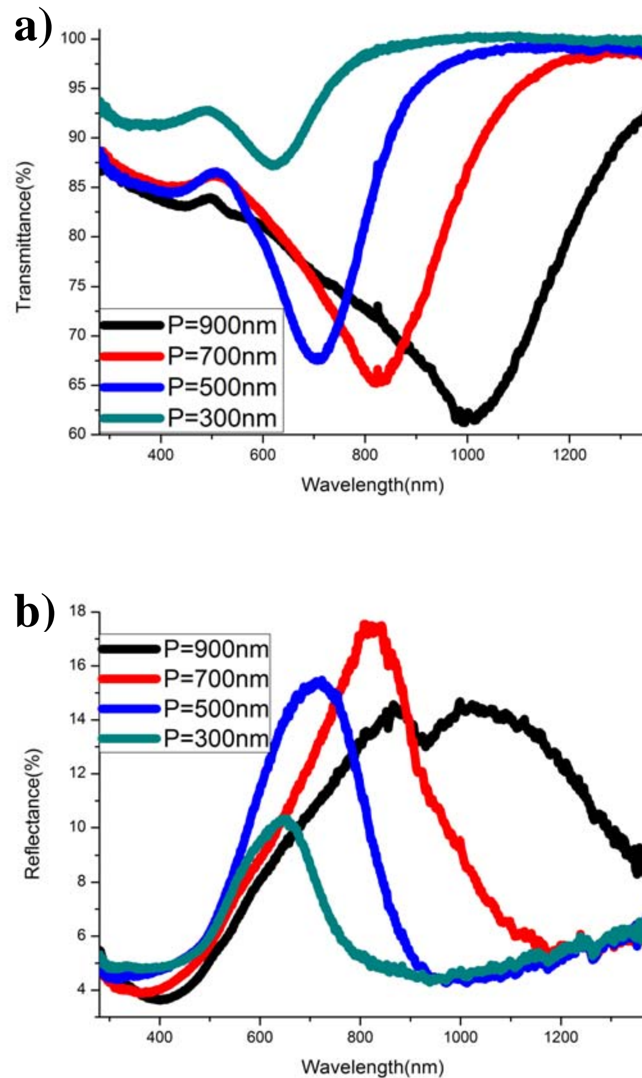

Fig. 4-6. (a) Transmittance and (b) reflectance spectra of the plasmonic crystals shown in Fig. 4-5.

4.4 Chapter summary

Fabrication of high quality plasmonic nanoring and nanorod structures using different techniques have been shown. Both air- and metal-filled coaxial geometries have been fabricated by FIB milling and EBL followed by argon ion milling. The uniform profiles of the narrow gaps have also been demonstrated using FIB cross sectional milling. Although the total milling depth and aspect ratio are limited by etching rates and selectivity issues using EBL, one can realize deep etching by using

an improved patterning with the FIB technique. By realigning ring arrays and controling the overlapping areas, one can fabricate dense nanorods with varying sizes, shapes and pitches. Effective LSPR tuning is achieved. Different geometries with various lattice shapes are thus available in a wide range of metallic materials now. The whole process is completely programmable and monolithic. Such geometries are crucial for fabricating plasmonic devices and can find extensive applications in focusing and imaging beyond the diffraction limit.

This chapter deals with main fabrication methods and demonstrates different structures with good quality and uniformity. Such devices could find a variety of applications (color filters, for instance) in nanophotonics, as will be discussed in the next two chapters.

Chapter-5: Annular Aperture Array Based Color Filter

This chapter experimentally demonstrates a color filter based on an annular aperture geometry working in the visible range. The device is built by configuring an array of annular apertures in a gold film suitable for transmission measurement. Effective tuning of resonance peaks through precise structural control of the aperture dimensions is shown. Selective transmission through annular apertures of various sizes leads to continuous color changing of transmitted electromagnetic waves. This may find potential for application in high-definition displays, optical filters, ultrafast switching and bio-sensing.

5.1 EOT through AAA

Annular aperture arrays (AAAs) have generated extensive interest in the last decade because of their potential as an important canditate for ultracompact optical devices, after the EOT properties of such geometries were first reported by Baida and coworkers.[58] Early investigations of guiding light of wavelengths much larger than the waveguide aperture dimensions using AAAs have shown several interesting phenomena and unique optical properties.[59-64] For example, the cutoff wavelength of a guided mode can be effectively shifted to longer wavelengths when the outer and inner radii are approaching each other.[60] Additionally, the low group velocity of the fundamental mode leads to important applications when materials with high electro-optic coefficients (LN, for instance) are employed in the AAA design.[65] Moreover, such annular structures can find application in composing single layer metamaterials in the visible range.[45,46,66]

Very high (up to 90%) transmission through AAAs has been previously achieved at visible frequencies (using AAAs fabricated in a silver film[47]) and this property, combined with the fact that the optical response of AAAs is also insensitive

to the incident angle,[67,68] makes the AAA structure a perfect candidate for high efficiency display and filtering devices.

In this chapter, a simple yet effective method is proposed to filter individual colors using AAA-based geometries. Fabrication of apertures with features as small as 25 nm that show efficient color-filter functionality is demonstrated. An effective wavelength selecting function with AAAs that can be operated across the whole visible band and tuning of transmission resonance via structural control are also demonstrated. The optical response of the fabricated devices can be accurately tailored by shaping the aperture gap width, leading to new opportunities for nanophotonics and optics.

A 2-D AAA structure usually has at least two transmission peaks, as reported by different groups under different designs.[58-64] The transmission peaks are caused by cylindrical surface plasmons (CSPs) and planar surface plasmons (PSPs), respectively. CSPs are affected by the geometrical design and the thickness of the metal film, while PSPs are mainly related to the periods of two dimensional gratings fabricated therein. Baida *et al.* have further studied the double peak transmission analytically and provided a relation between geometrical parameters and position of the peaks, which has been implemented in Ref. 62 to design different structures with the same resonance peaks. The resonance peaks are a direct result of Fabry-Pérot resonances in a cylindrical resonance cavity formed by a metal film with finite thickness and two end-faces. For a finite metal film with thickness l, the design of the desired transmission peaks can be estimated by the following equation[62]

$$l = \frac{m\pi + \varphi}{\beta} \quad \text{..............................} \quad (5.1)$$

where l is the thickness of the metal film, m is the order of the Fabry-Pérot resonance, and φ and β represent phase of reflection and propagation constant, respectively. For the case where l is constant, the propagation constant β varies with different annular aperture sizes, and affects the reflection and transmission of the designed structure. Detailed discussion and analytical solutions of φ and β can be found elsewhere.[62]

In this work, the target is to design a color filter which allows the transmission of a selected wavelength in the visible range for applications of true color or high-definition displays. Therefore, a metal film with fixed thickness (160 nm gold in this study) is preferred. The periods of the two dimensional gratings also play an important role affecting the selective transmission. PSP resonances occur for wavelength values given by[58]

$$\lambda = \frac{p_x p_y}{\sqrt{i^2 p_y^2 + j^2 p_x^2}} \sqrt{\frac{\varepsilon_m \varepsilon_d}{\varepsilon_m + \varepsilon_d}} \quad \text{..............................} \quad (5.2)$$

where p_x and p_y are periods of annular apertures along the x and y directions, respectively, ε_m and ε_d represent the permittivities of metal and dielectric, and i and j are integers. The position of the transmission peaks caused by PSPs is determined by the periods of the two dimensional gratings. Thus, it can be artificially tuned by changing the periods of the gratings. However, multiple transmission peaks within the visible range will degrade the performance of the color selector. This effect can be minimized by increasing the periods of the two-dimensional gratings so that the resonance peaks can be moved out of the visible range.

5.2 Tunable resonance via geometric control

Fig. 5-1 shows the schematic representation of the fabricated elements and measurement system in this work. Using electron-beam evaporation, a 160 nm thick gold film over a 6 nm titanium adhesion layer was first deposited on a quartz substrate. Then arrays of coaxial rings were milled using FIB etching. Each array comprises 9×9 rings occupying an area of ～10×10 μm^2. The inner radii of the coaxial rings are fixed to 200 nm while the outer radii change from 225 nm to 270 nm in steps of 15 nm (corresponding to a 25-70 nm gap width). Measurements of the transmission properties of the fabricated nanostructures were carried out using a UV-Vis-NIR microspectrometer (CRAIC QDI 2010) at normal incidence.

Figs. 5-2 (a) and (b) show SEM images of a fabricated AAA, and a single aperture (gap width equal to 25 nm) with a much higher magnification, respectively. Fig. 5-2 (c) plots the measured transmission spectra of the coaxial structures with gap widths of 25, 40, 55 and 70 nm. The apertures have fixed inner radius at 200 nm and varying outer radii from 225 nm to 270 nm in steps of 15 nm. One can see that when the gap width is 70 nm, a broad resonance can be observed which is centered at ～590 nm. After the gap is narrowed to 55 nm, the transmission peak shifts to around 650 nm. Further reducing the gap width to 40 and 25 nm, additional red shifts can be observed and new resonance peaks are located at ～680 nm and 710 nm because of the excitation of CSP modes on the metal-dielectric interfaces and strong coupling of CSP modes on the inner and outer surfaces of the rings. And this coupling enhances prominently as the inner and outer radii progressively approach each other.

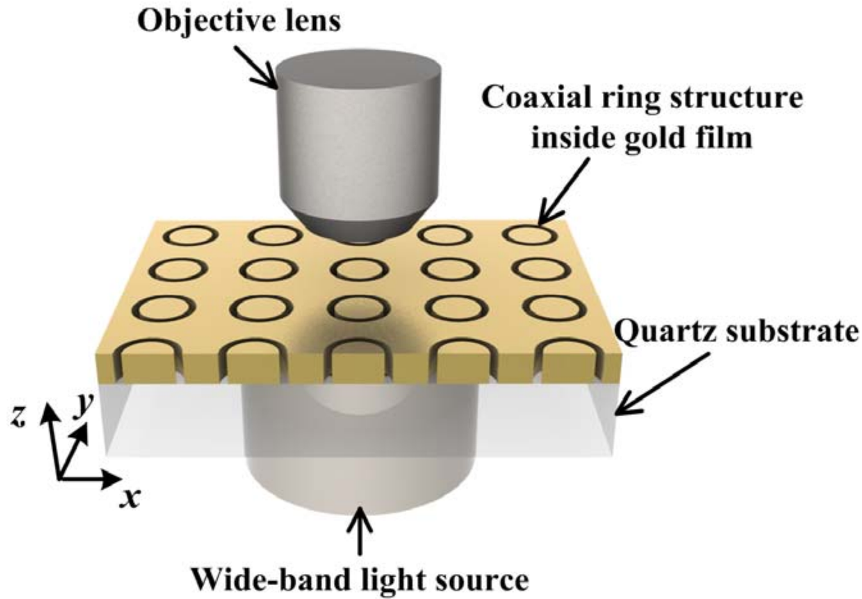

Fig. 5-1. Schematic drawing of the proposed color filter working under transmission measurement.

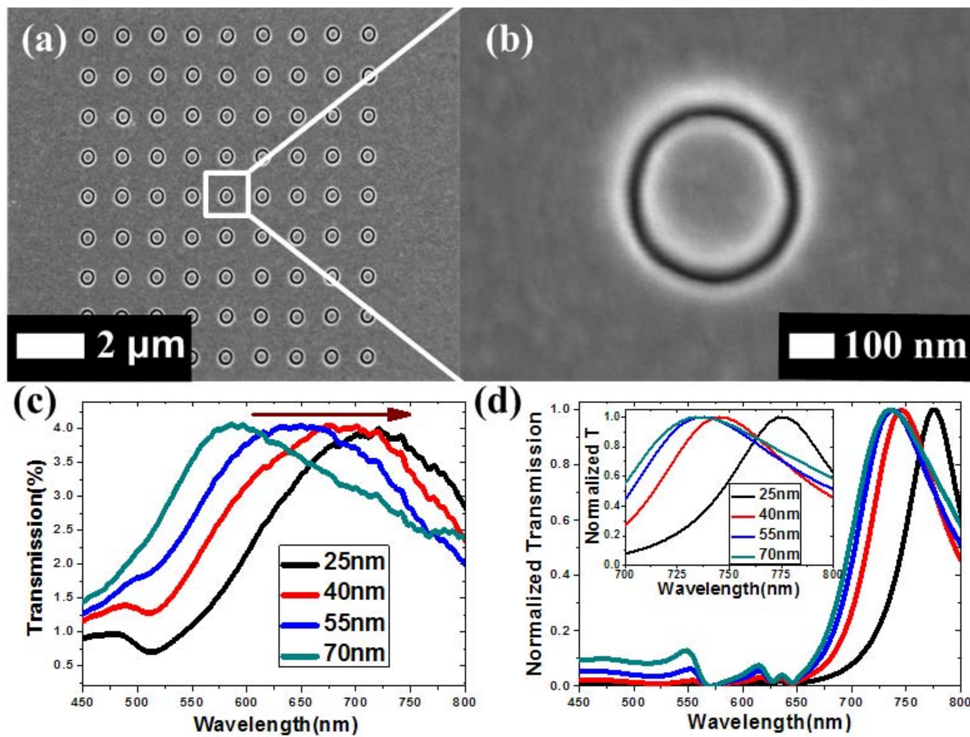

Fig. 5-2. SEM images showing (a) overview of a fabricated 9 × 9 AAA and (b) magnified view of a single ring with 25 nm gap width. (c) Measured and (d) simulated transmission spectra of AAAs as a function of gap width. Simulated spectra are normalized for clarity. The apertures have fixed inner radius at 200 nm and varying outer radii from 225 nm to 270 nm in steps of 15 nm. The arrow in (c) indicates decreasing gap width. Inset of (d), magnified peak tops with 700-800 nm wavelength range to show the shift more clearly.

Note that the tuning of transmission peaks was realized via controlling the gap width of the ring apertures instead of the periodicity (fixed to 1200 nm) of the arrays. The transmission characteristics are mainly determined by the CSP modes inside each gap cavity rather than by the periodicity. To further investigate the underlying physical principles related to the annular apertures, finite-difference time-domain (FDTD) simulations[69] were performed by a collaborator (Zhao Yanhui, Ph. D candidate at Pennsylvania State University) to investigate the theoretical performance of the structures. The dispersion model of gold was based on the Johnson and Christy model[70] in the material library of the software. The simulation model was built based on the schematic shown in Fig. 5-1.

The dimension of the simulation area was 2.4 μm × 2.4 μm × 1μm, which allowed two periods of the ring structure in the x-y plane, and enough space for the light source and power monitors. Periodic boundary conditions were applied for the x and y directions and perfectly matched layer boundary conditions were used for the z direction. A polarized Gaussian beam was used as the light source with the polarization direction along the x axis. The source covered wavelengths ranging from 400 nm to 900 nm, with an increasing step of 2 nm. A power monitor was located 300 nm above the gold film to collect any transmission modes reaching the output region.

The calculated transmission spectra are shown in Fig. 5-2 (d). The position of the resonance peaks strongly depends on the diameter values and similar results have been observed and discussed in Refs. 51 and 52. A redshift of the resonance peaks can also be observed when decreasing the gap width. Note that the simulated transmission

curves here are normalized to clearly show the shift trend of the transmission peaks. Compared to the measured spectra, the slightly smaller spectral width and red shift (~ 150 nm) of the peak wavelength λ_{max} observed in the simulations are mainly due to the difference between the idealized features used in the simulations and imperfect structures of fabricated elements for testing, e.g. rough surfaces and tapered sidewalls caused by redeposition during FIB milling. It is also attributed to the convergence of numerical iteration process in the software. Besides, the periodical boundary conditions applied onto the simulation differ from limited testing sample area allowed by the field of view of the measuring instrument, as discussed in Ref. 47. A 9 × 9 array of rings was measured in reality, but simulations were based on bi-infinite AAAs along both x and y directions. Nevertheless, the overall trends in both peak position and red shift of λ_{max} with decreasing gap width agree well with the measured spectra, clearly demonstrating the dependence of resonance on the gap width of the apertures.

The calculated electric field distributions are presented in Fig. 5-3. Auto-nonuniform meshing with the finest meshes (0.25 nm minimum mesh step, corresponding to 4.8146×10^{-19} s maximum time step) was used in the x-y plane as illustrated in Fig. 5-1 to get the most accurate results. Strong confinement of light in the nanoring cavity is obvious, corresponding to the TE_{11} mode demonstrated in previous work.[48,61] Top and cross-sectional views of the 55 nm ring at 740 nm (λ_{max}, on-resonance) and 600 nm (λ_{min}, off-resonance) confirm that the selective transmission is caused by the resonant ring cavities with various gaps.

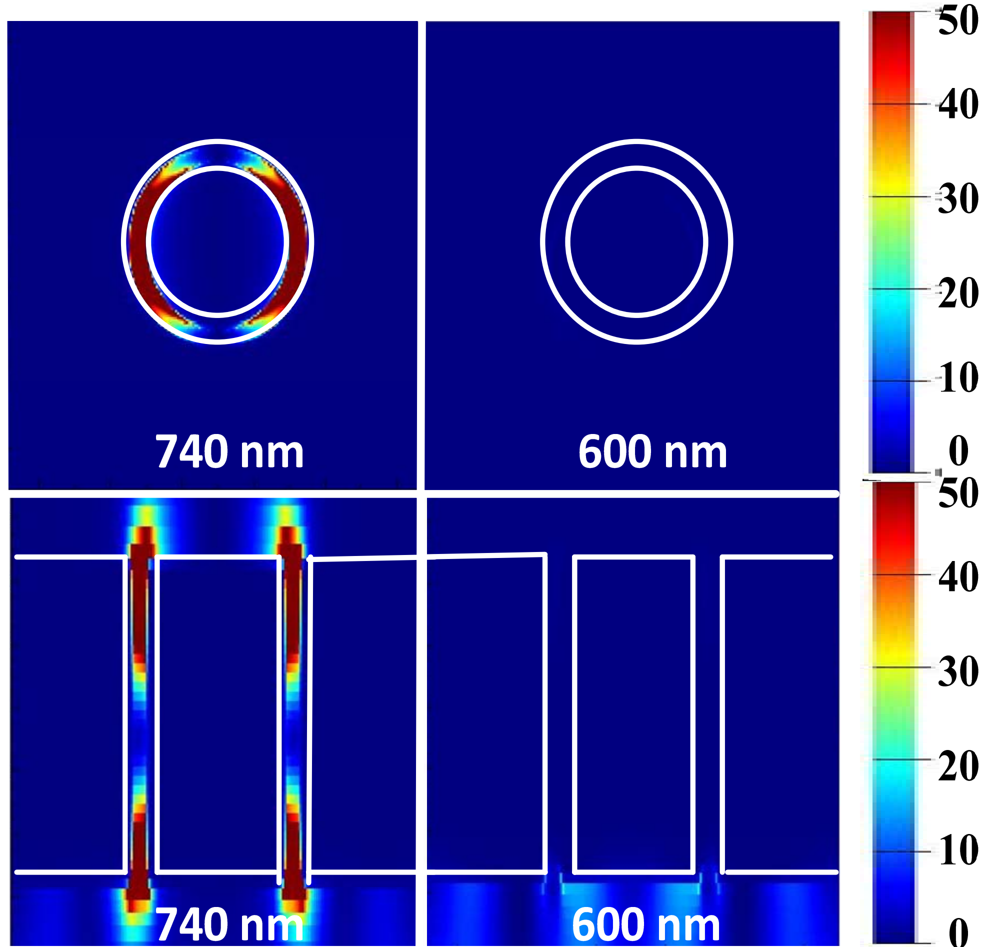

Fig. 5-3. Top panel: top view; and bottom panel: cross sectional view showing the electric intensity distribution of a single ring with 55 nm gap width illuminated at 740 nm (λ_{max}) and 600 nm (λ_{min}).

5.3 Fabrication and characterization of AAA color filter

In order to further tune the transmission response and finally filter individual colors out, new AAAs with 40 nm increments were milled in another sample with significantly increased gap widths. SEM images of the fabricated structures are shown in Figs. 5-4 (a) - (d). One can see that the fabricated ring patterns are uniform. The white spots at ring surroundings are caused by redeposition during FIB milling. Using 40-, 80-, 120-, and 160-nm-wide ring apertures, colors of red, yellow, blue and cyan, respectively, can be observed in Fig. 5-4 (e).

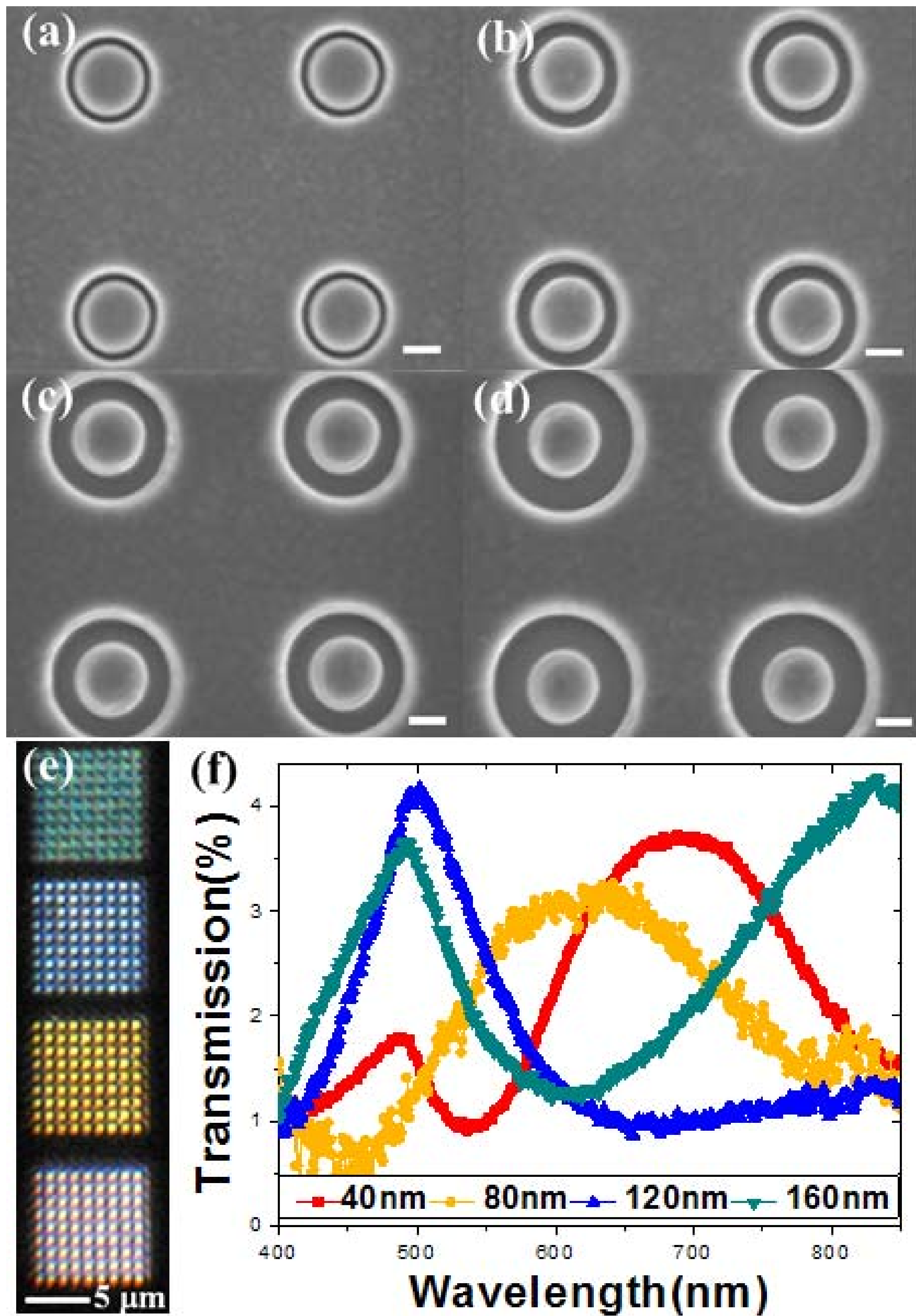

Fig. 5-4. SEM images of the fabricated AAAs with (a) 40 nm, (b) 80 nm, (c) 120 nm, and (d) 160 nm gap width (outer radii equal to 240 nm, 280 nm, 320 nm, and 360 nm with 200 nm fixed inner radius). Scale bars are 200 nm. (e) Corresponding optical image presenting different colors. (f) Measured transmission spectra of the AAAs with different color outputs shown in (e).

Fig. 5-5. Optical images showing the words of (a) “NUS” and (b) “IMRE” with different colors.

As plotted in Fig. 5-4 (f), resonances occur at different wavelengths when varying the gap widths; peaks gradually shift to longer wavelengths as the rings are narrowed. The relatively weak intensity is mainly caused by high loss and attenuation over a long propagation distance (160 nm gold with 6 nm titanium in this work). For arrays with 160 nm and 120 nm gaps, the transmission peaks are located at about 480 nm and 500 nm, giving cyan and blue colors, respectively. When the gap aperture is narrowed down to 80 nm, the peak shifts to ～600 nm, exhibiting a yellow color. More light at around 680 nm is transmitted when the gap is further narrowed to only 40 nm, which results in a red color. A similar trend has been observed in Fig. 5-2: a blue shift of the transmission peaks occurs with increasing sizes of the annular

aperture. Fig. 5-5 shows the words of “NUS” and “IMRE” using nanorings with different gap widths to present varying colors.

5.4 Chapter summary

In summary, tuning of the transmission resonance at visible frequencies has been demonstrated with AAAs in a metallic film. The optical response of a broadband light source through nanorings is wavelength-selective and accurate control can be achieved to filter individual colors out. FDTD calculations confirm the resonance dependence of selective transmission on gap width. Using AAAs, fine tuning of optical response through structural control and a color filtering function under transmission mode can be readily realized, opening up new opportunities for sensing and integrated optics.

Annular nanorings can be used as filters to distinguish individual colors as shown in this chapter. Alternatively, plasmonic nanorods are capable of filtering colors under reflection testing mode, which will be demonstrated experimentally in the following chapter.

Chapter-6: Plasmonic Crystal Color Filter Based on Silver Nanorods with Ultrasmall Spacings

In this chapter, a novel method will be developed for filtering broadband light into individual colors under reflection measurement using 2-D plasmonic nanorods with ultrasmall inter-rod spacings. Fine tuning of LSPR with varying array periodicities will be shown. The dependence of reflected intensity on inter-rod spacing will be first determined and then utilized to develop a plasmonic crystal color filter using dense silver nanorods with different periodicities. Theoretical calculations agree well with experimental results. This approach may find broad application in sensing and filtering.

6.1 Coupling regimes in plasmonic nanorods

The use of noble metals allows coupling of incident light to fabricated nanostructures, resulting in collective electron oscillations localized in the metallic nanostructure, which are LSPRs. Importantly, the excitation of LSPRs gives rise to greatly enhanced electromagnetic fields and strong near-field coupling with different designs,[71-90] enabling highly sensitive sensing[91-95] with large quality factor and figure of merit. Due to the high sensitivity and reliability of the interaction between plasmonic nanorods and incident electromagnetic waves, many achievements[96-99] have been realized.

Based on the shift of the LSPR wavelength, high performance sensing of refractive index is available in a wide range of applications. The optical response of the LSPR depends strongly on the particle size, shape, composition and dielectric environment, leading to extensive tuning applications via flexible structural control. In particular, the optical response of metallic particles can be tailored for operation at different frequency bands, offering great opportunities for various photonic designs at nanometer scales.

The tunability of the LSPR with high performance and sensitivity is therefore of special importance. Additionally, the interaction between electromagnetic waves and metal nanoparticles allows for tight confinement of light and guiding beyond diffraction limit. Investigations of the coupling interactions between metal nanoparticles of periodic structures are critical to understand the energy transfer and resonance properties. Coupling between metallic nanorods leads to a significantly enhanced electric field when the rods are close enough to excite the interaction between different plasmon modes. Resonances depend strongly on the separation between nanorods and the strength of their individual interaction with the incident wave. However, most of the resonances which have been experimentally demonstrated by using periodic plasmonic crystals are in the near infrared range.[96,97]

This chapter shows reflection resonances generated at visible frequencies using dense plasmonic periodic nanorod arrays with ultrasmall inter-rod spacings to introduce strong near-field coupling effects and fine tuning of plasmon resonance across the whole visible band via geometrical control. Typically, there are two different coupling regimes based on the inter-rod separation, namely weakly and strongly coupled regimes.[100-104] For relatively large separations, far-field dipolar interactions are dominant. When the separations are remarkably reduced, strong near-field coupling is enabled between neighboring nanorods involving the sharply evanescent fields tightly confined to the rod tops. With these two coupling regimes in mind, we present the coupling effects in two dimensional metallic nanorod arrays. The effects of different periods of rod arrays on the plasmonic resonance under the

relation of $d/p = 0.5$ are examined firstly, with d representing the diameter of the rod and p being the periodicity of the two dimensional array. In the second step, plasmonic resonances of fabricated nanorod arrays in strongly coupled regime are investigated by changing to different ratios of d/p. Finally, a plasmonic crystal color filter using silver nanorods is developed with ultrasmall spacing (s) based on the conclusion drawn from those studies. By decreasing the inter-rod separation and precisely controlling the periodicity, plasmonic crystal arrays are capable of tuning the plasmon resonance and filtering individual colors. These results may find extensive application in high resolution displays, biological and chemical sensing and efficient surface enhanced Raman spectroscopy substrates.

6.2 Nanorod color filter based on strong coupling effect

Fig. 6-1 shows the schematic diagram of the design and measurement system in this study. Silver nanorods were fabricated on a quartz substrate using standard EBL followed by ion milling. Fig. 6-2 (a) shows a typical example of the fabricated two dimensional gratings on a quartz substrate with $p = 550$ nm and $d = 275$ nm ($d/p = 0.5$). As plotted in Fig. 6-2 (b), tuning of the LSPR using nanorod arrays with normal inter-rod spacing ($s > 200$ nm) and varying periodicities ranging from 400 nm to 700 nm in 50 nm increments is demonstrated. As can be seen, accurate and fine tuning of the LSPR can be realized across the near infrared range with various array periodicities. Shift of resonance peaks from 730 nm to 1280 nm is obtained when the periodicity is increased. It is obvious that the resonance peaks red shift with increasing periodicities and the reflected intensity remains almost constant.

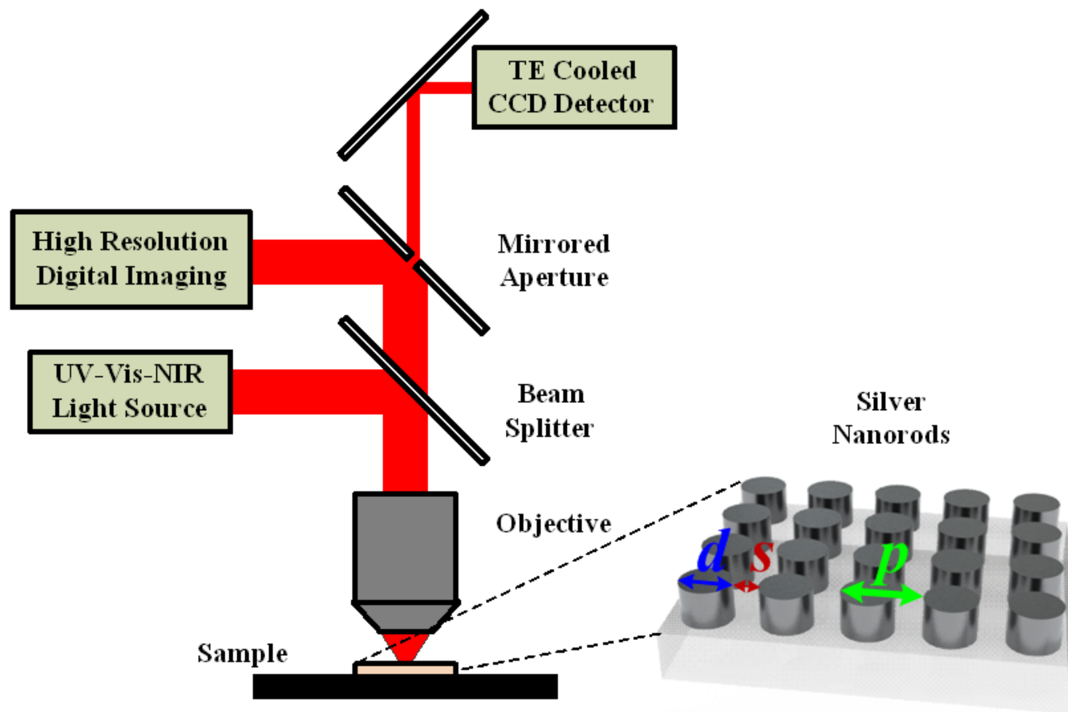

Fig. 6-1. Schematic of the proposed color filter working under reflection mode.

When the periodicities are 700 nm and 650 nm, broad resonance peaks can be observed at 1270 nm and 1180 nm from the reflection spectrum. In addition, the full-width at half-maximum (FWHM) increases noticeably with larger periodicities, indicating shorter lifetimes. In addition, the main resonances are sharpened and enhanced when the period is reduced due to stronger coupling in the cavities which results in higher reflected intensity and quality factors. Besides, the shift of resonance peaks (λ_{max}) maintains almost a linear change with the increment of periodicity, with an unoptimized changing range up to 90 nm, as shown in Fig. 6-3. This feature is assigned to the linear regressions of periodical rod arrays which can be verified by coupled dipole approximation or discrete dipole approximation calculations. Fig. 6-2 (c) plots the calculated reflections corresponding to the measurements shown in Fig.

6-2 (b) using Lumerical FDTD solutions[69] by a collaborator (Zhao Yanhui, Ph. D candidate at Pennsylvania State University). Good agreement of red shift with increasing periodicity between experimental and theoretical results can be observed. Note that the measured spectra are not as intense and sharp as the simulated ones because of fabrication imperfections including tapered sidewalls and rough surfaces. The homogeneous broadening and ununiformity are attributed to larger losses in measurements caused by grain boundaries and surface scattering. Differences of peak positions and FWHM between measured and calculated data are caused by the shape discrepancy between the simulation models (ideal cylinder rod) and real samples (dome-like shape). The observed two reflection minimums in Figs. 6-2 (b) and (c) can be accounted for the Wood's anomalies, or the Rayleigh cutoff wavelength for a periodical nanoparticle array structure. The nanoparticle array works as a buffer layer between two different materials: air and quartz substrate. The dispersion relations of the incident electromagnetic waves with same frequencies are different due to different refractive indices. Diffraction happens on both interfaces of the air/particle array and the substrate/particle array, and many modes tend to transmit from the air into the substrate. However, total conversion of all the diffraction modes from one medium to another is impossible due to impedance mismatch, or different dispersion relations of the electromagnetic waves inside different materials, thus some diffraction modes will disappear during the conversion process and are confined on the interface in the form of surface waves. Those missing diffraction modes are represented as narrow reflection minimums in the reflection spectrum.

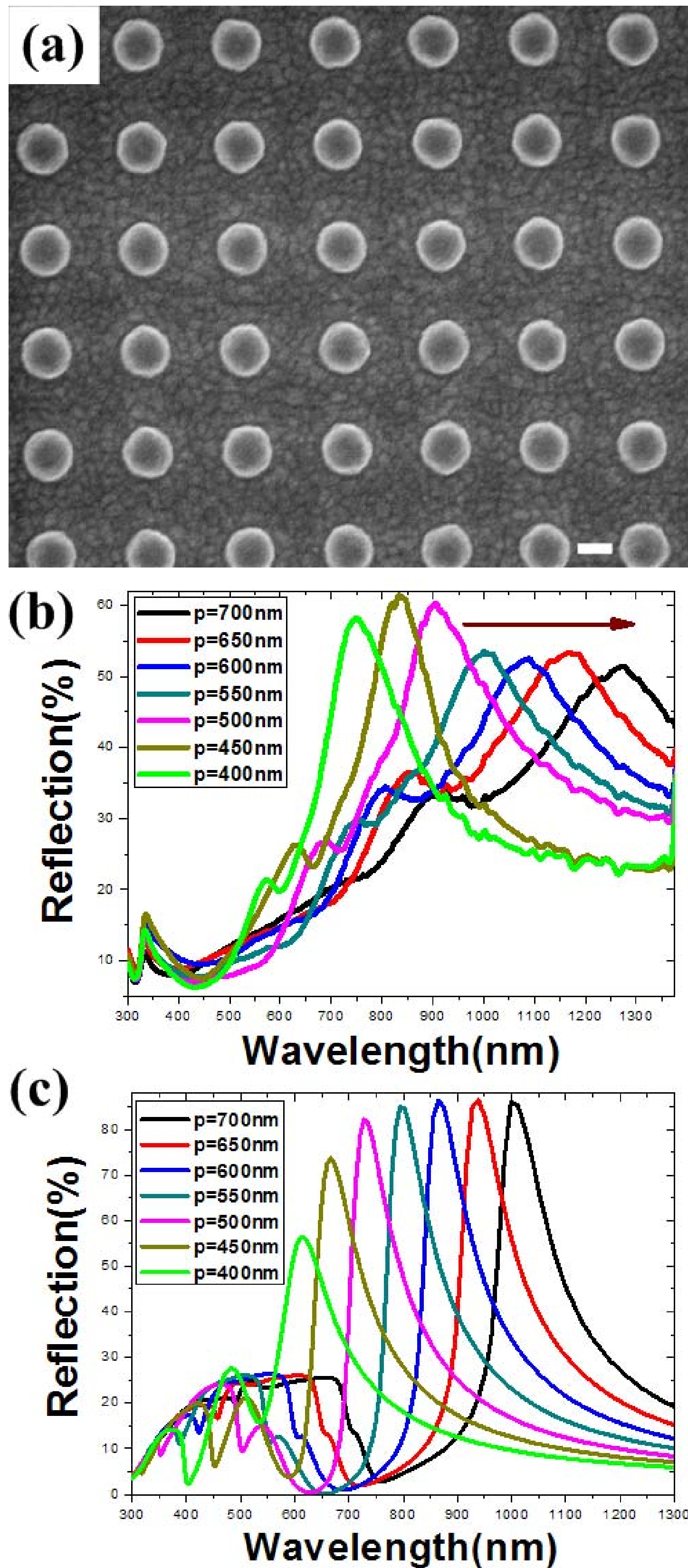

Fig. 6-2. (a) SEM image showing the top view of the nanorod array with period p =550 nm. Scale bar, 200 nm. (b) Measured and (c) calculated reflection spectra of nanorod arrays with periodicities from 400 nm to 700 nm. The arrow indicates increasing periodicities. The height of the nanorods is 240 nm.

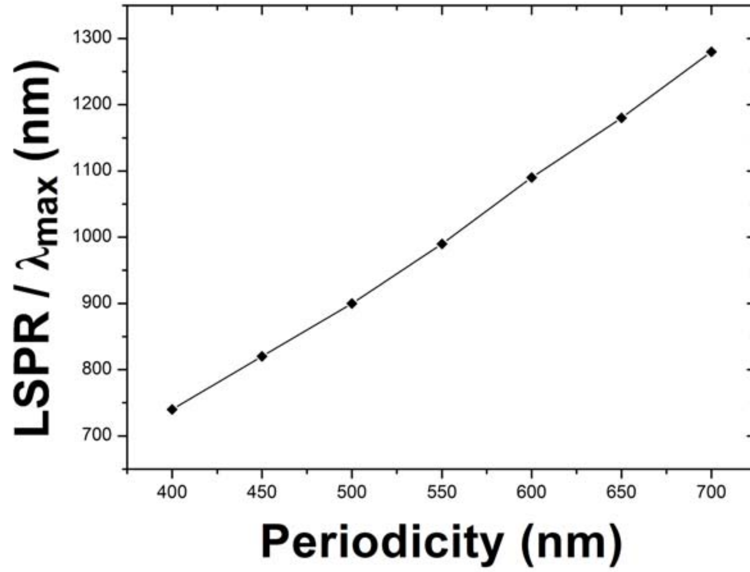

Fig. 6-3. Dependence of the reflection resonant wavelength on the periodicity. As the periodicity is varied, the resonance (λ_{max}) sweeps with a typical constant increment (about 90 nm).

The Rayleigh cutoff wavelength at an interface of two different materials can be expressed as follows: [99]

$$\lambda_{R_lmn} = \frac{p}{l}\left\{\sqrt{m^2+n^2} \pm \sin(\theta)\left[m\cos(\varphi)+n\sin(\varphi)\right]\right\} \quad (6.1)$$

where λ_{R_lmn} is the cutoff wavelength, p is the lattice constant of the particle array, θ is the incident angle and φ is the polarization angle. l, m, n are all integers. For the case of normal incidence and $\varphi = 0$, the most important cutoff wavelengths for our case at two different interfaces can be estimated as: [99]

$$\lambda_{R_l}^{air} = \frac{p \cdot n_{air}}{l} \quad \text{and} \quad \lambda_{R_l}^{quartz} = \frac{p \cdot n_{quartz}}{l} \quad (6.2)$$

For a nanoparticle array with period of 400 nm, we can expect two cutoff wavelengths with a transmission peak between them from the spectrum at two different locations, one is around 400 nm, and the other wavelength is around 550 nm, corresponding to the dips observed at 420 nm and 580 nm in the measured reflection spectra.

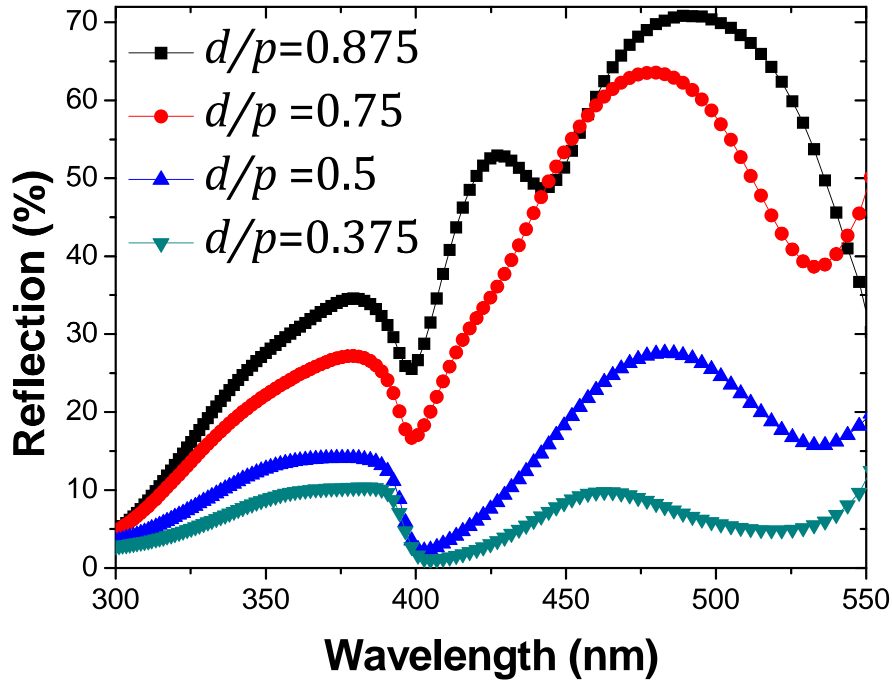

Fig. 6-4. Simulated reflection of nanorod arrays with constant periodicity *p* = 400 nm and varying *d/p* ratios.

To extend the investigation to the strong coupling regime and design the color selector device, the case that *d/p* with various values rather than a fixed constant should be discussed to get a clear concept of how *d/p* will affect our design. In Fig. 6-4 (a), calculated reflected intensity of nanorod arrays with constant periodicity *p* = 400 nm and varying *d/p* ratios are plotted.

There are two important points that need to be noted here. First, the peak position barely changes with different *d/p* values, which is a confirmation that the position of the reflection peak can be estimated using Eqs. (1) and (2) even in the case where *d/p*=0.5. Second, the reflected intensity increases dramatically with reduced inter-rod spacings, given that limited transmission can pass through the compressed space among the nanorods, leading to a high efficiency in the reflection measurement.

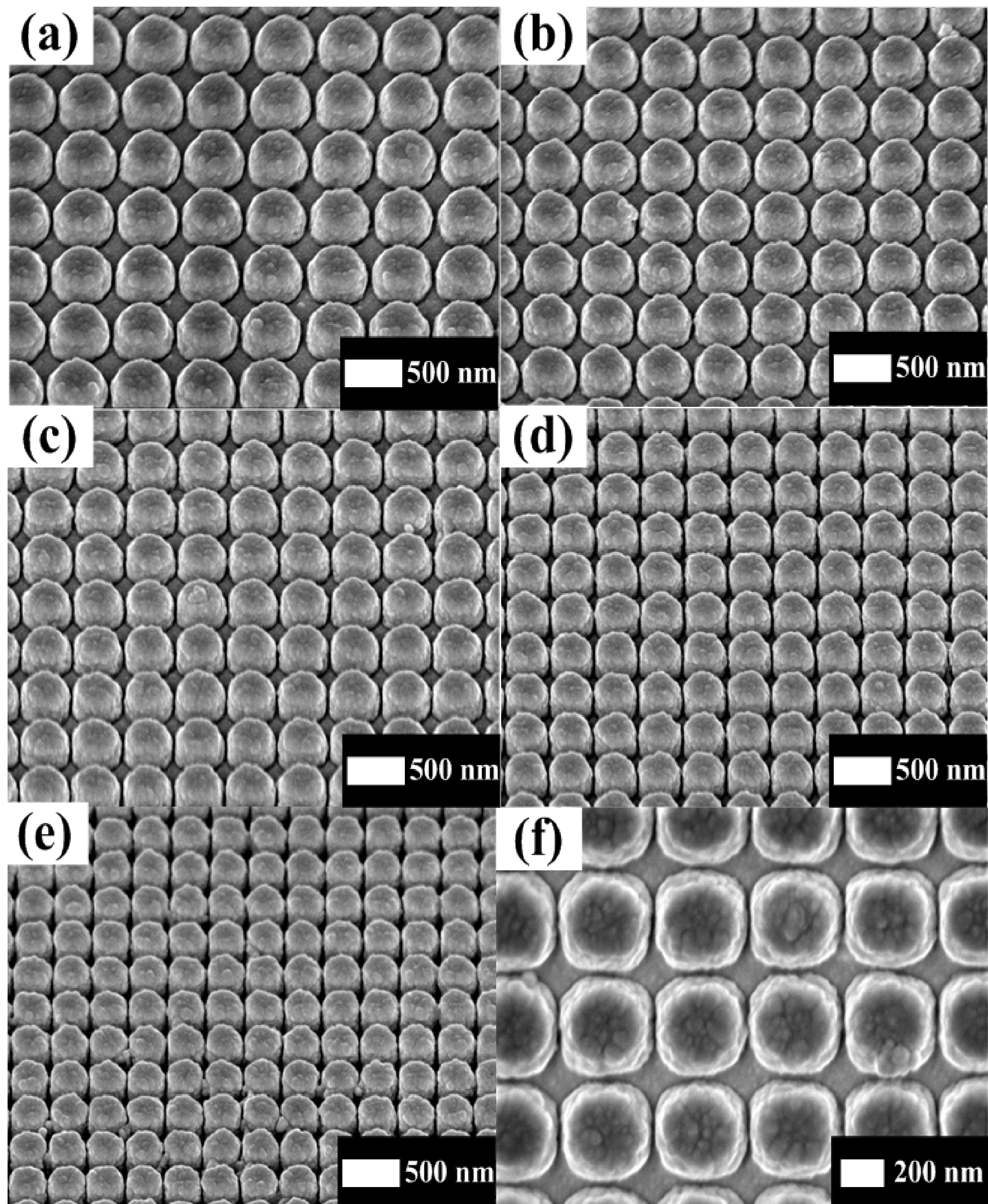

Fig. 6-5. SEM images of nanorods with ultrasmall gaps. (a) - (e) Oblique views of nanorod arrays with varying periodicities from 540 nm (a) to 320 nm (e) in steps of 55 nm. (f) Magnified top view of the p = 375 nm rod array (blue color). It is obvious that the rods have been milled through. The height of the nanorods is 240 nm.

As a result, the transmitted intensity is relatively low (see Fig. 6-6 (c) for details) in the visible range, leading to a high efficiency color filter working under the refection testing mode.

Table 6-1. Parameters of the arrays presenting different colors.

Presented color	*Periodicity (nm)*	*Diameter (nm)*	*Spacing (nm)*	*d/p*
Red	540	500	40	0.926
Yellow	485	450	35	0.928
Green	430	400	30	0.930
Blue	375	350	25	0.933
Cyan	320	300	20	0.938

In order to generate considerable optical response in the visible band, we now introduce strong coupling between adjacent nanorods by dramatically decreasing inter-rod separations. Typical SEM images of nanorods with ultrasmall spacings are displayed in Fig. 6-5. Obviously, the nanorods have been milled through and very small (20 - 40 nm) inter-rod spacings can be observed.

Using nanorods with varying periodicities from 540 nm (Fig. 6-5 (a)) to 320 nm (Fig. 6-5 (e)) in steps of 55 nm, we filtered individual colors out as shown in Fig. 6-6 (a). The structural parameters of the arrays are summarized in Table I. As expected, strong optical excitations in the visible band of the spectrum are observed. Nanorods with ultrasmall gaps exhibit similar reflection resonances and peak shift observed from rod arrays with regular separations shown in Fig. 6-2.

By changing the periodicity of the nanorod arrays, tuning of the LSPR peak wavelengths between 480 nm (cyan) to 630 nm (red) is achieved, as shown in Fig. 6-6. Sharp spectral features with a significantly reduced linewidth can be observed with decreasing periodicities.

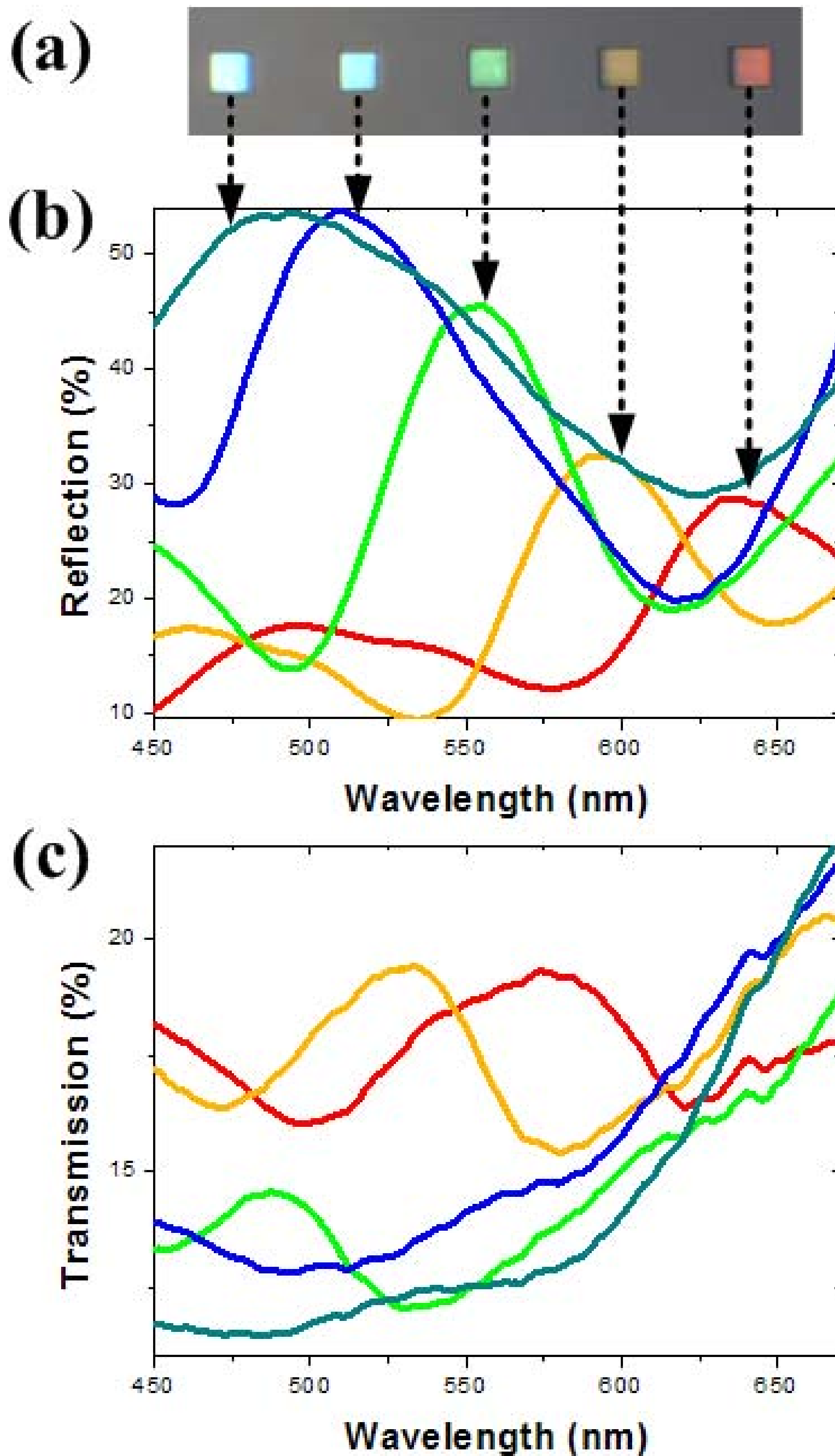

Fig. 6-6. (a) Optical image showing different color outputs under reflection mode using plasmonic nanorod crystals. Measured corresponding reflection (b) and transmission (c) spectra of the arrays as a function of wavelength.

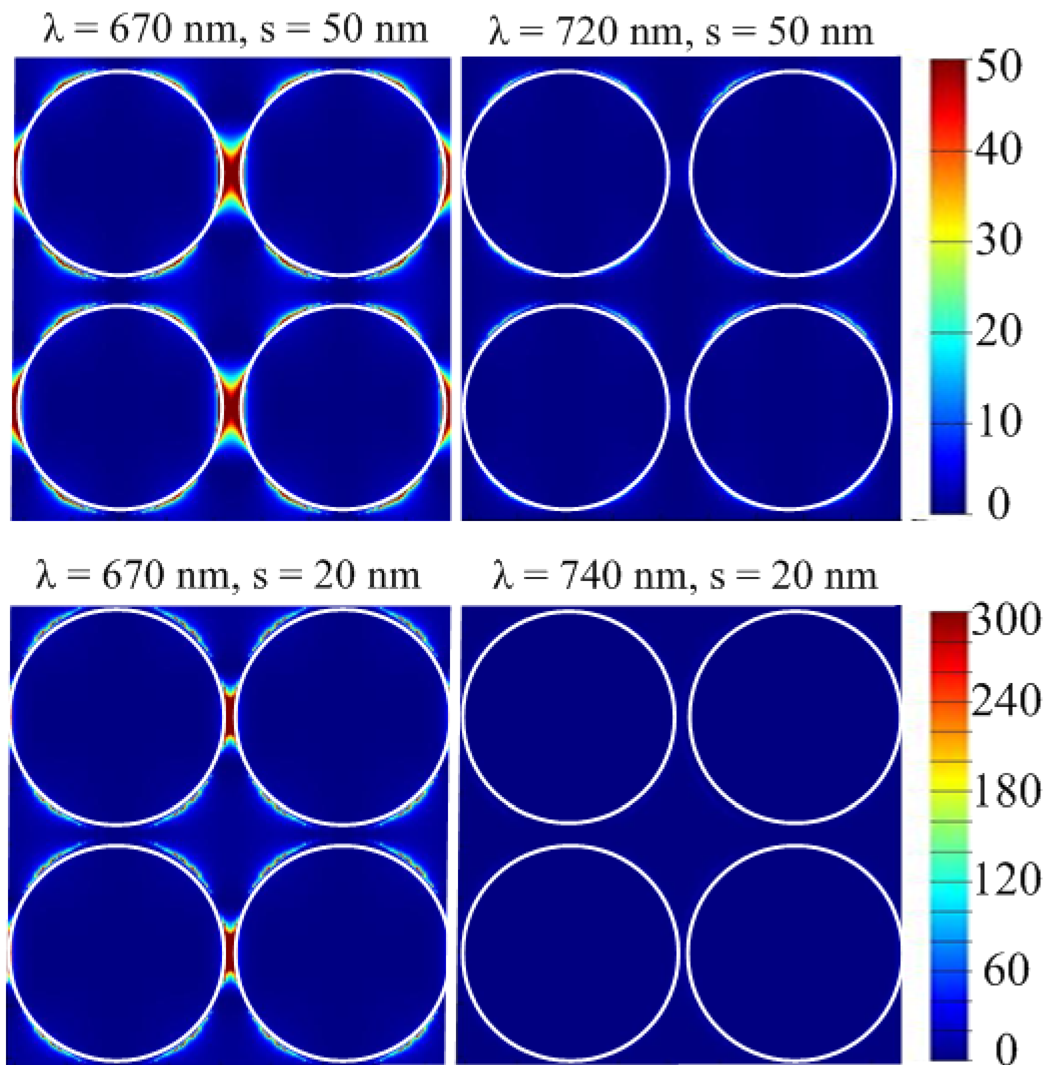

Fig. 6-7. Electric intensity distribution of nanorods with 50 nm (top panel) and 20 nm (bottom panel) spacings illuminated at 670 nm (λ_{max}) / 720 nm (λ_{min}) and 670 nm (λ_{max}) /740 nm (λ_{min}), respectively.

In addition, one can see that when the periodicity is 540 nm (inter-rod spacing = 40 nm), a broad resonance is located at ~630 nm. When the periodicity is reduced to 485 nm (inter-rod spacing = 35 nm), the resonance peak shifts to about 580 nm, exhibiting a yellow color.

Further, when the periodicity is smaller than 430 nm, sharper resonance peaks are distinct and more reflectance is observed due to stronger coupling in the small cavities, displaying as green, blue and cyan, respectively. Note that the resonance

becomes sharper and more intensity is reflected as the periodicity is decreased, implying a smaller damping and longer lifetimes due to smaller radiative rates. This is because the scattered fields of the opposing dipoles partially cancel out in the far-field (also known as the anti-bonding mode). It is also attributable to the decreased restoring force of the plasmon oscillations caused by strong interactions of opposite charges formed on tops of silver rods. Additionally, the FWHM undergoes a smooth decrease with reducing inter-rod periodicity from the red color to blue except for the cyan spectrum due to fabrication imperfections. Some of the neighboring rods are touching each other which is limited by the fabrication process. Once the conductive contact between rods is established, the original surface charge distribution is broken and a different regime is formed. The conductive coupling between nanorods leads to redistribution of surface charges resulting in the mergence of split individual modes. Fig. 6-6 (c) presents measured transmission spectra which show relatively low intensities. The transmission data were collected using the same setup shown in Fig. 6-1 but with the illumination light from the bottom (substrate side) instead of top (silver nanorods side). The calculated electric field distributions are presented in Fig. 6-7. Strong confinement of light on tops of the nanorods is obvious.

Basically, there are two critical issues for the color filter in this case. First, the resonance must be sharp enough (small FWHW) to distinguish individual colors. Otherwise, the presented colors will be either bright white or yellow. Broad resonance peaks are unable to give pure individual colors with a small spectral range using other methods (annular aperture array based color filter under transmission testing mode,

for instance). Second, multi-resonance peaks will degrade the performance of the fabricated devices. Thus, the intensity contrast of the resonance peaks must be high enough to differentiate the desired color from unintended disturbance.

6.3 Chapter summary

To conclude, tuning of plasmon resonance at visible frequencies using two dimensional plasmonic crystals has been demonstrated. Effective tuning of the LSPR is first achieved across the near infrared band using nanorods with large inter-rod spacings. Then the influence of inter-rod spacing on reflected resonances is investigated and the strong coupling effect with significantly decreased inter-rod spacings is studied. Based on these investigations, individual colors are finally filtered out and the color tuning can be achieved by controlling structural parameters of arrays. The oscillation of the electrons inside metal under the driving power of certain incident light energy results in precise control of the plasmon resonance.

Except for useful optical devices, plasmonic structures also give rise to novel physical phenomenon like the plasmon induced transparency. Pronounced resonance peaks can be generated in certain frequency bands using specially designd structures, as will be shown in Chapter 7.

Chapter-7: Plasmon-Induced Transparency in Plasmonic Crystals with Ultrasmall Gaps

In this chapter, 2-D plasmonic crystal designs consisting of different lattices which can exhibit an EIT-like optical response in the reflectance spectrum at visible frequencies will be proposed. Fabrication and optical characterization of single layer metamaterials with high quality will be shown. New reflectance peaks appear when the edge-to-edge separations of lattices are remarkably reduced. Strong coupling with decreasing separations is observed. These findings could find new applications in nanophotonics and plasmon-based sensing.

7.1 EIT in classic optics

Among all the plasmonic devices having unique and fascinating optical properties[105-112] which have been reported recently, regimes which can generate electromagnetically induced transparency (EIT) are of particular importance due to the fundamental physical interest. EIT was first observed in a quantum system[113] which refers to a transparency window in an absorptive medium due to the destructive quantum interference between two pathways. Nevertheless, it can be introduced into classic optics[114] because coherent effects in coupled resonators are similar to those in atomic systems. Importantly, the narrow transparent window in the absorption spectrum generated by EIT effects enables strong dispersion and great potential for applications in sensing and ultrafast switching. In addition, sharp resonances provide high quality factors and therefore give rise to high sensitivities, opening up new opportunities for sensing. Most recently, several different regimes[115-120] which can generate EIT have been demonstrated. However, most of these early approaches produce EIT by breaking structural symmetry since asymmetric geometries allow for strong coupling between bright and dark plasmon modes. Further tuning of resonance

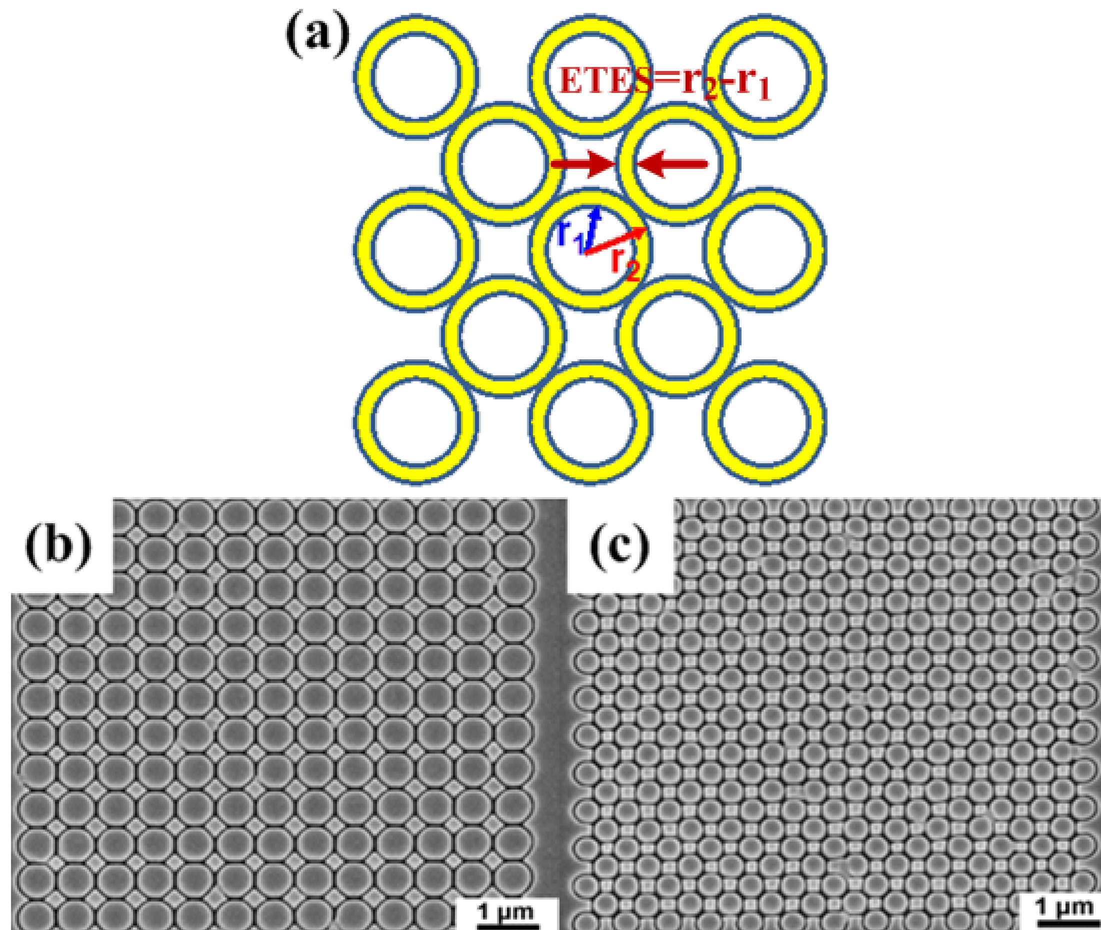

Fig. 7-1. (a) Schematic diagram of the FIB lithography method for nanorod fabrication based on nanoring patterning. (b) and (c), two typical designs proposed in this study. SEM images of (b) diamond-circle and (c) square-circle lattices.

and quality factor can be realized via changing the degree of asymmetry.[121] This chapter shows EIT-like spectra generation using 2-D symmetric plasmonic crystals with different lattices and ultrasmall inter-particle separations. Tuning of the resonance through geometric control is also demonstrated.

7.2 Plasmon-induced transparency in ultrasmall gaps

Fig. 7-1 (a) is the schematic view of a pattern for nanorod fabrication using FIB lithography. By realigning coaxial ring-like structures, one can easily remove the parts between coaxial structures.

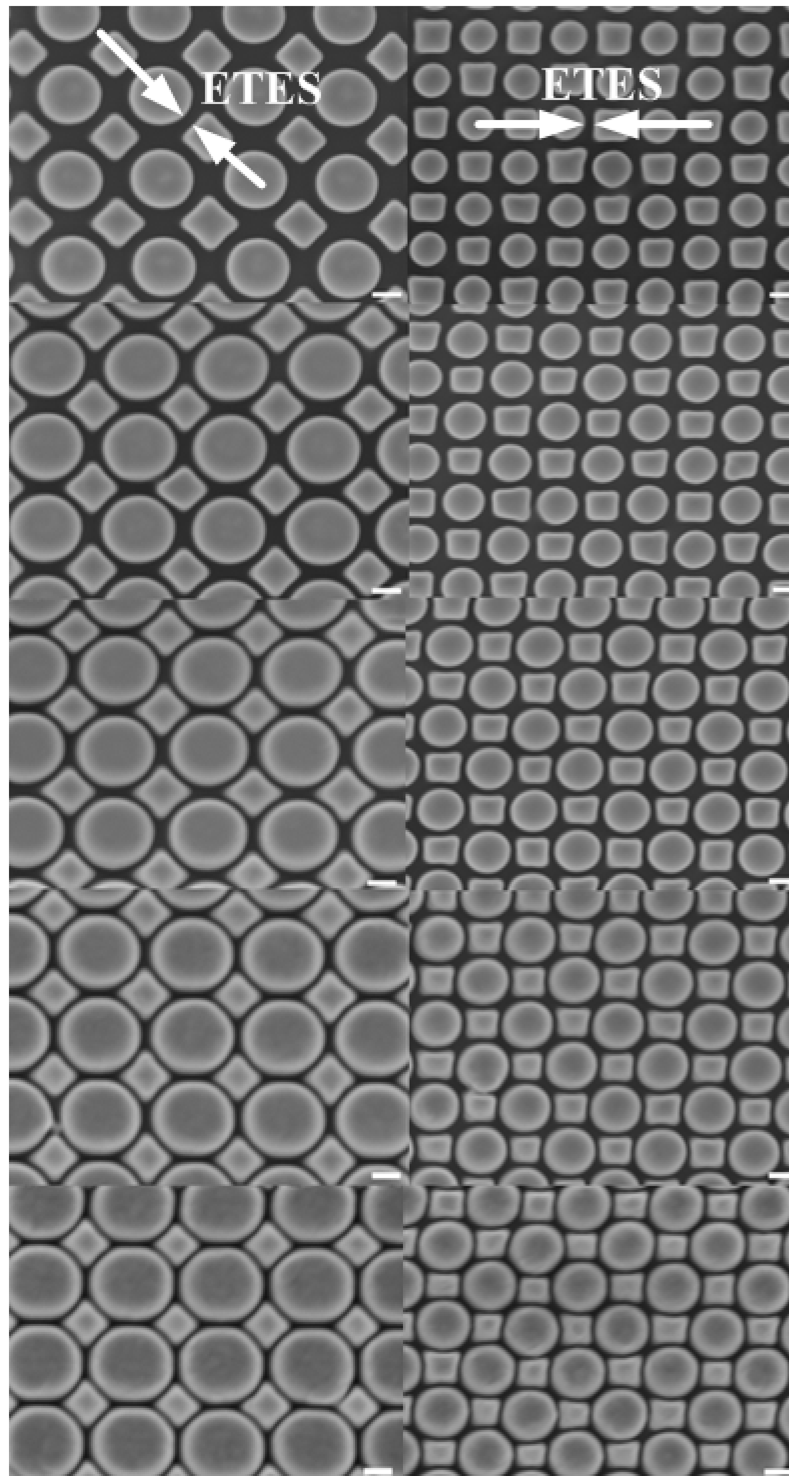

Fig. 7-2. SEM images showing decreasing ETES of diamond-circle (left column) and square-circle (right column) shaped lattices. All scale bars are 200 nm.

Using such an improved FIB patterning method, one can simply fabricate metallic nanorods with larger aspect ratios than when using EBL techniques, since there is no limitation of selectivity issue. Moreover, one can easily control the

geometry by varying inner and outer radii of individual rods and changing the distance between rods to precisely dominate overlapping areas. Therefore, the entire process is highly accurate and monolithic. Figs. 7-1 (b) and (c) demonstrate two typical structures (overview) under investigation in this work. Using FIB milling, diamond-circle and square-circle shaped lattices were fabricated. For both geometries, accurate control of lattice shape and spacing can be readily realized.

Fig. 7-2 demonstrates decreasing edge-to-edge separation (ETES = r_2 - r_1) of two lattice-shaped plasmonic arrays. It also presents the programmable character of FIB lithography. From Fig. 7-2, we can find lattices with different dimensions. By decreasing inner radii (with fixed outer radii) of the coaxial apertures, the ETES can be increased accordingly.

Interestingly, a distinct sharp peak is more expected to be observed in the reflectance spectrum instead of transmittance, therefore a new expression "electromagnetically induced reflectance" (EIR) was termed by Liu and coworkers recently.[116] As plotted in Fig. 7-3 (a), one can see that when the ETES is 90 nm and 70 nm, only broad resonances can be observed between 500 nm and 600 nm. When it is reduced to 50 nm, a new resonance peak appears at about 560 nm.

Further, when the ETES is smaller than 30 nm, new resonance peaks are distinct in the broad reflectance spectra at ～550 nm wavelength due to strong coupling in the small cavities. As the ETES is decreased, the resonance becomes sharper and more intensity is reflected, implying a smaller damping. Moreover, one can observe a redshift of resonance peaks located at ~700 nm with decreasing ETES.

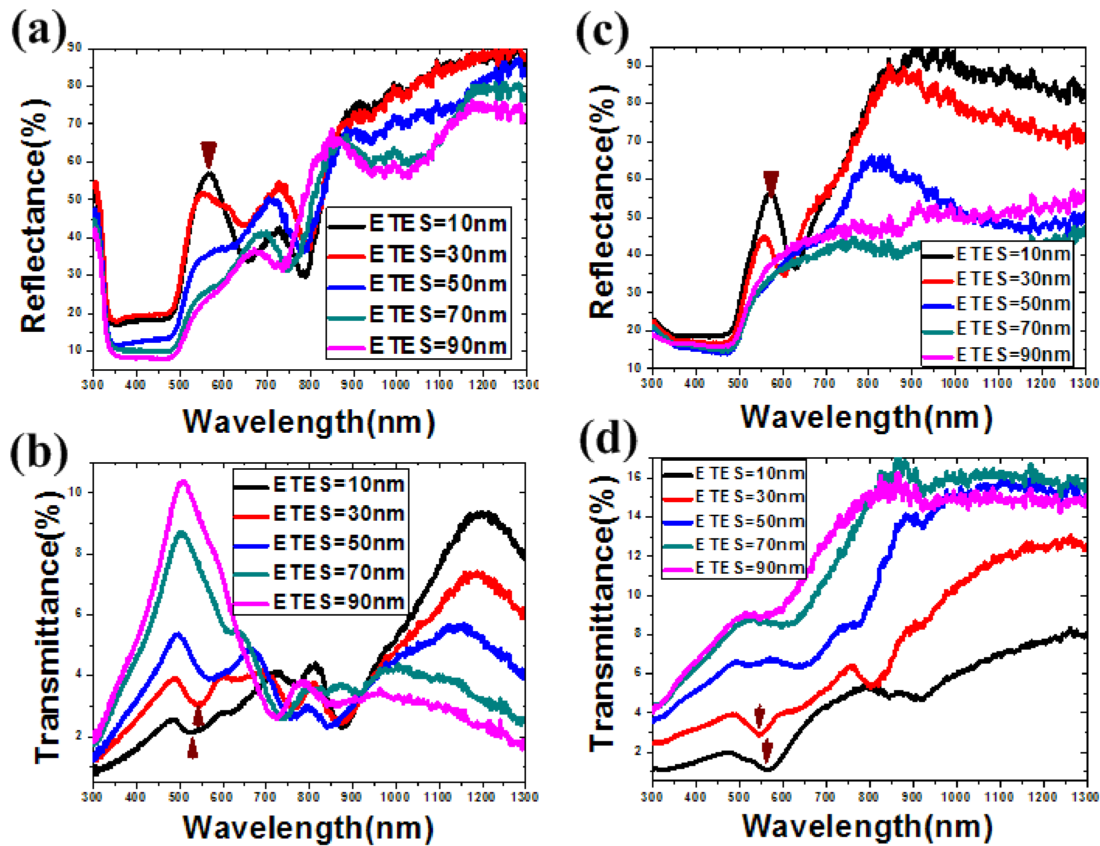

Fig. 7-3. Measured reflectance and transmittance spectra of plasmonic nanoantenna systems consisting of diamond-circle ((a) and (b)) and square-circle ((c) and (d)) shaped lattices with different ETES.

About 60 nm redshift is reached when the ETES is tuned from 90 nm (peak at 680 nm) to 10 nm (peak at 740 nm). Evidently, one can find an increment of intensity when the ETES is reduced. The sudden intensity drop of the 10 nm ETES spectrum is due to fabrication imperfections. For the long wavelength resonance located at about 900 nm, a similar increasing intensity and redshift of peak positions can be clearly seen with decreasing ETES. For square-circle lattices, the corresponding reflectance measurements are plotted in Fig. 7-3 (c). New resonance peaks emerge at about 550 nm and 560 nm when the ETES equals 30 nm and 10 nm, respectively.

Both enhanced intensity and redshift of peak positions are visible, which also applies to the long wavelength resonance after 800 nm. Reflected intensity of the peak

increases because the coupling in the cavities between neighboring lattices becomes stronger. Ultra-small spacings result in strong coupling in nanocavities which act as Fabry–Pérot resonators. Despite the fact that high transparency can be obtained in metamaterials (absorption is only affected by dielectric loss of metals), most of the plasmonic EIT analogues may show broad Fano-type resonances[122-124] due to the well-known difficulties of fabricating small and sharp line widths in metallic materials. Additionally, large scattering may be caused by rough surfaces and sidewalls as well as grain boundaries during fabrication.

7.3 Chapter summary

To conclude, 2-D plasmonic crystals with ultrasmall ETES exhibiting EIT effects have been demonstrated. Tuning of the optical response with varying lattices and different ETES has been investigated. High intensity and the EIR effect can be generated with small ETES due to strong coupling and interference between different modes. Significant enhancement and tunable local fields make such geometries greatly attractive for use in designing complex metamaterials with a desired response range and special purpose. Such geometries are crucial for fabricating plasmonic devices and can find extensive applications in focusing and imaging beyond the diffraction limit.

Chapter-8: Summary and Future Work

8.1 Summary of this thesis

An elegant way of fabricating suspended waveguides in LN is developed initially. Using combined techniques, monolithic fabrication of strip waveguides and PCs is available in bulk LN substrate now. The propagation loss is normally high due to light leakage caused by low refractive index contrast for waveguides in LN fabricated by PE process. A symmetric cladding structure (air-LN-air) can be formed once the buried sacrificial layer is removed by chemicals, resulting in significantly enhanced light confinement in the waveguide as well as dramatically reduced propagation loss. Subsequently, the influence of waveguide sidewall on device performance is investigated in detail in the following chapter. Ultra-high aspect ratio PCs are fabricated. The impact of tapered profiles is also thoroughly studied and ring-type FIB patterning function is proposed to replace conventional cylindrical holes milling for fabricating high aspect ratio structures with almost vertical sidewalls.

Novel structures realized in LN are introduced to noble metals, giving rise to fascinating plasmonic waveguides. Such devices have found important applications in developing nanophotonics and integrated optics. As typical examples, Chapters 5 and 6 demonstrate color filters under transmission and reflection testing modes using nanorings and rods, respectively. In particular, the nanorod color filter could be applied in digital light processing techniques since each mirror or pixel can be made very small to achieve a high resolution. In addition, different colors are generated by

pumping light signals, which can increase the response time greatly. More interestingly, a pronounced EIR-like resonance peak is observed in symmetric plasmonic patterns which can find important application in sensing, as demonstrated in Chapter 7.

8.2 Improving device performance

For waveguides fabricated by EBL, one critical issue is high optical loss generated by stitching error and rough waveguide sidewalls. Fig. 8-1 shows the stitching error which is common in standard EBL processes. Here, negative electron resist NEB 22 was used to fabricate a 4-μm wide strip waveguide on an x-cut LN substrate. Fig. 8-2 demonstrates rough sidewalls of a waveguide which result in high propagation loss during testing. Until now, buried channel waveguides in x-cut LN substrates have been fabricated using the PE method. Fig. 8-3 (a) shows the intensity distribution of such a waveguide captured by an infrared CCD camera. To characterize the performance of the channel waveguide, a laser with 1550 nm wavelength was coupled into the device using a lensed fiber with a tip diameter of 2.5 μm. The mode size is an important parameter particularly for nonlinear optics applications. The remote inhomogeneity shown in the intensity distribution is due to possible imperfect facets during dicing and polishing. Fig. 8-3 (b) shows the cross sectional view of a trench in LN after 30 min ICP etching with 80 nm chromium as etching mask. CHF_3/Ar (flow rate 50/50) was used as recipe at 20 mTorr chamber pressure. Argon was added to mix with CHF_3 in order to enhance the physical component during etching and thereby achieve a better profile.

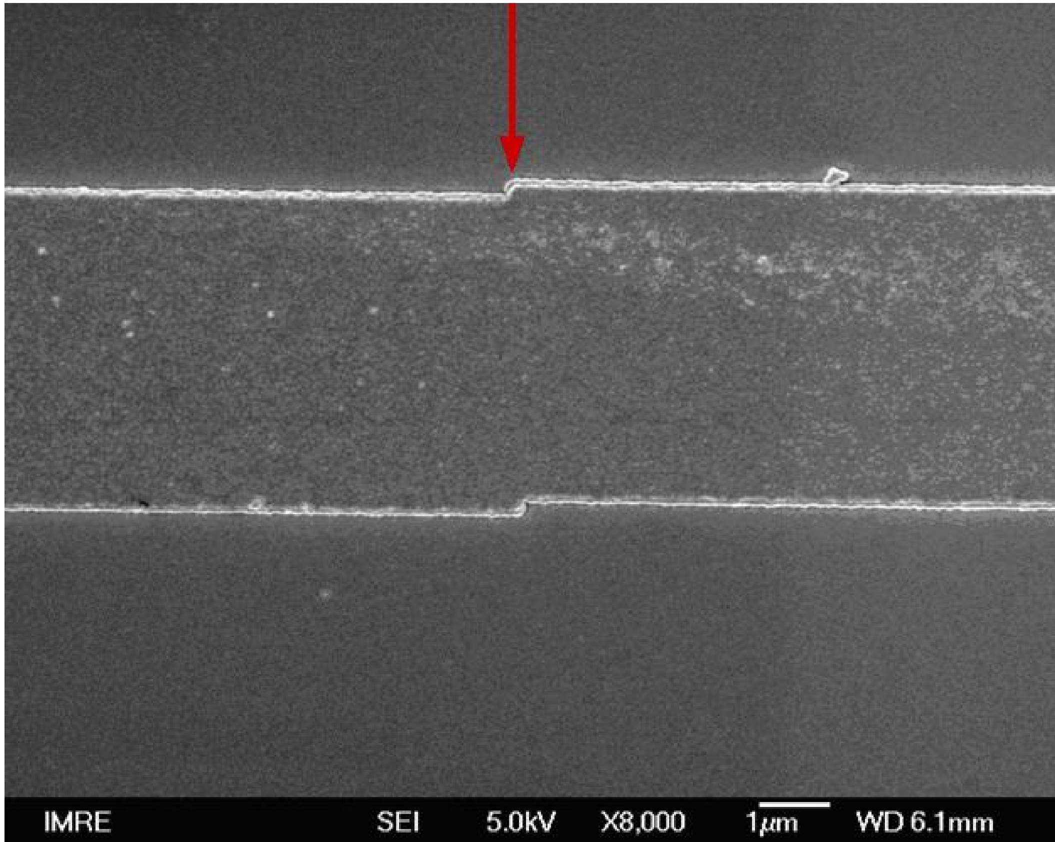

Fig. 8-1. SEM image showing the stitching error in a standard EBL process.

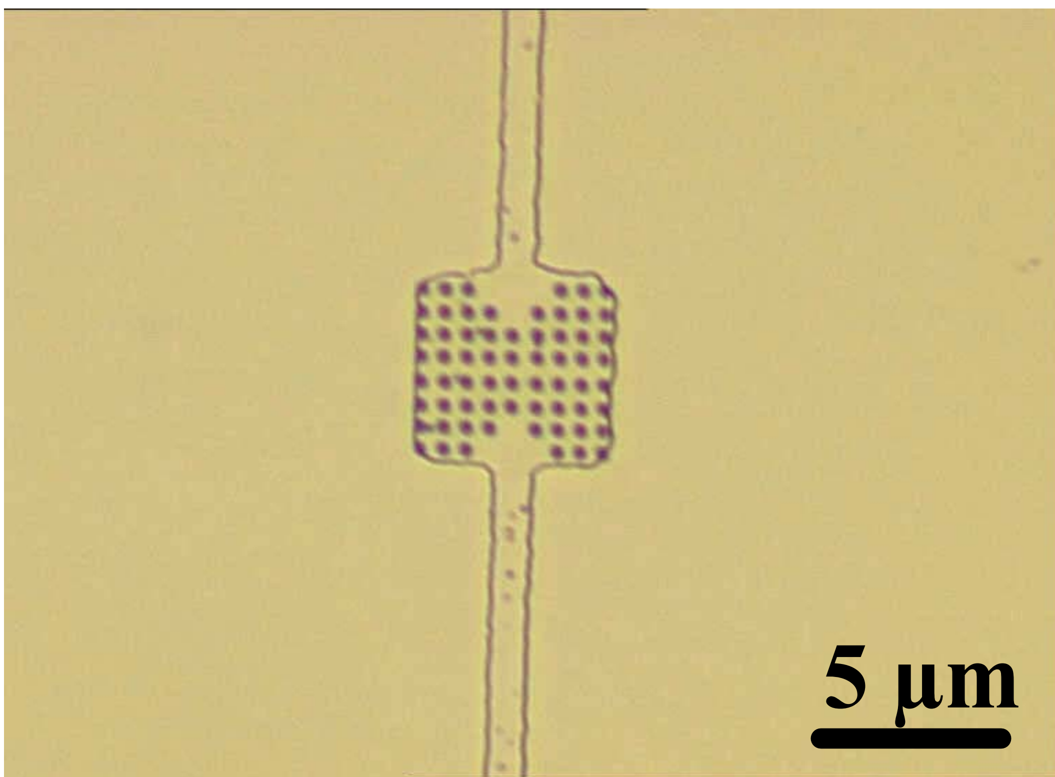

Fig. 8-2. Microscope image of a strip waveguide with rough sidewalls and PCs.

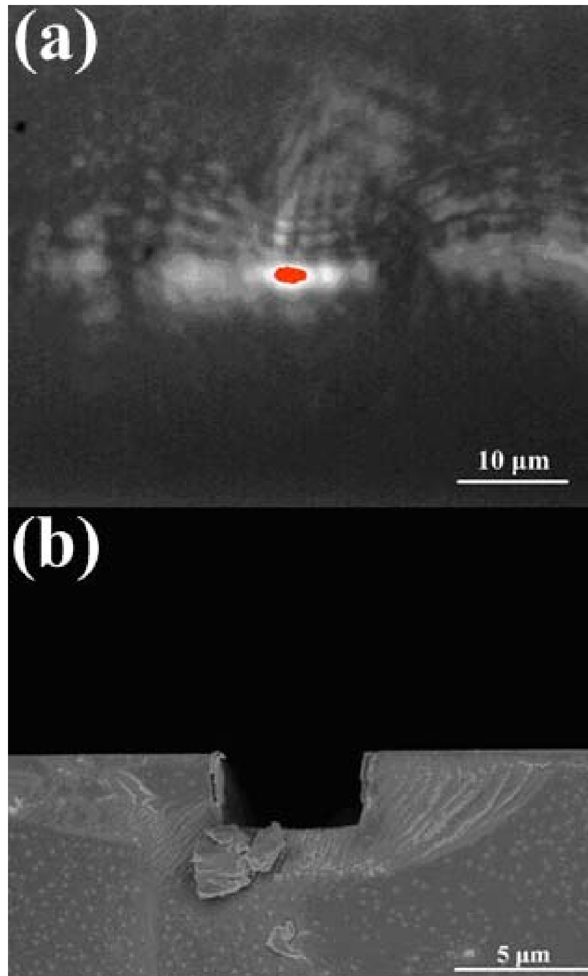

Fig. 8-3. (a) Intensity distribution of a channel waveguide fabricated in an x-cut LN substrate using proton exchange technique. (b) Cross section of a trench after ICP etching a channel waveguide.

After etching for 30 min, the samples were cooled down at 25 °C and taken out of the ICP chamber. Then the chromium layer was removed by wet etching. The measured etching rate is 92.5 nm/min (2.775-μm total etching depth for 30 min).

Fixed beam moving stage (FBMS) lithography is proposed to fabricate straight waveguides without stitching errors. During FBMS lithography, the waveguide is written in one continuous exposure path and the stage moves on a defined trajectory with a constant velocity while the electron beam does not change position. One can also simply apply ion bombardment to reshape waveguide sidewalls.

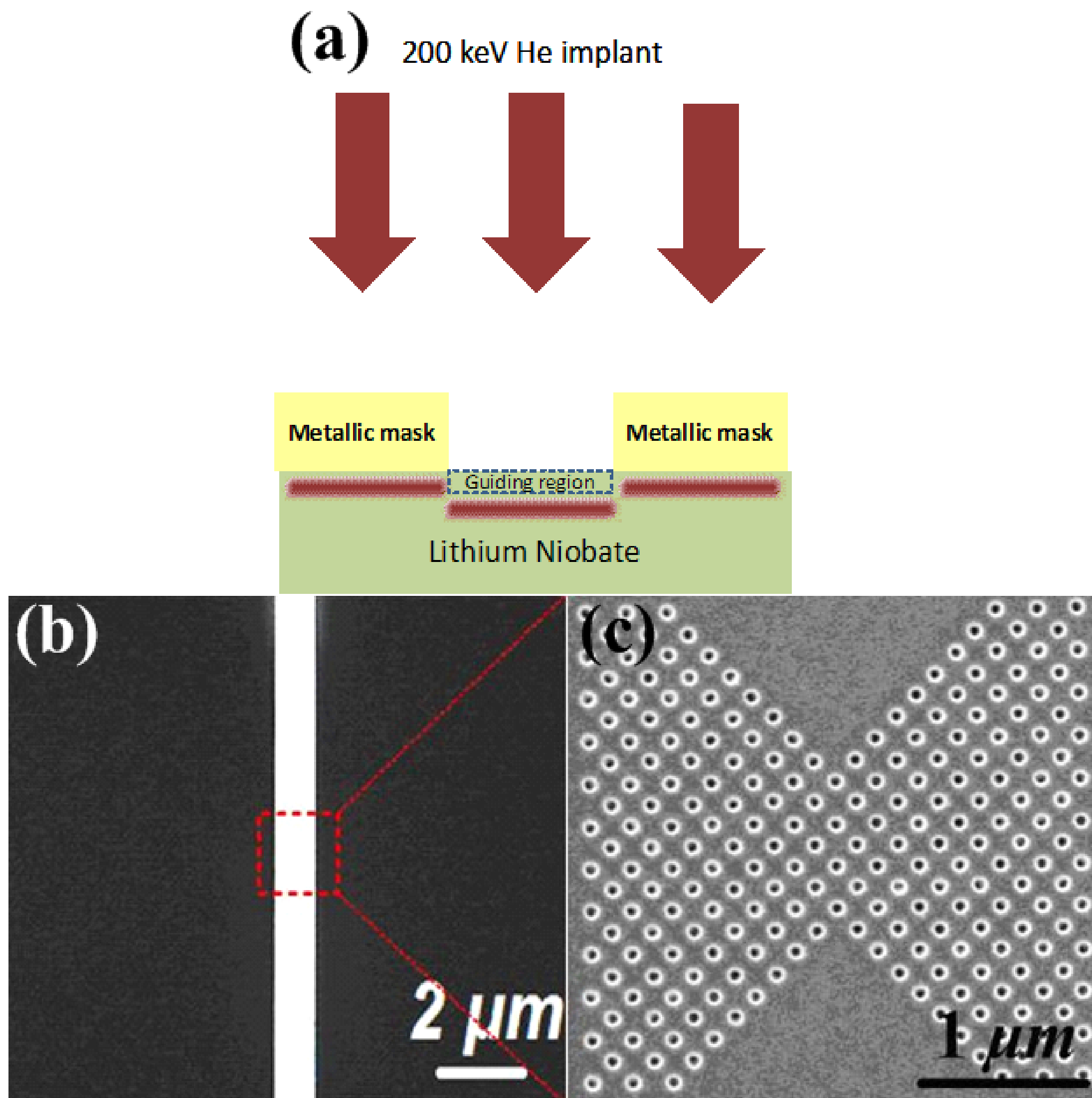

Fig. 8-4. (a) Schematic diagram of fabricating channel waveguides in LN using He implantation. (b) Microscope image of a strip waveguide on LN with a thick metal film as implantation mask. (c) Top view SEM showing PCs in the waveguide.

Another effective way to fabricate waveguides in LN is to use high energy implantation as illustrated in Fig. 8-4 (a). Fig. 8-4 (b) is the microscope image of a strip waveguide on LN with 550 nm gold as an implantation mask fabricated by photolithography followed by long duration ion milling. Fig. 8-4 (c) is a top view of FIB milled PCs in LN with tapered input and output. The characterization work is underway and the rest of this project has been handed over to a junior PhD student.

8.3 Tunable plasmonic devices using LCs

Another important future work is to fabricate tunable plasmonic devices by employing liquid crystals (LCs). Fig. 8-5 shows the schematic drawing of the experimental setup for characterization of a hybrid system. The probe light beam is focused onto the sample surface with a detecting area of $7 \times 7\ \mu m^2$ using a 36× objective lens combined with a variable aperture. The dynamic spectral change was achieved when the hybrid system was subject to a flood exposure using a UV light source (ELC-410).

By integrating a layer of photoresponsive LCs with the gold plasmonic nanostructures, a hybrid system can be formed. Meanwhile, an optically active functionality can be incorporated in this hybrid system. As known, a distinct advantage of azobenzene and azobenzene derivatives is that they can undergo a reversible photoisomerization between the *trans* (rodlike shape) and the *cis* (bent shape) molecular forms upon irradiation with UV or visible light.

Fig. 8-6 shows the measured absorption spectra of the *trans* and the *cis* forms of the BMAB molecules. The *trans*-isomer has a main absorption band in the UV around 350 nm (π–π* molecular transition), whereas the *cis*-isomer has an absorption peak in the visible around 450 nm (n–π* molecular transition). The *trans*-isomer, which is the thermally stable ground state, can transform into the *cis*-isomer by absorbing UV light. Under visible light irradiation or thermal isomerisation, the *cis*-isomer can return to the *trans*-isomer form[125], making the hybrid system highly reversible and reproducible.

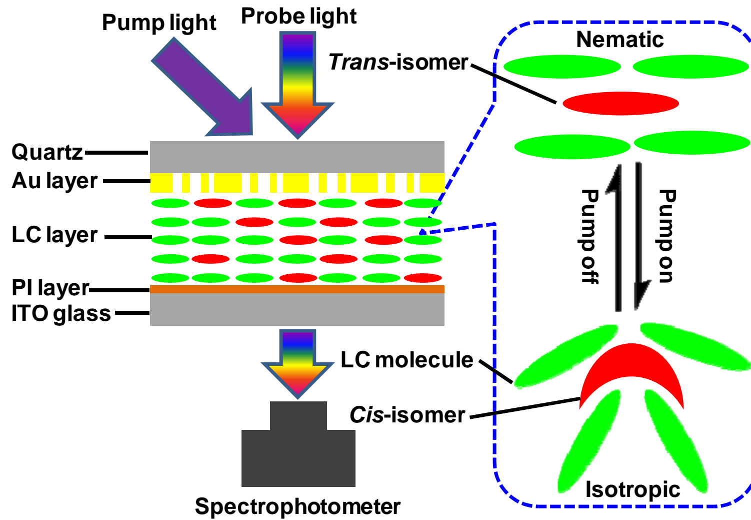

Fig. 8-5. Schematic of the experimental setup for characterization of the hybrid system. The enlarged part shows the reversible N–I phase transition induced by the *trans*-*cis* photoisomerization of the photochromic LCs.

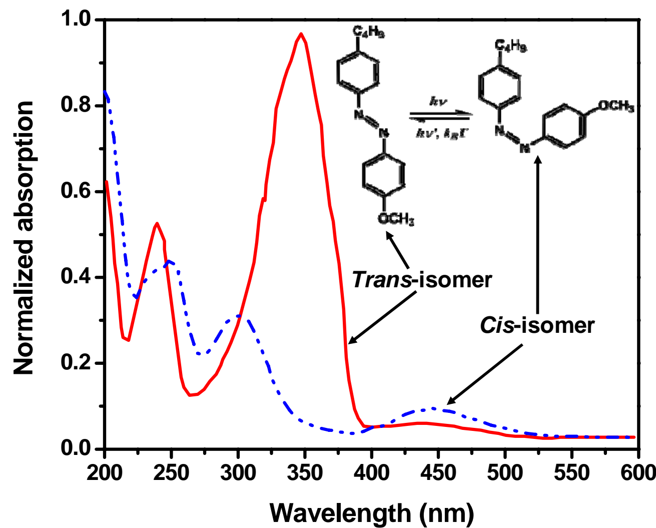

Fig. 8-6. The trans-cis isomerization of BMAB under UV flood exposure. Inset, the structure of a BMAB molecule and its reversible trans-cis isomerization.

By overlaying a photoresponsive LC layer on the gold plasmonic nanostructures, the optical transmission can be significantly enhanced due to index matching. The hybrid system demonstrates an all-optical modulation of the transmission intensity due to the *trans–cis* photoisomerization-induced N–I phase transition of the LCs. Such a hybrid system can be used for optically switchable color filters.

8.4 3-D metamaterials and novel plasmonic clusters

Last but not least, 3-D metamaterials are considered as an important future work because of their great potential in invisibility cloaking.[126-128] Fig. 8-7 demonstrates some typical examples fabricated by FIB etching.

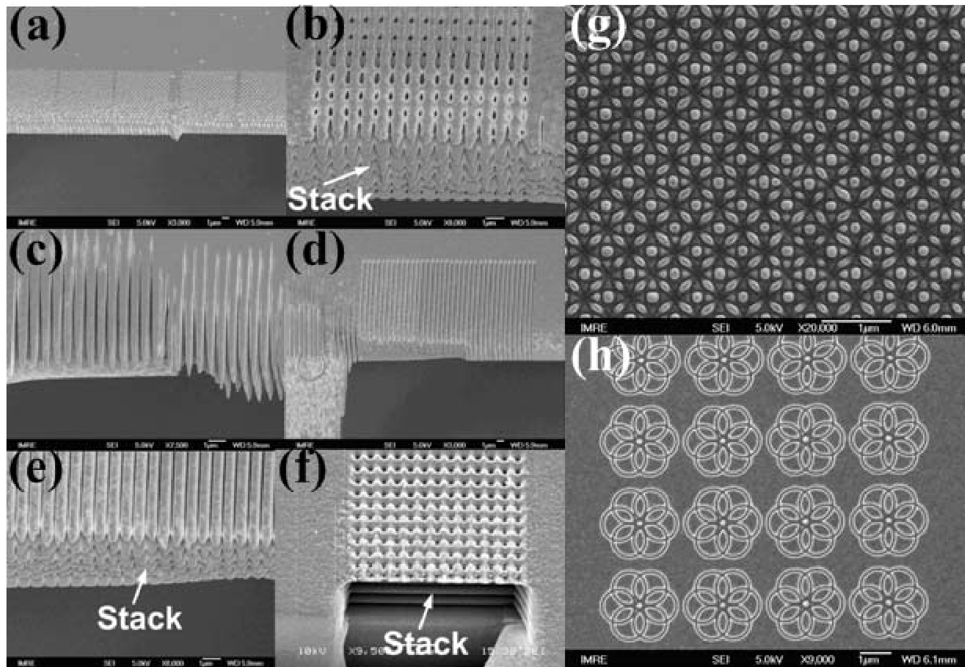

Fig. 8-7. (a) - (h) Examples of 3-D metamaterials and novel plasmonic clusters.

References:

1. T. Fujiwara, R. Srivastava, X. Cao and R. V. Ramaswamy, *Opt. Lett.* **18**, 346 (1993).
2. K. Ito and K. Kawamoto, *Jpn. J. Appl. Phys.* **31**, 3882 (1992).
3. V. M. N. Passaro, M. N. Armenise, D. Nesheva, I. T. Savatinova, and E. Y. B. Pun, *J. Lightwave Technol.* **20**, 71 (2002).
4. W. J. Liao, X. Chen, F. Chen, Y. Chen, Y. Xia, and Y. Chen, *Opt. Laser Technol.* **36**, 603 (2004).
5. M. -P. Bernal, N. Courjal, J. Amet, M. Roussey, and C. H. Hou, *Opt. Commun.* **265**, 180 (2006).
6. M. Roussey, M. -P. Bernal, N. Courjal, and F. I. Baida, *Appl. Phys. Lett.* **87**, 241101(2005).
7. M. Roussey, M. -P. Bernal, N. Courjal, D. Van Labeke, F. I. Baida, and R. Salut, *Appl. Phys. Lett.* **89**, 241110(2006).
8. T. -J. Wang, C. -F. Huang, W.-S Wang, and P. -K Wei, *J. Lightwave Technol.* **22**, 1764 (2004).
9. H. Hu, R. Ricken, W. Sohler, and R. B. Wehrspohn, *IEEE Photonics Technol. Lett.* **19**, 417 (2007).
10. H. Hu, A. P. Milenin, R. B. Wehrspohn, H. Hermann and W. Sohler, *J. Vac. Sci. Technol. A* **24**, 1012 (2006).
11. Z. Ren, P. J. Heard, J. M. Marshall, P. A. Thomas, and S. Yu, *J. Appl. Phys.* **103**, 034109 (2008).
12. T. -L. Ting, L. -Y. Chen, and W. -S Wang, *IEEE Photon. Technol. Lett.* **18**, 568 (2006).
13. Y. A. Vlasov, M. O'Boyle, H. F. Hamann, and S. J. McNab, *Nature* **438**, 65 (2005).
14. S. J. McNab, N. Moll, and Y. A. Vlasov, *Opt. Express* **11**, 2927 (2003).
15. E. Dulkeith, S. J. McNab, and Y. A. Vlasov, *Phys. Rev. B* **72**, 115102 (2005).

16. Y. -B. Park, B. Min, K. J. Vahala, and H. A. Atwater, *Adv. Mater.* **18**, 1533 (2006).

17. M. Levy, R. M. Osgood, Jr., R. Liu, L. E. Cross, G. S. Cargill, III, A. Kumar, and H. Bakhru, *Appl. Phys. Lett.* **73**, 2293 (1998).

18. D. Djukic, R. M. Roth, R. M. Osgood, Jr., K. Evans-Lutterodt, H. Bakhru, S. Bakhru, and D. Welch, *Appl. Phys. Lett.* **91**, 112908 (2007).

19. P. Rabiei and P. Gunter, *Appl. Phys. Lett.* **85**, 4603 (2004).

20. P. Rabiei and W. H. Steier, *Appl. Phys. Lett.* **86**, 161115 (2005).

21. F. Schrempel, T. Gischkat, H. Hartung, T. Höche, E. -B. Kley, A. Tünnermann, and W. Wesch, *Opt. Lett.* **34**, 1426 (2009).

22. F. Sulser, G. Poberaj, M. Koechlin, and P. Günter, *Opt. Express* **17**, 20291 (2009).

23. Y. Tanaka, T. Asano, Y. Akahane, B. -S. Song, and S. Noda, *Appl. Phys. Lett.* **82**, 1661 (2003).

24. G. W. Burr, S. Diziain, and M. -P. Bernal, *Opt. Express* **16**, 6302 (2008).

25. M. Roussey, F. I. Baida, and M. -P. Bernal, *J. Opt. Soc. Am. B* **24**, 1416 (2007).

26. F. Chen, *J. Appl. Phys.* **106**, 081101 (2009).

27. F. Lacour, N. Courjal, M. -P. Bernal, A. Sabac, C. Bainier, and M. Spajer, *Opt. Mater.* **27**, 1421 (2005).

28. A. Guarino, G. Poberaj, D. Rezzonico, R. Degl'Innocenti, and P. Günter, *Nat. Photon.* **1**, 407 (2007).

29. G. Si, E. J. Teo, A. A. Bettiol, J. Teng, and A. J. Danner, *J. Vac. Sci. Technol. B* **28**, 316 (2010).

30. Nan Yao, Ed., *Focused Ion Beam Systems: Basics and Applications* (Cambridge University Press, 2007).

31. C. R. Musil, J. Melngailis, S. Etchin, and T. E. Haynes, *J. Appl. Phys.* **80**, 3727 (1996).

32. C. Crell, S. Friedrich, H.-U. Schreiber, and A. D. Wieck, *J. Appl. Phys.* **82**, 4616 (1997).

33. M. J. Vasile, Z. Niu, R. Nassar, W. Zhang, and S. Liu, *J. Vac. Sci. Technol. B* **15** (6), 2350 (1997).

34. S. Matsui, T. Kaito, J. Fujita, M. Komuro, K. Kanda, and Y. Haruyama, *J. Vac. Sci. Technol. B* **18** (6), 3181 (2000).

35. R. DeVore, J. F. Toth, and R. Caldecott, *J. Appl. Phys.* **44**, 4488 (1973).

36. R. DeVore, *J. Appl. Phys.* **45**, 2874 (1974).

37. M. Ibanescu, Y. Fink, S. Fan, E. L. Thomas, and J. D. Joannopoulos, *Science* **289**, 415 (2000).

38. H. Kurt and D. S. Citrin, *Opt. Express* **13**, 10316 (2005).

39. A. Cicek and B. Ulug, *Opt. Express* **17**, 18381 (2009).

40. H. Kurt, R. Hao, Y. Chen, J. Feng, J. Blair, D. P. Gaillot, C. Summers, D. S. Citrin, and Z. Zhou, *Opt. Lett.* **33**, 1614 (2008).

41. P. Shi, K. Huang, X. Kang, and Y. Li, *Opt. Express* **18**, 5221 (2010).

42. A. Säynätjoki, M. Mulot, J. Ahopelto and H. Lipsanen, *Opt. Express* **15**, 8323 (2007).

43. J. Feng, Y. Chen, J. Blair, H. Kurt, R. Hao, D. S. Citrin, C. J. Summers, and Z. Zhou, *J. Vac. Sci. Technol. B* **27** (2), 568 (2009).

44. T. W. Ebbesen, H. J. Lezec, H. F. Ghaemi, T. Thio, and P. A. Wolff, *Nature* **391**, 667 (1998).

45. S. P. Burgos, R. de Waele, A. Polman and H. A. Atwater, *Nat. Mater.* **9**, 407 (2010).

46. R. de Waele, S. P. Burgos, H. A. Atwater, and A. Polman, *Opt. Express* **18**, 12770 (2010).

47. Y. Poujet, J. Salvi and F. I. Baida, *Opt. Lett.* **32**, 2942 (2007).

48. F. I. Baida, A. Belkhir, D. Van Labeke, and O. Lamrous, *Phys. Rev. B* **74**, 205419

(2006).

49. F. J. Rodríguez-Fortuño, C. García-Meca, R. Ortuño, J. Martí, A. Martínez, *Opt. Lett.* **34**, 3325 (2009).
50. F. I. Baida and D. Van Labeke, *Phys. Rev. B* **67**, 155314 (2003).
51. M. I. Haftel, C. Schlockermann, and G. Blumberg, *Phys. Rev. B* **74**, 235405 (2006).
52. M. I. Haftel, C. Schlockermann, and G. Blumberg, *Appl. Phys. Lett.* **88**, 193104 (2006).
53. S. M. Orbons, A. Roberts, D. N. Jamieson, M. I. Haftel, C. Schlockermann, D. Freeman, and B. Luther-Davies, *Appl. Phys. Lett.* **90**, 251107 (2007).
54. R. de Waele, S. P. Burgos, A. Polman and H. A. Atwater, *Nano Lett.* **9**, 2832 (2009).
55. A. Ono, J. Kato, and S. Kawata, *Phys. Rev. Lett.* **95**, 267407 (2005).
56. S. Kawata, A. Ono, and P. Verma, *Nat. Photon.* **2**, 438 (2008).
57. Y. Liu, G. Bartal, and X. Zhang, *Opt. Express* **16**, 15439 (2008).
58. F. I. Baida and D. Van Labeke, *Opt. Commun.* **209**, 17 (2002).
59. F. I. Baida, Y. Poujet, B. Guizal, and D. Van Labeke, *Opt. Commun.* **256**, 190 (2005).
60. F. I. Baida, Y. Poujet, J. Salvi, D. Van Labeke, and B. Guizal, *Opt. Commun.* **282**, 1463 (2009).
61. J. Salvi, M. Roussey, F. I. Baida, M. -P. Bernal, A. Mussot, T. Sylvestre, H. Maillotte, D. Van Labeke, A. Perentes, I. Utke, C. Sandu, P. Hoffmann, and B. Dwir, *Opt. Lett.* **30**, 1611 (2005).
62. B. Heshmat, D. Li, T. E. Darcie, and R. Gordon, *Opt. Express* **19**, 5912 (2011).
63. S. M. Orbons, M. I. Haftel, C. Schlockermann, D. Freeman, M. Milicevic, T. J. Davis, B. Luther-Davies, D. N. Jamieson, and A. Roberts, *Opt. Lett.* **33**, 821 (2008).
64. P. Banzer, J. Kindler, S. Quabis, U. Peschel, and G. Leuchs, *Opt. Express* **18**, 10896 (2010).
65. E. H. Barakat, M. -P. Bernal, and F. I. Baida, *Opt. Express* **18**, 6530 (2010).

66. F. J Rodríguez-Fortuño, C. García-Meca, R. Ortuño, J. Martí, and A. Martínez, *Opt. Lett.* **34**, 3325 (2009).

67. A. Belkhir and F. I. Baida, *Phys. Rev. E* **77**, 056701 (2008).

68. D. Van Labeke, D. *Gérard*, B. Guizal, F. I. Baida, and L. Li, *Opt. Express* **14**, 11945 (2006).

69. http://www.lumerical.com/

70. P. B. Johnson and R. W. Christy, *Phys. Rev. B* **6**, 4370 (1972).

71. H. Raether, *Surface plasmons on Smooth and Rough Sufaces and on Gratings*; Springer: New York, (1988).

72. S. A. Maier, *Plasmonics: Fundamentals and Applications*; Springer: New York, (2007).

73. W. L. Barnes, A. Dereux, and T. W. Ebbesen, *Nature* **424**, 824 (2003).

74. M. L. Brongersma and P. G. Kik, Eds., *Surface Plasmon Nanophotonics*; Springer: Dordrecht, (2007).

75. J. A. Fan, C. Wu, K. Bao, J. Bao, R. Bardhan, N. J. Halas, V. N. Manoharan, P. Nordlander, G. Shvets, and F. Capasso, *Science* **328**, 1135 (2010).

76. J. B. Lassiter, J. Aizpurua, L. I. Hernandez, D. W. Brandl, I. Romero, S. Lal, J. H. Hafner, P. Nordlander, and N. J. Halas, *Nano Lett.* **8**, 1212 (2008).

77. H. Kuwata, H. Tamaru, K. Esumi, and K. Miyano, *Appl. Phys. Lett.* **83**, 4625, (2003).

78. J. N. Anker, W. P. Hall, O. Lyandres, N. C. Shah, J. Zhao, and R. P. Van Duyne, *Nat. Mater.* **7**, 442 (2008).

79. I. Zorić, E. M. Larsson, B. Kasemo, and C. Langhammer, *Adv. Mater.* **22**, 4628 (2010).

80. C. Langhammer, M. Schwind, B. Kasemo, and I. Zorić, *Nano Lett.* **8**, 1461 (2006).

81. J. Aizpurua, P. Hanarp, D. S. Sutherland, M. Käll, G. W. Bryant, and F. J. García de Abajo, *Phys. Rev. Lett.* **90**, 057401 (2003).

82. P. Nordlander, *ACS Nano* **3**, 488 (2009).

83. S. I. Bozhevolnyi, V. S. Volkov, E. Devaux, J. Y. Laluet, and T. W. Ebbesen,

Nature **440**, 508 (2006).

84. J. C. Weeber, G. Colas-des-Francs, A. Bouhelier, and A. Dereux, *Phys. Rev. B* **83**, 115433 (2011).
85. J. A. Dionne, H. J. Lezec, and H. A. Atwater, *Nano Lett.* **6**, 1928 (2006).
86. S. Lal, S. Link, and N. J. Halas, *Nat. Photon.* **1**, 641 (2007).
87. Z. Liu, Q. Wei, and X. Zhang, *Nano Lett.* **5**, 957 (2005).
88. Z. Liu, Y. Wang, J. Yao, H. Lee, W. Srituravanich, and X. Zhang, *Nano Lett.* **9**, 462 (2009).
89. X. Wei, X. Luo, X. Dong, and C. Du, *Opt. Express* **15**, 14177 (2007).
90. W. Srituravanich, N. Fang, C. Sun, Q. Luo, and X. Zhang, *Nano Lett.* **4**, 1085 (2004).
91. C. Sun, K. Su, J. Valentine, Y. T. Rosa-Bauza, J. A. Ellman, O. Elboudwarej,B. Mukherjee, C. S. Craik, M. A. Shuman, F. F. Chen, and X. Zhang, *ACS Nano* **4**, 978 (2010).
92. J. McPhillips, A. Murphy, M. P. Jonsson, W. R. Hendren, R. Atkinson, F. Höök, A. V. Zayats, and R. J. Pollard, *ACS Nano* **4**, 2210 (2010).
93. P. Offermans, M. C. Schaafsma, S. R. J. Rodriguez, Y. Zhang, M. Crego-Calama, S. H. Brongersma, and J. G. Rivas, *ACS Nano* **5**, 5151 (2011).
94. F. Hao, P. Nordlander, Y. Sonnefraud, P. Van Dorpe, and S. A. Maier, *ACS Nano* **3**, 643 (2009).
95. O. Vazquez-Mena, T. Sannomiya, L. G. Villanueva, J. Voros, and J. Brugger, *ACS Nano* **5**, 844 (2011).
96. B. Auguié, and W. L. Barnes, *Phys. Rev. Lett*. **101**, 143902 (2008).
97. Y. Chu, E. Schonbrun, T. Yang, and K. B. Crozier, *Appl. Phys. Lett.* **93**, 181108 (2008).
98. A. V. Kabashin, P. Evans, S. Pastkovsky, W. Hendren, G. A. Wurtz, R. Atkinson, R. Pollard, V. A. Podolskiy, and A. V. Zayats, *Nat. Mater.* **8**, 867 (2009).
99. V. G. Kravets, F. Schedin, and A. N. Grigorenko, *Phys. Rev. Lett*. **101**, 087403 (2008).
100. R. M. Bakker, A. Boltasseva, Z. Liu, R. H. Pedersen, S. Gresillon, A. V.

Kildishev, V. P. Drachev,and V. M. Shalaev, *Opt. Express* **15**, 13682 (2007).

101. S. Enoch, R. Quidant, and G. Badenes, *Opt. Express* **12**, 3422 (2004).
102. E. Lamothe, G. Leveque, and O. J. F. Martin, *Opt. Express* **15**, 9631 (2007).
103. C. P. Burrows, and W. L. Barnes, *Opt. Express* **18**, 3187 (2010).
104. O. Lecarme, T. Pinedo-Rivera, K. Berton, J. Berthier, and D. Peyrade, *Appl. Phys. Lett.* **98**, 083122 (2011).
105. J. B. Pendry, *Phys. Rev. Lett*. **85**, 3966 (2000).
106. J. B. Pendry, D. Schurig, and D. R. Smith, *Science* **312**, 1780 (2006).
107. W. Cai, U. K. Chettiar, A. V. Kildishev, and V. M. Shalaev, *Nat. Photon.* **1**, 224 (2007).
108. Ni. Fang, H. Lee, C. Sun, and X. Zhang, *Science* **308**, 534 (2005).
109. Z. Liu, S. Durant, H. Lee, Y. Pikus, N. Fang, Y. Xiong, C. Sun, and X. Zhang, *Nano Lett.* **7**, 403 (2007).
110. L. Yin, V. K. Vlasko-Vlasov, J. Pearson, J. M. Hiller, J. Hua, U. Welp, D. E. Brown, and C. W. Kimball, *Nano Lett.* **5**, 1399 (2005).
111. S. I. Bozhevolnyi, J. Erland, K. Leosson, P. M. W. Skovgaard, and J. M. Hvam, *Phys. Rev. Lett*. **86**, 3008 (2001).
112. G. A. Wurtz, R. Pollard, W. Hendren, G. P. Wiederrecht, D. J. Gosztola, V. A. Podolskiy, and A. V. Zayats, *Nat. Nanotechnol.* **6**, 107 (2011).
113. S. E. Harris, J. E. Field, and A. I*mamoğlu, Phys. Rev. Lett*. **64**, 1107 (1990).
114. S. Zhang, D. A. Genov, Y. Wang, M. Liu, and X. Zhang, *Phys. Rev. Lett*. **101**, 047401 (2008).
115. N. Liu, L. Langguth, T. Weiss, J. Kästel, M. Fleischhauer, T. Pfau, and H. Giessen, *Nat. Mater.* **8**, 758 (2009).
116. N. Liu, T. Weiss, M. Mesch, L. Langguth, U. Eigenthaler, M. Hirscher, C. Sönnichsen, and H. Giessen, *Nano Lett.* **10**, 1103 (2010).
117. V. A. Fedotov, M. Rose, S. L. Prosvirnin, N. Papasimakis, and N. I. Zheludev, *Phys. Rev. Lett*. **99**, 147401 (2007).
118. N. Papasimakis, V. A. Fedotov, N. I. Zheludev, and S. L. Prosvirnin, *Phys. Rev. Lett*. **101**, 253903 (2008).

119. P. Tassin, L. Zhang, Th. Koschny, E. N. Economou, and C. M. Soukoulis, *Phys. Rev. Lett*. **102**, 053901 (2009).

120. A. Christ, O. J. F. Martin, Y. Ekinci, N. A. Gippius, and S. G. Tikhodeev, *Nano Lett.* **8**, 2171 (2008).

121. K. Aydin, I. M. Pryce, and H. A. Atwater, *Opt. Express* **18**, 13407 (2010).

122. N. Verellen, Y. Sonnefraud, H. Sobhani, F. Hao, V. V. Moshchalkov, P. Van Dorpe, P. Norlander, and S. A. Maier, *Nano Lett.* **9**, 1663 (2009).

123. A. Christ, Y. Ekinci, H. H. Solak, N. A. Gippius, S. G. Tikhodeev, and O. J. F. Martin, *Phys. Rev. B* **76**, 201405 (2009).

124. Y. Sonnefraud, N. Verellen, H. Sobhani, G. Vandenbosch, V. V. Moshchalkov, P. Van Dorpe, P. Norlander, and S. A. Maier, *ACS Nano* **4**, 1664 (2010).

125. K. G. Yager and C. J. Barrett, *J. Photochem. Photobiol. A* **182**, 250 (2006).

126. D. Chanda, K. Shigeta, S. gupta, T. Cain, A. Carlson, A. Mihi, A. J. Baca, G. R. Bogart, P. Braun, and J. A. Rogers, *Nat. Nanotechnol.* **6**, 402 (2011).

127. H. F. Ma and T. J. Cui, *Nat. Commun.* **1**, 21 (2010).

128. C. M. Soukoulis and M. Wegener, *Nat. Photon.* **5**, 523 (2011).